DEVELOPMENT OF LASER MICRO-FABRICATED SURFACES TO ACCELERATE & ENHANCE ENDOTHELIAL CELL ADHESION AND PROLIFERATION

CHING TZU GOH

A thesis submitted in partial fulfilment of the requirements of Liverpool John Moores University for the degree of Doctor of Philosophy

This research programme was carried out in collaboration with Biomer Technology Ltd

July 2014

ABSTRACT

The aim of this thesis was to develop novel indirect laser micro-textured polymer substrates to accelerate and enhance bovine aorta endothelium (BAE-1) cell adhesion and proliferation. The response of BAE-1 and human coronary smooth muscle cells (HCASMCs) were studied, including cell adhesion, proliferation, β-actin expression, migration velocity, and migration directionality. The laser used in these experiments was a SPI infrared solid state fibre laser. By using beam overlapping scanning strategies surfaces having two types of distinct surface features were produced: (i) microfringes and (ii) microripples. Through a series of laser parameter optimisation experiments control of the melt expulsion mechanism and the formation of an intact recast ring could be generated. Overlapping of the focused beam resulted in an overlapping of the recast rings, thus resulting in surfaces having microripple and microfringe features.

Experimental results found that polyurethane 1A, which has a projecting topography of ~4μm width microfringes, significantly increased BAE-1 cell adhesion, proliferation, and β-actin expression, compared to the non-textured surface. However, strong adhesion to this surface decreased mean cell migration velocity. Furthermore, focal adhesions were confined to the microfringe structure leading to the formation of parallel actin stress fibres and as a result changed the cell migration directionality. On the other hand, Polyurethane 3D, which has a projecting topography of ~6μm width microripples, was also found to significantly enhance BAE-1 cell proliferation (only at 72 hours post cell seeding), β-actin expression and migration velocity, when compared to the non-textured polyurethane.

Differences were also found between BAE-1 and HCASMCs cells. HCASMCs were less sensitive to the polymer substrates and were not found to be influenced by the microfringe and microripple structures. However, the microridges with >700nm height on polyurethane 1A, 3A and 3D were found to promote HCASMC alignment parallel to the microridges. In addition, the Z1A1 polyurethane used for pattern transfer through polymer casting has shown delayed HCASMCs adhesion. Further investigation is required to study the effect of Z1A1 polyurethane's chemical properties on HCASMACs behaviour. Overall, the data obtained from this work, suggests that the width dimension of the microfringes and microripples between ~4-6μm are important regulators for BAE-1 behaviour and microridge heights >700nm are important regulators for HCASMCs alignment. The preliminary data provided from this work can be used for stent technology development in the future.

Table of Contents

ACKNOWLEDGEMENTS

My childhood dream was to become an electronic engineer under the influence of my father. However, life set me a new path when I enrolled on a Masters degree at the Liverpool John Moores University (LJMU). After completing my Masters degree at LJMU, I was offered a place to study for a PhD in Tissue Engineering at General Engineering Research Institute, LJMU which was a joint decision by Dr Paul French, Dr Mark Murphy, Dr Martin Sharp, Professor David R. Burton and Dr Francis Lilley. No one can whistle a symphony, my 3-years PhD work is truly a cohort of combined effort and practical experience from many kind people who I am indebted to.

I am grateful to Paul French, a man who led me into the fantasy world of laser engineering. You taught me everything you knew about laser machining without reservation, you brought me along to conferences which widen my research horizons.

To me, Mark Murphy, you are not only a mentor but also a friend and family to me. You were always there for me when I confronted problems in biological experiments. Your great personality and humour were no doubt a precious addition towards my PhD life. Thank you for your shared appreciation of beers, life experiences, and friendship.

There is one man who I must not forget to thank, Simon Dixon, director of Biomer. Thank you for your support and supply of chemical substrate which was the key element in making the polymer moulding.

My tissue engineering work wouldn't have been able to finish if not because of the excellent technical service provided by Peter Moran. I am sorry if I have been a trouble maker to you as I kept bombarding you with various peculiar sketching of biological devices and solid work designs. But you proved that you could make anything out from your hands.

There weren't many PhD students in GERI working on tissue engineering. Aos, you were an exceptional nice lab mate to work with in a laser lab. I cherished our moments of sharing and contemplating life's challenges over tea breaks.

A lab will lose its functional operation if there is no adequate supply of consumables. To this, I thank the prettiest woman in GERI - Helen Pottle for being a responsible person who was in charge of calling suppliers, getting quotations, and ordering goods. This has always been a strong force in driving my lab work's progression.

Pa and ma, thank you for the love and support that you have given throughout the years. Your regular warm greetings sent from 6400 miles away from UK via Skype have always warmed my heart and cured my homesick. I can't thank you enough. To my family-in-laws, I thank you for your interest in my work and progression throughout the years.

In Chinese saying, every successful man has a dedicated woman behind him. Wan Yee, my lovely wife, without you, I am nothing. Your help in making sure I would get this thesis finished, checking my typo error between lines, and giving me confidence that I could finish my work make you undeniable the greatest support of all.

LIST OF ABBREVIATIONS

2D	Two dimensional
3D	Three dimensional
ADSC	Adipose tissue-derived stem cells
AFM	Atomic force microscopy
AlF_3	Aluminium fluoride
ArF	Argon fluoride
BAE-1	Bovine aorta endothelium-1
BAECs	Bovine aorta endothelium cells
BARC	Bottom antireflective coatings
BHK	Baby hamster kidney
CABG	Coronary artery bypass graft
CAD	Computer-aided design
CHD	Coronary heart disease
CLSM	Confocal laser scanning microscope
CW	Continuous wave
DAPI	4',6-Diamidino-2-Phenylindole, Dihydrochloride
DC	Direct current
DES	Drug eluting stents
DLIP	Direct laser interference patterning
DNA	Deoxyribonucleic acid
DUV	Deep ultraviolet
dyne/cm^2	dyne per square centimeter
EBL	Electron beam lithography
EC	Endothelial cells

ECM	Extracellular matrices
EDP	Ethylenediamine pyrocatechol
ELISA	The enzyme-linked immunosorbent assay
F_2	Fluorine
fs	Femtoseconds
FA	Focal adhesions
FAK	Focal adhesion kinase
FAP	Focal adhesion points
FC	Fibroblast cells
FDA	Food and Drugs Administration
FIB	Focused ion beam
FITC	Fluorescein isothiocyanate
FMI	Forward Migration Index
Fsec	Femtoseconds
g	Gram
GPa	Gigapascal
GS	Luminal microgroove
HASMCs	Human aortic smooth muscle cells
HAEC	Human Aortic Endothelial Cells
HCASMCs	Human coronary smooth muscle cells
Hg	Mercury-vapor lamp
HRP	Horse Radish Peroxidase
HSFL	High spatial frequency laser-induced periodic surface structures
HSQ	Hydrogen silsesquioxane
IgG	Immunoglobulin G
J/cm^{-2}	Joules per square centimeter
KOH	Potassium hydroxide

KrF	Krypton fluoride
kV	Kilo voltages
kW	Kilowatt
LIPSS	Laser induced periodic surface structure
LSFL	Low spatial frequency laser-induced periodic surface structures
m/s	Meter per second
MDCK	Madin Darby canine kidney
MEMS	Microelectromechanical systems
MHC	Major histocompatibility complex
MLVS	Multi-Link Vision stent
MPa	Megapascal
NA	Numerical aperture
NHSBT	National Health Service blood and transplant
Nm	Nanomolar
NOR-1	Neuron derived orphan receptor-1
PC12	Pheochromocytoma
PCI	percutaneous coronary intervention
PCL	Polycaprolactone
PDGF	Platelet derived growth factor
PDLA	Polylactic acid
PDMS	Polydimethylsiloxane
PEO	Poly(ethylene oxide)
PET	Poly(ethylene terephthalate)
PGA	Polyglycolic acid
PI	Polyimide
PLGA	Poly (lactide-co-glycolide)
PMMA	Polymethylmetacrylate

PS	polystyrene
RAECs	Rat aortic endothelial cell
RBM	Rat bone marrow osteoblast-like
RF	Radio frequency
RIE	Reactive ion etching
RMS	Root mean square
SCs	Schwann cells
SD	Standard deviation
SEM	scanning electron microscopy
SEW	surface electromagnetic wave
SMC	Smooth muscle cell
SPP	surface plasmon polaritons
SSG	split skin grafting
StEM	Standard error mean
TEM	Transmission electron microscopy
Ti-6Al-4V	Grade 5 titanium alloy (titanium with chemical composition of 6% aluminium, 4% vanadium)
TMAH	Tetramethylammonium hydroxide
TMB	3, 3’, 5, 5’-Tetramethylbenzidine liquid substrate
TPP	Two photon polymerization
Tris	Tris(hydroxymethyl)aminomethane
µCP	Micro-contact printing
UV	Ultraviolet
UV-vis	Ultraviolet–visible
ʌ	Periodical structure
X-ray	X-radiation
α	Alpha

β	Beta
μC	Microcoulombs
λ	Wavelength

LIST OF FIGURES

LIST OF TABLES

Chapter 1

1.0 Introduction

In animal tissues, the extracellular matrix (ECM) consists of surface topographies ranging from the nano to the micron scale and acts to provide a scaffold for cell support and development. Cells interact with native ECM through integrins and transduce the physical cues taken from the ECM into intracellular signals so as to produce a coordinated cellular response such as cell adhesion, maintenance of correct morphology, cell migration, proliferation, and gene expression (Huttenlocher and Horwitz, 2011).

The recognition the importance of the cell-surface interaction started when Ross Granville Harrison observed that embryonic frog spinal neurons were extended along on the meshwork of spider web filaments (Harrison, 1911). The phenomenon was later described as contact guidance by Paul Weiss (Weiss, 1945). Later, micro and nano fabrication technology was adopted from the semiconductor industry that was used to manufacture microelectromechanical systems (MEMS). However, MEMS manufacturing equipment requires a high capital cost, but research and development has led to advances in lower cost technology which has been developed in other fields and includes such techniques as soft lithography, polymer electrospinning, indirect and direct laser patterning techniques etc. The rapidly development of advanced micro and nano fabrication technology has revolutionised tissue engineering and the regenerative medicine field.

With the advances in micro and nano fabrication technologies, a number of diverse surface topographies have been designed and produced to study and manipulate cell response. A number of investigations have demonstrated that substrates that consist of features with dimensions in the range of micrometres and nanometres could either suppress or enhance cell performance, influencing the cells response to the surface. As well as the scale of the structure, feature design also plays a

crucial role for cell-surface interactions. The most extensive feature that has been studied is the micro and nanogroove topography, this structure has been shown to have potentially beneficial effects on a wide range of medical implants in a number of biomedical applications, such as stent implantations (Dibra *et al.*, 2005) (Sprague *et al.*, 2012), dental implants (Fillies *et al.*, 2005), bone (Lenhert *et al.*, 2005) and nerve regeneration (Hsu *et al.*, 2005) etc.

In this thesis, the focus is on surface topographies relevant to stent applications and the aim is to generate novel micro scale topographies that could potentially physically accelerate vascular endothelial cell behaviours without using pharmaceutical drugs. Currently, the drug eluting stent (DES) has been widely used for treating coronary heart disease (CHD) and has proved to be superior to bare metal stents (BMS) due to a lower restenosis rate after stent placement. Although, the pharmaceutical anti-proliferative drug carried by a DES can inhibit smooth muscle cell (SMCs) proliferation, the major concern with DES is that it also suppressing re-endotheliazation leading to late (1month - 1year) and very late stent thrombosis (ST) (>1 year) after DES implantation. Many researches have demonstrated that nano and micro-topography could improve a wide range of biomedical application. Hence, BMS consisting of physical topography could be an alternative treatment for CHD.

The objective of this thesis are as follows:

(a) To use a cost effective (<10,000 pounds), user friendly and portable solid state SPI laser system to develop polyurethane substrates having novel micro-topography

(b) To understand how micro-textured and non-textured polyurethane affects BAE-1 cell adhesion, level of spread (as measured by cell height) and BAE-1 cell proliferation.

(c) To understand how micro-textured and non-textured polyurethane affects focal adhesion formation and actin organisation in BAE-1 cells. Such knowledge will complement the adhesion and proliferation studies.

(d) To understand how micro-textured and non-textured polyurethane affects β-actin expression levels in BAE-1 cells and to link this to parameters of cell migration, e.g. velocity.

(e) To understand how micro-textured and non-textured polyurethane affects focal adhesion formation and actin organisation in BAE-1 cells under flow conditions.

1.1 Structure of the Thesis

This thesis is concerned with modifying surface topography to enhance the adhesion and growth of cells, namely endothelial cells which play an important role in maintaining vascular haemostasis. Such work has potential to improve medical implant technology and tissue engineering processes, in this case stent technology.

Chapter two in this thesis will be used to 'set the scene', so as to highlight the potential impact that surface topography could have on controlling cell growth, particularly of endothelial cells in clinical, coronary stent applications.

In a broader context the chapter will begin by introducing the history, development and disadvantages of tissue and organ transplantation, followed by the emergence of tissue engineering, and how tissue engineering may be used to improve and replace tissue and organ transplant. Next, the chapter will discuss implant prosthetic device failure and the importance of surface topography on cell bio-functionality. Furthermore, it will discuss the naturally occurring extracellular matrix topography, which is inspiring scientists to either reproduce or generate new user designed surface topography to maintain or improve cell bio-functionality.

In chapters three and four, the thesis discusses the current technologies available used to fabricate surfaces having micro and nano-sized topographical features. This will be followed by a discussion of how cells respond to such surface

topography and the impact surface topography can have on coronary stent applications.

In chapters five and six, the thesis will discuss the details of laser micro-texturing of surfaces, the model cells types used during this research and the experiments that were carried out.

In Chapter seven, the results of the engineered surfaces are presented through optimization of the of the microfabrication process. Surface characterization is also described.

In chapter eight, the results of the biological experiments are presented. These results are based on experiments that were carried out in order to investigate the effects of surface topography on cell behaviours including cell adhesion, height, proliferation, migration and β-actin expression.

Chapter nine is a discussion of the results. This chapter will draw upon the relevant literature to discuss the results and put them into context with the aim of understanding how the cells interact and move of the textured surfaces.

Chapter ten contains the conclusions drawn from this research work.

Chapter eleven will provide some suggestions for future work.

Chapter 2

2.1 The History of Organ and Tissue Transplantation

This chapter will begin with the history of tissue and organ transplantation, drugs development and their disadvantages and how tissue engineering may be used to improve and replace tissue and organ transplants. The emergence of tissue engineering is important to aid humans to be able to regenerate lost body parts or organs. Some small animals such as lizards, frogs and salamanders possess the ability to regenerate lost limbs or organs. Understanding this unique ability would open opportunities of undreamt in human health (Straube and Tanaka, 2006). The degeneration of organs through processes such as ageing or disease and trauma has been investigated by scientists over the last century. For people who develop such health problems the only clinical solution is organ and tissue transplantation. Here healthy organs such as kidneys, liver, lungs, heart, pancreas, bowel, cornea, bone, skin, heart valves, tendons and cartilage are obtained from a suitable donor for transplantation into the patient (Kemp, 2006).

The first human to human kidney transplantation was performed by Dr. Yu Yu Voronoy in Russia in 1933, but unfortunately the transplanted kidneys were found to be thrombotic and thus failed to function. This failure was due to an immune response caused by a mismatch of class I and II of major histocompatibility complex (MHC) and which induces T-lymphocyte interaction, ultimately resulting in organ rejection (García *et al.*, 2012). It was not until 1954 that the first successful kidney transplant was carried out by an American plastic surgeon Dr. Joseph Murray. He was transplanting a kidney from a genetically identical twin brother to his twin, who was suffering from chronic renal failure. The operation was successful with no observed rejection of the organ (Klintmalm, 2004). Hence, they realized that the immunological response is a formidable obstacle in organ transplantation. In 1959 and 1960, a British surgeon Dr. Roy Calne studied a new compound called azathioprine, which is an imidazole derivative of 6-

mercaptopurine supplied by Burroughs and the Wellcome Trust. This drug is a purine analogue, which can be incorporated into replicating deoxyribonucleic acid (DNA) and also blocks purine synthesis in the lymphocyte salvage pathway (Maltzman and Koretzky, 2003). Dr. Calne showed in dogs that azathioparine could help prevent organ rejection. Later, this drug was registered under the name of Imuran. However, further work on humans found that very few patients could tolerate the required doses of Imuran that would be needed to prevent organ rejection.

The discovery of a new immunosuppressive drug 'cyclosporine' by Sandoz in 1971 revolutionised immunopharmacology. This drug is isolated from fungal species *Tolypocladium inflatum Gams*, which is a calcineurin (protein phosphatase 2B involved in activating T cells) inhibitor that mainly suppresses T cells activation by inhibiting the transcription of cytokine genes including IL-2 and IL-4 (Matsuda and Koyasu, 2000).

The discovery of cyclosporine has showed an increase in the survival rate for kidney transplantation of up to 70% and a decrease in mortality rate to approximately 10%. Moreover, the use of cyclosporine has also increased the survival rate for liver and heart transplantation, which is now up to 80% (Watson and Dark, 2011). Despite the rapid evolution of immunosuppressive drugs such as cyclosporine, tacrolimus and mycophenolic acid, further development of immune-repressive drug treatment for transplantation has been advanced by combination therapy, particularly the combination of sirolimus and everolimus, which has been found to further reduce the risk of transplantation rejection However, the number of organs available from donors are limited compared to demand and many patients die before an organ donor becomes available. In the UK alone, the National Health Service Blood and Transplant (NHSBT) special health authority reported that since April to September 2014 only 1,459 patients have received transplants and there are still 6,925 patients waiting for an organ transplant.

Tissue transplantation such as skin transplant are now routinely performed. For example, a procedure known as split skin grafting (SSG) is typically used for patients with skin disease and skin trauma. The autografting method is most commonly used for SSG. The procedure involves removing a thin slice of

epidermis or dermis from the patient while leaving sufficient reticular dermis in the wound bed (from where the skin is removed) to regenerate itself. The skin graft is then meshed up by passing through the meshing device to increase surface area and transferring it to larger secondary wound. Although the skin can be obtained from the patient's own body, the patient donor site may suffer severe pain due to exposure of nerve endings and scarring after recovery. Therefore, the best donor site areas must be invisible to the public and are therefore typically obtained from the thigh, buttock, back, upper arm, forearm and abdominal wall. In more serious cases, for example where a patient has suffered from severe burn (i.e. higher than 60%), autologous grafting cannot be used, therefore allogeneic transplantation becomes the only clinical solution. This however, carries the associated risk of graft rejection (Beldon, 2007).

Hence, tissue engineering has emerged in attempt to overcome by developing an alternative clinical strategies to fulfil the high demand of the organ and tissue replacement each year. To date most of the tissue engineered constructs have been successfully produced, but are largely limited to non-modular organs such as cartilage, corneal epithelium, and skin epidermis. The main barrier to success for tissue engineering is the complexity of the architecture and most of the tissues and organs are composed of multiple cell types such as epithelial, fibroblast, and smooth muscles cells (Zorlutuna *et al.*, 2012). To mimic and replicate the complexity and functions of the tissues and organs, tissue engineering must rely on more than one type of technology, such as high throughput scaffold printing, automated cell sorters, cell and organ bioreactors to turn research into reality for clinical applications (Lott *et al.*, 2013).

2.2 The Emergence of Tissue Engineering

With the drawbacks associated with organ and tissue transplantation, the field of tissue engineering emerged in the mid-1980s with the aim of addressing significant medical needs in tissue replacement and regeneration therapies, by providing complementary solutions to the former discussed therapies (Vacanti, 2006). Tissue engineering has shown great potential in the development of medical implant and transplantation technology. The main clinical success to date are tissue engineered bladders, small arteries, skin grafts, cartilage, and a full trachea which have been successfully implanted in patients (Atala *et al.*, 2006)(Wystrychowski *et al.*, 2011) (Matsumura *et al.*, 2003) (Fulco *et al.*, 2014)(Gonfiotti *et al.*, 2014). However, some organs such as the bladder and trachea are costly to build, requiring customization for each individual patient and involving complex approaches (Lott *et al.*, 2013).

Tissue engineering is a multidisciplinary field which combines the principles of biological, materials and engineering sciences in order to develop functional substitutes which can be used to replace, restore and enhance cell function on damaged tissue or organs. The distinctive feature of tissue engineering is to offer "off the shelf" tissues and organ substitutes generated from a patient's own cells and tissues and which can improve biocompatibility, biofunctionality and immunogenic rejection (Burg *et al.*, 2010).

Tissue engineering utilises techniques which include: (i) injection of functional stem cells into damaged or non-functional tissues, to stimulate tissue regeneration. For example, a Belgian medical doctor used stem cells to treat penile erectile dysfunction caused by nerve damage. The authors showed that injection of adipose tissue-derived stem cells (ADSC) into a rat penis could improve the recovery of erectile dysfunction (Albersen *et al.*, 2010) and (ii) the use of biocompatible scaffolding to construct new tissues or organs

However, the first technique mention above cannot be used for large tissue regeneration. It can only be used to stimulate tissues regeneration, because most of the cell types in the human body are "anchorage" dependent and will not survive if an appropriate adhesive site is absent. In addition, large tissue reconstruction requires appropriate scaffolding for proper tissue formation such as scaffold with

specific surface topography design (for example porous scaffold), stiffness, and chemical properties (Yamato and Okano, 2004).

The second technique has been widely used for tissues regeneration because the three dimensional scaffolds are capable of supporting large tissues and can easily be transferred to the damaged site with high precision. This process comprises the isolation of cells from the patient via biopsy and expanding them on a three dimensional, bio-engineered scaffold in a bioreactor under controlled physiological conditions, so that they develop into functional tissues. The functional tissue-biomaterial complex is then implanted onto the defective site (Tan *et al.*, 2006). The development of tissue engineering technologies has been used to cure heart disease, renal failure and spinal cord injury and has the potential to treat other diseases that could result in tissue damage and malfunctions, this will be discussed further in the next section.

2.3 Tissue Engineering Development

Over the past 20 years, scientists have worked diligently to develop organ substitutes and functional tissues for clinical applications. For example, constructed synthetic heart valves have been used to replace the heart valves in sheep (Shinoka *et al.*, 1995). In this particular work the researchers used synthetic biodegradable scaffolds that were composed of a polyglactin woven mesh surrounded by non-woven polyglycolic acid (PGA). This construct was seeded with fibroblast cells to form a tissue-like sheet that was further seeded with endothelial cells. After cultivation, the researchers replaced the right posterior leaflet of the pulmonary valve with the tissue-engineered heart valve and studied the response. The results showed no sign of stenosis and trivial pulmonary regurgitation

Similarly, a study carried out at the University of Basel investigated using tissue-engineered articular cartilage to repair large osteochondral defects in adult rabbits. The authors constructed the tissue-engineered articular cartilage by using biodegradable PGA scaffolds. These scaffolds were then seeded with primary

chondrocytes, harvested from the femora and tibiae of the rabbit. The scaffold was composed of 13µm diameter fibres which formed a nonwoven mesh with a void volume of 97%. After 4 to 6 weeks of *in vitro* cultivation, the engineered cartilage was implanted into the defective rabbit knee. The results demonstrated that after 6 months the engineered cartilage had remodelled into osteochondral tissue with characteristic architectural features able to withstand physiological loading with Young's moduli of 0.8MPa (Schaefer *et al.*, 2002). Some engineered organs have been fully developed, however some are still under development including a bioengineered urinary bladder (Oberpenning *et al.*, 1999)(Drewa *et al.*, 2012), kidney (Song *et al.*, 2013)(Friedrich MJ, 2004), trachea (Gonfiotti *et al.*, 2014), and gastrointestinal tract (Bitar and Raghavan, 2012).

Although great progress has been made in tissue and organ regeneration there are still many hurdles that need to be overcome and many aspects that have to be taken into consideration. For example, tissues having different functional roles such as protective tissues, mechano-sensitive tissues, electro-active tissues and shear stress-sensitive tissues have specifically constructed extracellular matrices (ECM) that help organise cellular architecture and provide mechanical support (Figure 2.1). Therefore it is important that when tissue-constructs are developed for transplantation, the morphology of the scaffolding is suitable for promoting cell attachment and growth.

For instance, tendons transmit 'movement force' from skeletal muscle to the bone, while also helping in holding bones together at the joint. To facilitate these roles tendons are composed of parallel collagen fibers with a highly ordered multi-hierarchical organization. In order for tendons to transmit forces to bone, the collagen molecules must be arranged into parallel fibrils and then assembled into fibril bundles with a diameter of 50-500nm. These fibrils are embedded in proteoglycan-rich matrix forming a fascicles (diameter of 50–300µm). Eventually, the fascicles form into tendon fibres with diameters within the region of 100–500µm and having an elastic moduli of 10 MPa–2GPa (Franchi *et al.*, 2007). Another example, is that of ventricular cavities which are surrounded by elongated cardiac myocytes which are arranged into layered anisotropic bands. This organisation has evolved to generate contraction for cardiac pumping (Agarwal *et*

al., 2013). Additionally, nerve cells' alignment is also very important during nerve regeneration. Therefore biocompatibility, scaffold surface architecture and bio-functionality all need to be carefully considered when designing and implanting materials intended to help tissue regeneration.

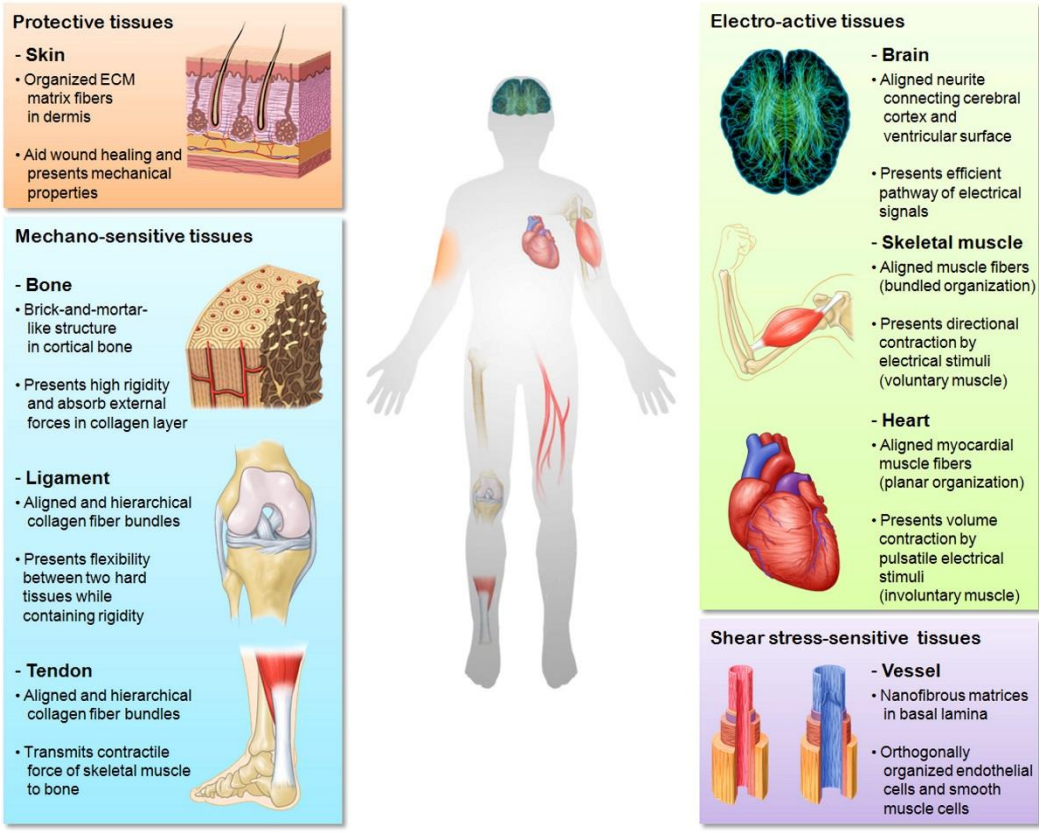

Figure 2.1 Organisation of human tissues showing how they are categorised into protective, mechano-sensitive, electro-active, and shear stress-sensitive tissues, with respect to the tissue specific environment, structure and function (reproduced with permission of Kim *et al.*, 2013).

Hence, simply culturing or repopulating cells on a substrate to form a tissue-biomaterial construct, does not guarantee that it would restore tissue and organ bio-functionality. For example, patients that receive prosthetic vascular grafts tend to have a comparatively high failure rate, due to the onset of thrombosis and neointimal hyperplasia. This usually occurs within a short period following bypass surgery. It is thought that this is due to a lack of endothelial coverage and a mismatch in the mechanical properties of the construct (Tiwari *et al.*, 2001). High

risks of prosthetic trachea failure is also frequently observed due to lack of mechanical strength and flexibility, leakage of intestinal fluid, and slow ciliated epithelium regeneration (Chua *et al.*, 2013). Hence, the ideal material should provide support for cells and promote cell organisation before/after transplantation and mimic the extracellular matrix in mammalian tissues, which serves as a scaffold to promote cell adhesion, migration, alignment, proliferation, etc.

It is important to know what surface topography the native cells have and how it affect cell behaviours interacting *in vivo*. The responses of cells to naturally occurring surface topography *in vivo* can be studied by either directly extracting the (ECM) from animal tissues, or replicating natural extracellular matrix (ECM) architecture through advanced nano-microfabrication technology. The next section will discuss a variety of natural ECM surface topography.

2.4 Organisation and Scale of the Extracellular Matrix

In order to design an appropriate surface or scaffold for cells, it is critical to understand the composition, organisation and scale of the ECM. *In vivo*, the ECM provides structural support and physical cues for cell attachment, migration, proliferation, and gene expression. When grown on 2D substrates many cell types change their phenotypes, for example smooth muscle cells and chondrocytes. This is because the 2D environment is alien to cells and lacks the complex three-dimensional physiochemical cues that are present *in vivo* and which are required for normal cellular function. Such cues are generated, in part, by surface features ranging from the nanometer to millimeter scale. The ECM is a highly organized structure that consists of a mixture of extracellular macromolecules (fibrous proteins and proteoglycans) such as collagen, elastin, fibronectin, laminin, etc. which are embedded in a polysaccharide gel-like substance. Interestingly, some of these extracellular macromolecular structures possess complex nanoscale features. For instance, collagen is the most abundant structural protein in mammalian connective tissue contributing 25% of the total protein mass. The collagen fibril has a notable banding pattern that is formed by periodical spacing, organization

and cross-linking between tropocollagen molecules arranged along a helical axis. A schematic diagram of collagen assembly and organization is shown in Figure 2.2.

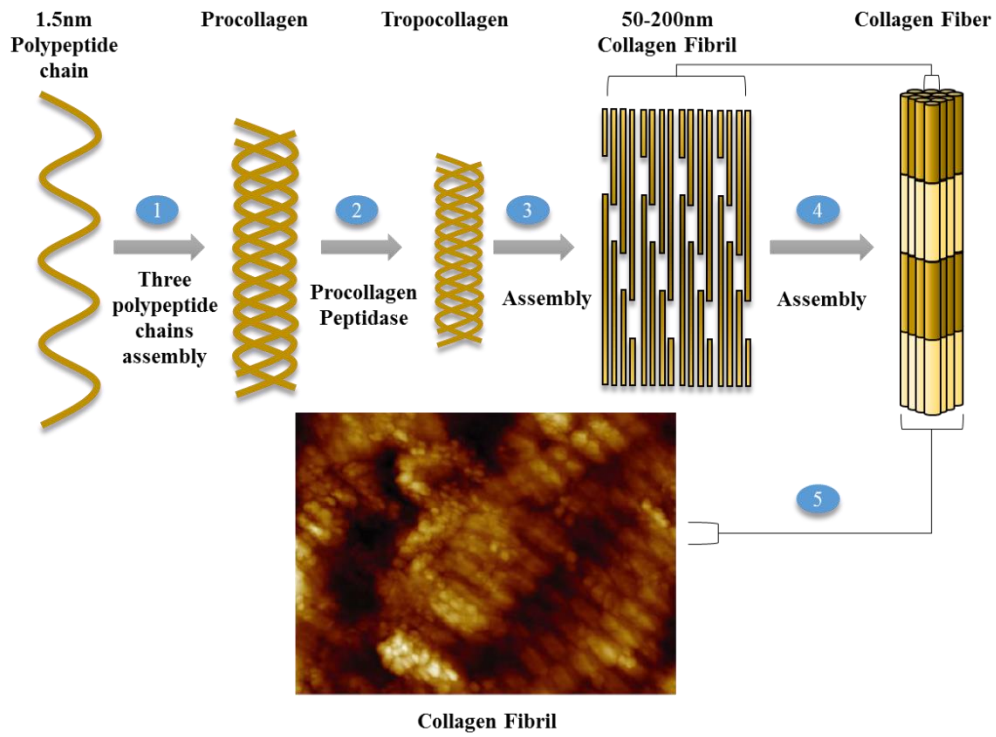

Figure 2.2 The synthesis process of a collagen fiber. (1) It is secreted in the form of a polypeptide chain 1.5nm in diameter and 300nm long. (2) Three polypeptide chains wind together into a tropocollagens fiber. (3) Many helical tropocollagen align side by side along a helical axis and cross-link to form a 50-200nm collagen fibril. (4) The collagen fibrils assemble into collagen fibers (5) AFM image of a collagen fibril showing a distinctive banding pattern (reproduced with permission of Hassenkam *et al.*, 2004).

This organisation of extracellular macromolecules is able to generate highly complex three dimensional ECM sheets. These sheets contain a range of primary structures both on the micro and nanoscale such as grooves, pits, pores, pitched ripples and fibres. These ECM sheets can then fold into a secondary organisation, having features on the microscale, or tertiary organisations with features on the mesoscale, structures to form a hierarchical organisation which is specific for the immobilisation of different cell types and which ultimately characterises the

organisation of the tissue/organ scaffold and function of the tissues, such as muscle contraction, signal transmission through neuron and etc. (Wang and Carrier, 2011).

Given the complexity of the ECM and its importance in controlling cell behaviour it is important to understand its basic architecture and characteristics in animal tissues and how ECM structure relates to processes within the cell. Generally, ECM in animal tissues exists in two forms: basement membrane and the stromal matrix (Davies, 2001). Different types of ECM in the basement membrane and the stromal matrix, taken from different locations from mammalian tissue, have been extensively studied and characterized using techniques such as scanning electron microscopy (SEM), transmission electron microscopy (TEM) and atomic force microscopy (AFM). These studies have showed that ECM samples taken from different tissues have specific organisations, architecture and feature dimensions and which are important to support local tissue bio-functionality.

2.4.1 Basement Membrane Topography

The ECM is folded into three dimensional hierarchical basement membranes which provides adhesion sites that support the overlying epithelial cells and compartmentalises the epithelial cells from other cell types (Yurchenco, 2011). The basement membrane structure is formed by cross-linking of laminin, type IV collagen, entactin and perlecan (Martin and Timpl, 1987). The basement membrane organisation, architecture and feature dimensions varies, depending on the specific location of the ECM within the animal tissues. For example, Kawabe *et al.* examined the basement membrane of human plantar skin using SEM and found that the structure is comprised of millimetre scale primary and secondary grooves and dermal papillae. The primary grooves were wider than the secondary grooves and the bottom of the primary grooves exhibits a microscale reticulated appearance with a net-like arrangement of collagen fibrils which contain holes (the ducts of eccrine sweat glands) running along the grooves (Figure 2.3a and e). In contrast the secondary grooves contained a series of rough parallel microridges along the grooves. The millimeter scale microridges in between the primary and

secondary grooves were comprised of microscale finger-like projections known as dermal papillae (Figure 2.3b). In comparison to the microridge arrangement pattern on secondary grooves, the dermal papillae were found to consist of invaginated microridges having a spiral arrangement and which are terminated as broad sinuous folds on the papillary tips (Figure 2.3c and d). The complexly folded microridge features that cover the secondary grooves and dermal papillae are supported and assisted by a complex honeycomb like structure under the basal lamina, formed by aggregation of 60-70nm dermal collagen fibrils (Kawabe *et al.*, 1985).

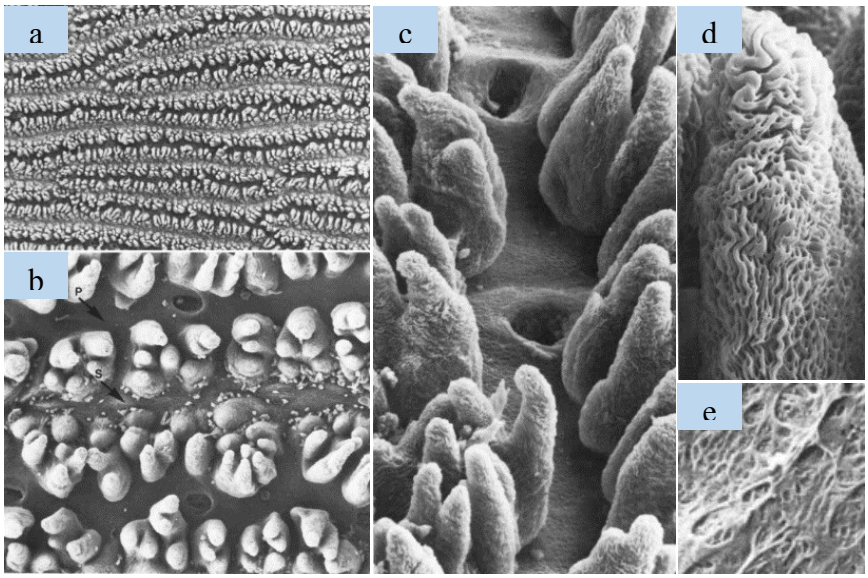

Figure 2.3 (a) SEM image of plantar dermis after epidermis removal. (b) The image revealed that the dermis consists of primary (P) and secondary grooves (S). (c) The primary groove and dermal papillae contain microstructures, known as dermal papillae, on their surface. (d-e) High magnification SEM image showing that the dermal papillae consist of invaginated microridges with a spiral arrangement and the primary groove has a reticulated appearance (reproduced with permission of Kawabe *et al.*, 1985).

In contrast, the human bronchial basement membrane was also studied under SEM which revealed a porous topography. The pores were found to be oval shaped with a mean pore diameter of 1.75µm (range, 0.6 to 3.85; SD=0.67µm). The mean pore density was found to be 863±404 pores/mm^2 (range, 208-2337; SD=404 pores/mm^2) (Howat *et al.*, 2001)(Howat *et al.*, 2002).

A study on porcine oesophagus basement membrane morphology showed that the porcine oesophagus basement membrane was constructed from interwoven fibres and pores which were unevenly distributed. The resulting measurements showed that the fibre diameter was 66nm (range, 28 to 165; SD=24nm), the mean pore diameter was 177nm (range, 29 to 638; SD=116nm) and the interpore distance was approximately 198nm (range, 49 to 354; SD=61nm) (Li *et al.*, 2012).

2.4.2 Stromal Matrix Topography

Bone surface topograpghy is important for bone regeneration. Many researchers have showed that high nanometer levels of surface roughness enchances osteoblast adhesion and longer term functions such as collagen, alkaline phosphate activity and calcium-containing mineral deposition (Webster and Ejiofor, 2004)(Price *et al.*, 2004)(Liu *et al.*, 2006).

Bone is mostly composed of corticol and cancellous bones (spongy bone), with an estimated elastic moduli of 0.76-20 GPa. Its main function is for structurual support and to endure external mechanical forces (Rho *et al.*, 1993). Hassenkam *et al*. examined intact and fractured trabecular bone using AFM. The high resolution AFM images revealed that the corticol trabecular bone was densely interwoven with collagen fibrils with each fibril possessing a 67nm banding pattern (Figure 2.4). The average fibril diameter was found to be ~100nm (range, 50-200nm). In some areas, the collagen fibres on the trabecular surface were found to be mineralised into plate-like mineral cystals known as carbonated apatite (Figure 2.4a and b). The thickness of the plates-like mineral crytal were found to be ~3-10nm with width of ~30-120nm. Compared to the corticol area, the cancellous bone is less dense, less stiff and flexible with a porous or spongy apprearance (Hassenkam *et al.*, 2004). Other stromal matrices within the body have different ECM organisation, architecture, and feature demensions to act as load-bearing structures, including tendon, cartilage and ligament.

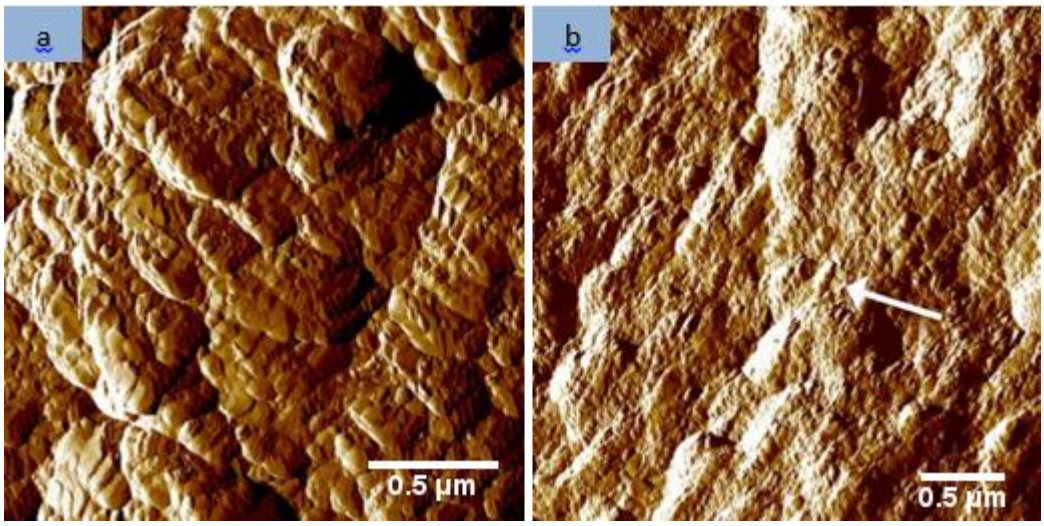

Figure 2.4 (a) AFM image showing mineral plates packed into fish scale arrangement on the collagen fibrils, (b) The white arrow shows the naked collagen fibrils (reproduced with permission of Hassenkam *et al.*, 2004).

The studies discussed in Sections 2.4.1 and 2.4.2 have showed that ECM from different locations of animal tissues consists of topography of pores, grooves, ridges, and ripples. Howat *et al*. suggested that the pores on the basement membrane (human bronchial airway) may serve as a route for immune cells to migrate between the epithelial and mesenchymal compartments (Howat *et al.*, 2001). However, the functions of other surface features for cells still remains unknown.

2.5 Extracellular Matrix in Biomedical application

Recognition of the importance of the structure and role of the ECM in major cellular processes has led to the development of acellular matrix products that aim to stimulate wound healing. Currently, there are a variety of natural ECM-based materials that are commercially available for dermal regeneration, such as

INTERGA®, OASIS® and Unite®. INTEGRA®, for example, is a bilayer wound healing dressing composed of cross-linked bovine tendon collagen and glycosaminoglycan (chrondroitin-6-sulfate) and a semi-permeable polysiloxane silicone layer.

Wound healing is a complex physiological process which involve in tissue repairs and restores function to damaged organ. The process is divided into four stages: inflammation, proliferation, granulation, and matrix remodelling (Demidova-Rice *et al.*, 2012). During the wound healing progress, an endogenous collagen matrix is deposited by the infiltrating fibroblast cells. This is followed by scaffold degradation and remodelling, as the patient's cells regenerate at the damaged site. This product has been shown to be useful for deep partial-thickness and full-thickness burn wounds, full-thickness skin defects with different aetiologies, chronic wounds and soft tissue defects. The collagen-glycosaminoglycan complex serves as a porous scaffold for infiltration of fibroblast cells, macrophages, lymphocytes and capillaries derived from the wound bed, thus accelerating the wound healing process. OASIS® is another class of ECM-based material which is derived from porcine acellular small intestinal submucosa. Unlike other collagen based scaffolds, OASIS® complex scaffold provides an optimal environment which allow cellular and vascular infiltration for tissue bio-functionality and structural restoration. OASIS® is typically used in all partial and full thickness wounds, superficial skin burns and second-degree skin burns.

The main component of the above product is type I collagen, which is normally harvested from a cadaver, or from animal tissues such as the dermis, small intestine submucosa and pericardium. This tissue is subsequently treated to remove all cellular material and hence obtain only the collagen matrix. Although the use of acellular matrices has shown promise there are potential drawbacks including the risk of infectious agent transfer and immunological rejection. The current clinical use of acellular matrices also remain limited, due to the high cost in manufacturing, transport, preservation and storage of these devices (International consensus, 2001).

The alternative clinical solution for acellular matrix replacement is the creation of an artificial ECM. This can be achieved by bio-mimicking the ECM architecture

through advanced micro and nanofabrication technology, or to generate a user design topography which gives more predictable and consistent performance due to the production of a reproducible well-defined topography (the detail of the technology and cell responses will be discussed in the following chapter).

Chapter 3

3.0 Advanced Micro- Nanofabrication Technology for Tissue Engineering

3.1 Microelectromechanical Systems for Tissue Engineering

As previously mentioned in Chapter 2, studies have been carried out in order to better understand the ECM organisation, its arrangement, topography characteristics and its functions, so as to improve artificial ECM construction for specific applications. The most challenging feature of the ECM architecture to reproduce is its very small dimensional sizes, which can be on the nanoscale. Numerous technologies have been developed to bio-mimic natural ECM topography and also to fabricate human designed patterns to control cellular function. The most widely used micro and nanofabrication methods for tissue engineering have been adopted from the well-established semiconductor industry and in particular in the manufacture of devices such as microelectromechanical systems (MEMS). Amongst these techniques are included photolithography, electron beam lithography, focused ion beam lithography, ion projection lithography and X-ray lithography. All of these techniques are followed by some form of wet or dry etching process, with the final surface geometry profile being determined by an etching process. The main methods for engineering surfaces that control cell growth will be discussed below.

3.1.1 Photolithography

Conventional optical lithography is the most popular and widely used technique for biomedical applications, because it is able to produce a well-defined and precise microscale features. (McMurray *et al.*, 2011). The lateral dimensions that can be produced by photolithography is of the order of 100 to 500nm, with resolution being dependent on the illuminating source. The resolution of photolithography is expressed using Rayleigh's criterion below:

$$Resolution = k_1 \frac{\lambda}{NA} \tag{3.1}$$

Where k_1 is a constant dependent on the photoresist being processed, with this value typically ranging from 0.5-0.8. the parameter λ is the illumination source wavelength and NA is the numerical aperture of the lithography objective lens, which ranges from 0.5-0.8 (Harriott, 2001). As a result, the shorter the illuminating wavelength, then the smaller are the features that can be generated (Table 1)(Xia and Whitesides, 1998).

Table 3.1 Lithography methods

Illumination Source	Wavelength (nm)	Smallest lateral dimension that can be produced (nm)
UV, g line of Hg lamp	436	500
UV, i line of Hg lamp	365	350
DUV, Krypton fluoride (KrF) excimer laser	248	250
DUV, Argon fluoride (ArF) excimer laser	193	180
DUV, fluorine (F_2) excimer laser	157	120
DUV, dimer discharge from an argon laser	126	100

Many researchers have employed photolithography to generate features such as grooves, ridges, pores and pits to mimic the natural ECM architecture for cell studies. A simplified diagram of the photolithography process is shown in Figure 3.1.

In general, lithography is a process that transfers a computer-aided design (CAD) layout onto a substrate by means of light. The process begins with the transfer of a computer designed pattern to a photomask, made from either borosilicate glass, soda lime, or quartz. A chromium coating is applied to the photomask using either electron beam lithography, or optical direct write lithography. The patterned chromium layer then serves as an opaque region to prevent the UV light exposing the photoresist.

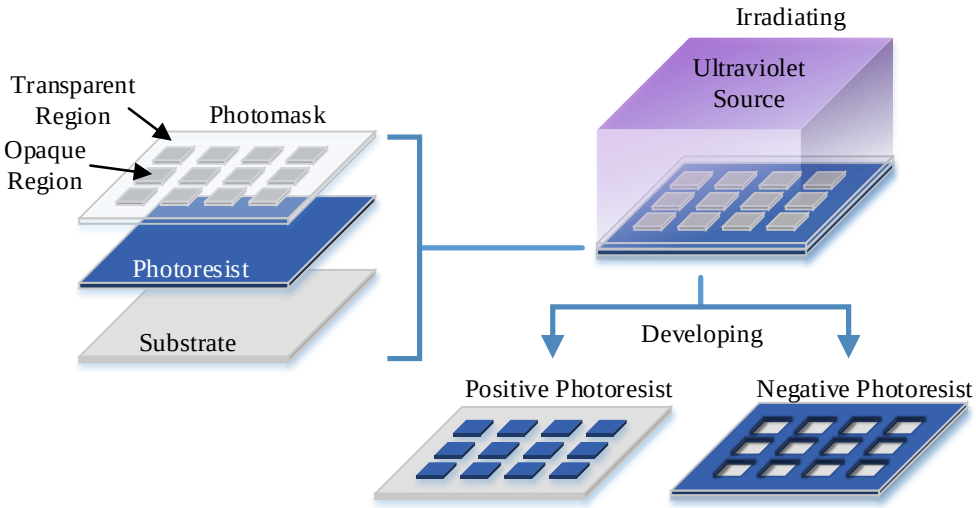

Figure 3.1 Schematic diagram of the photolithographic process. The substrate is spin-coated with either a positive or negative photoresist and exposed to UV radiation to alter the chemical structure. Positive photoresists dissolve in the developer solution after being exposed to UV, whereas negative photoresists become difficult to dissolve.

Once the photomask has been obtained, the substrate is spin coated with a layer of photoresist. Two different types of photoresist are commercially available: positive and negative. For a positive photoresist, the UV exposed region changes the resist's chemical structure, by breaking the polymer into shorter chains which

become soluble in a developing fluid. Negative photoresists behave in the opposite manner, where the UV exposed region polymerizes the polymer to longer molecular chains, which become difficult to dissolve. The photoresist is then aligned to the photomask and exposed to the UV light source. Finally, the transferred pattern from the mask is developed in the developer solution, and the pattern is either used as a mask in a further etching process, or is directly used in a biomedical application (Betancourt and Brannon-Peppas, 2006).

SU-8 is an EPON SU-8 epoxy resin negative photoresists is widely used by the biochemical industry in Bio-MEMS applications including, bioreactors, biosensors and biomolecule immobilisation related assays. This is due to its excellent mechanical properties, thermal stability, etch-resistance, chemically stability, and biocompatibility (Nemani *et al.*, 2013). It therefore, can be applied directly to medical devices without any sign of cytotoxicity (Lu *et al.*, 2006). Also, SU-8 allows the generation of relatively tall structures approximately >200µm in height and which can generate high relief micro-patterns (Guerin *et al.*, 1997).

3.1.2 Electron Beam Lithography and Focused Ion Beam Lithography

Electron Beam Lithography (EBL) was first developed in 1960 and was based on the principles of the already existing electron microscope (Hahmann and Fortagne, 2009). Electron Beam Lithography consists of a heated filament inside the microscope that emits electrons which are focused using electrostatic lenses into a narrow beam, creating a spot diameter size in the region of 2-5 nm. EBL can create features that are below 10 nm (Wanzenboeck and Waid, 2011). The focused beam is controlled by defection coils, which enable the user to fabricate an arbitrary geometry, by precisely exposing the focused electron beam onto the e-beam resist. This technique is known as maskless lithography (Alttissimo, 2010).

The e-beam resist used for EBL must be compatible to high energy forward scattered, back scattered, and secondary electrons (Broers *et al.*, 1996). The most common e-beam resist used to produce features below 50 nm is

polymethylmetacrylate (PMMA), which requires an exposure dose above 0.2μC/μm². However, greater resolution (i.e. fabrication below 20nm) requires the use of inorganic resists, such as hydrogen silsesquioxane (HSQ) or aluminium fluoride (AlF3) and a higher exposure dose (Grigorescu and Hagen, 2009). The drawbacks of this method are that a longer exposure time is required for a single scanning electron beam, in order to fabricate using an e-beam resist, thus resulting in slower processing time. Therefore, EBL is only used to write photomasks for optical lithography and other high value applications (Wanzenboeck and Waid, 2011).

Focused ion beam (FIB) lithography is similar to EBL, the only difference being that the FIB system uses a focused ion beam from a gallium ion source. Furthermore, FIB provides a greater capability than EBL including, (i) the generation of nanopatterns on e-beam resists, (ii) milling away atoms by physical sputtering, (iii) material deposition and (iv) direct material modification by ion induced mixing (Fu and Ngoi, 2004).

3.1.3 Etching Process

Once the pattern has been lithographically established by photolithography or EBL, it can then be transferred to the substrate underneath the protective mask. However, the final topographical profile will depend on which type of etching process is employed. The etching process can either be isotropic or anisotropic. For isotropic etching, the etching rate is the same in the vertical and horizontal directions. In contrast, to anisotropic etching, the etching rate is different, in both the vertical and horizontal directions. Both etching processes utilize a liquid chemical and gaseous physico-chemical mechanism, known as a wet and dry etching process (Ziaie *et al.*, 2010).

The isotropic wet etching rate is even in all directions and often generates a hemispherical or curved profile. In contrast, anisotropic wet etching generates a pyramidal profile, because the etching rate is different for various crystalline materials and depends on the crystal face being exposed to the etchant. For

example, the effect on silicon can be highly anisotropic, resulting in a pyramidal shaped profile after etching by anisotropic wet etching agents such as potassium hydroxide (KOH), ethylenediamine pyrocatechol (EDP), and tetramethylammonium hydroxide (TMAH)(Yi *et al.*, 2000).

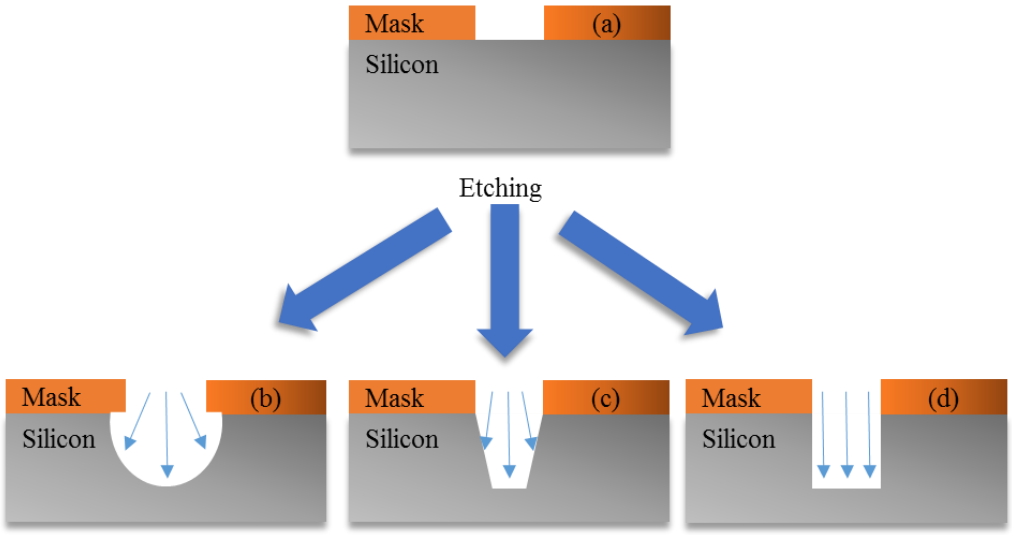

Figure 3.2 The effects of isotropic and anisotropic processes on final surface profile. (a) The desired pattern has been transferred onto the silicon substrate. (b) Isotropic wet etching generates a hemisphere shaped profile. (c) Anisotropic wet etching generates a pyramidal shaped profile. (d) Anisotropic dry etching generates a straight flat bottom planar profile.

Dry etching technology achieves a higher anisotropic etching rate and prevents undercutting. Reactive ion etching (RIE) is the most popular anisotropic dry etching process, using a chemical process to increase the etching rate and resolution. RIE, combined with RF (radio frequency) electromagnetic field generated plasma, ionises a gaseous mixture into reactive species and accelerates them towards the surface of the material. The chemical reaction occurs on the material surface forming a volatile by-product. After the reaction, the by-product diffuses away, to start another new cycle (Jansen *et al.*, 1996). The schematic diagram shown in Figure 3.2 shows the effect of isotropic and anisotropic etching on the final surface profile

3.1.4 The Disadvantages of Microelectromechanical Systems for Tissue Engineering

The main disadvantage of the MEMS technologies discussed above is that they must operate in a quality class clean room, where the air is constantly filtered, to achieve a particle density of 1-10 particles per cubic foot. Furthermore, the photo and e-beam resist polymers are very sensitive to temperature and humidity variations during the fabrication process and must be precisely controlled. Variation in temperature and humidity leads to changes in resist chemical properties and chemical reaction rate. It is also important that the illumination within the clean room is carefully controlled so as to eliminate the risk of inadvertently exposing the light sensitive resist. Therefore, the lighting within the clean room should operate in the yellow part of the spectrum and out of the photo-activation resist wavelength.

State of the art MEMS technology has revolutionized and empowered biologists to generate feature dimensions from the micro scale down to the nanoscale, the facilities are very dependent on the expertise of operators, and such facilities carry high operating costs and typically have limited accessibility. Other limitations of photolithography include being confined to flat surfaces and restricted to a limited set of photoresists that will integrate well with biomaterials. Although electron beam lithography, focused ion beam lithography and ion projection lithography are maskless techniques it is nevertheless true that the fabrication process are relatively slow and expensive.

To address these issues many advanced technologies have been developed. These allow the processing of a variety of materials to generate features at the micro and nanoscale and include soft lithography, electrospinning and direct laser microfabrication techniques. Such techniques are generally more accessible than other approaches and require lower operating costs.

3.2 Soft lithography

Soft lithography refers to a collection of inexpensive methods to transfer or replicate micro/nano features on a substrate. Soft Lithography consists of three types of techniques; micro-contact printing, replica moulding, and stencil patterning. The first phase of soft lithography is the micro/nanofabrication of a 'master' template using ready-available technologies such as photolithography, e-beam, and direct laser writing. In the second phase, a replica of the master template is made by producing a mould using polydimethylsiloxane (PDMS). This mould is an inverse to the master template. PDMS is used because of its biocompatibility, and good thermal (from −100 ºC up to +100 ºC), mechanical (shear modulus G between 100 kPa and 3 MPa) and optical properties (Lötters *et al.*, 1997). The main advantages of soft lithography is that once the reusable mould has been produced, none of the following procedures require clean room manipulation (Betancourt and Brannon-Peppas, 2006).

Micro-contact printing (µCP), also known as micro-stamping, produces a PDMS mould from the original master template to serve as a stamp. The 'ink' used in the stamping process can be polysaccharides, peptide, proteins, or other molecules. These molecules are transferred in the shape of the machined pattern on a receiving substrate. Moreover, a photoresist can be micro-stamped on to the substrate to form a protective layer for etching or film deposition processes (Whitesides *et al.*, 2001).

The second type of soft lithography technique is replica moulding. The replicated PDMS mould serves as a master template. Liquid pre-polymer fills the recessed regions of the mould. This is followed by pressing the mould against the substrate, then thermally or UV curing, depending on the type of pre-polymer.

The third type of soft lithography technique is stencil patterning. In this method the master template is sandwiched between two substrates to prevent the PDMS covering the master template. The end result of this process generates holes that resemble the pattern on the master template (Zhao *et al.*, 1997).

The advantages of this soft lithography technique is that a wide range of biomaterials can be used to repeatedly replicate features, from the reusable PDMS

mould, to different types of substrates, or same the substrate (Xia and Whitesides, 1998). It also allows the transfer of nano and micro features to non-planar surfaces using flexible PDMS moulds. However, the main disadvantage of the soft lithography method is that it generate artifacts due to deformation of the elastomeric stamp or mould (Zhao *et al.*, 1997).

3.3 Polymer Electrospinning Technique

Electrospinning has recently attracted much interest in biomedical applications, due to its simplicity and capability of producing micro and nanometer scaled fibres, which can form fibrous scaffolds that resemble the natural ECM. In contrast, the conventional mechanical fibre spinning approaches can only produce fibres with diameters that are larger than that of the natural ECM. Electrospinning is a technique used to produce fibres, having relatively small diameters (from<3nm to over1µm), from a polymer solution through electrostatic forces. In order to generate electrospun fibres, a DC voltage of several tens of kilovolts (kVs), must be applied to produce a strong mutual electrical repulsive force to overcome the weaker surface tension in the charged polymer liquid. The basic electrospinning system consists of three major components: (i) high voltage power supply, (ii) spinneret, and (iii) grounded collecting plate. Currently, there are two basic setups of electrospinning systems, vertical and horizontal as shown in Figure 3.3. The electrospinning process begins by applying an electric field or polarity to the liquid polymer. The polymer liquid becomes charged and the electrical repulsive forces overcome the weaker surface tension, causing the polymer droplet at the front of the spinneret to become stretched. Eventually, at a critical point, a stream of polymer liquid is ejected from the tip of a Taylor cone (Figure 3.3) forming an unstable liquid jet, which draws towards the opposite polarity of collecting plate. At the same time, the solvent is evaporated, leaving the polymer behind on the collector plate, while ejecting the polymer into the space between the spinneret and collecting plate (figure 3.3a) (Taylor, 1969).

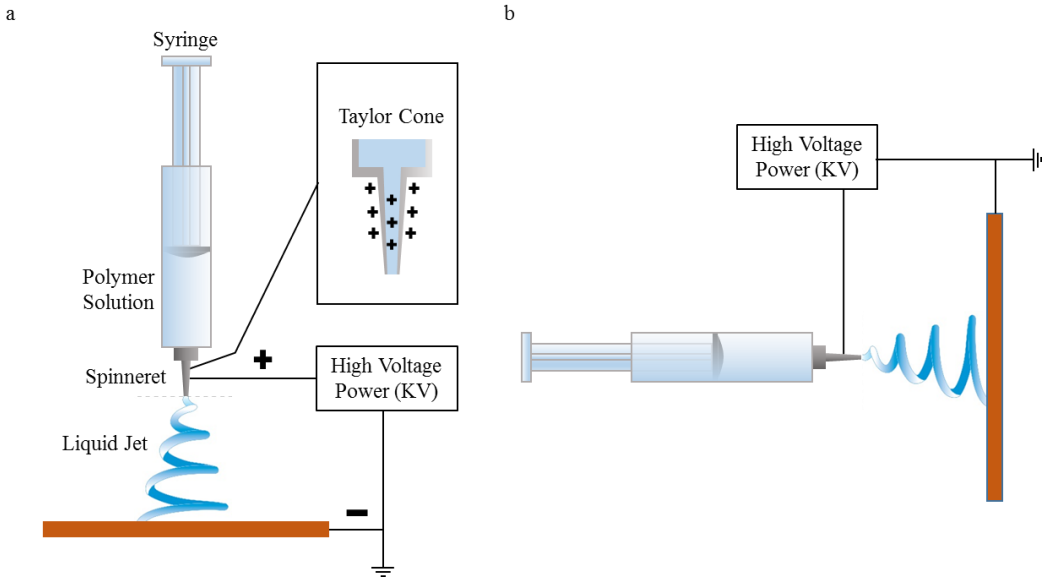

Figure 3.3 Schematic diagram of two basic electrospinning system setups: (a) vertical setup and (b) horizontal setup.

The electrospinning process relies on three sets of parameters: solution parameters (concentration, conductivity, molecular weight, and surface tension), process parameters (electric field, tip to collector distance and feeding rate), and environmental parameters (humidity and temperature). Polymers with a low concentration produce micron sized particles after solidification, which is similar to low molecular weight polymers (Figure 3.4a). Intermediate molecular weight polymers and polymer concentrations result in beaded nanofibres (Figure 3.4b). High polymer concentration increases fibre diameter and the beaded appearance is seen to disappear on the fibre surface (Figure 3.4c and d) (Jiang *et al.*, 2004). The polymer molecular weight is interrelated to polymer threshold concentration, i.e. lower molecular weight polymers require higher polymer concentration (Koski *et al.*, 2004).

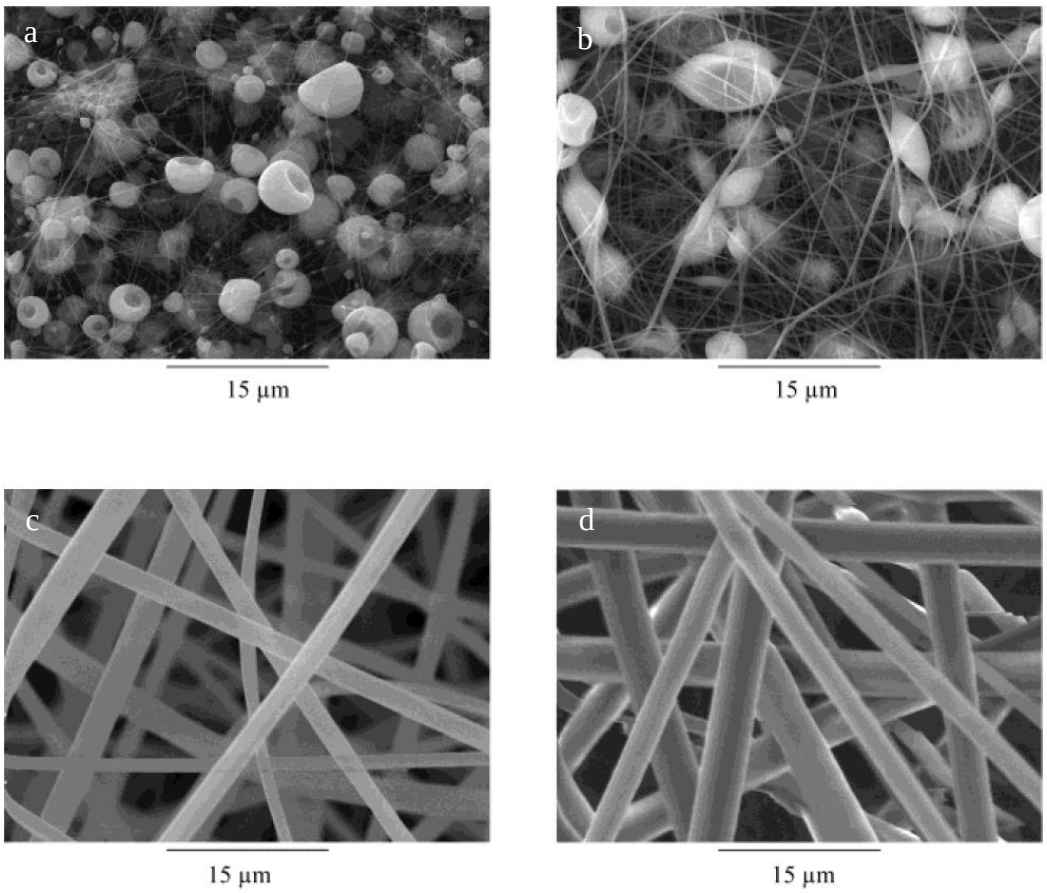

Figure 3.4 SEM images of electrospun dextran membranes with different dextran concentrations: (a) 0.5g/mL, (b) 0.65g/mL, (c) 0.75g/mL, and (d) 1.0g/mL (reproduced with permission of Jiang *et al.*, 2004).

Fong *et al* showed that the bead and beaded fibre formation was driven by surface tension. They found that the beaded fibre appearance decreased when increasingly mixing more ethanol into the water to lower the surface tension of poly(ethylene oxide) (PEO). Disappearance of the beaded fibre was observed at mass ratio of ethanol/water of 0.448 which is 67g of water and 30g of ethanol (Fong *et al.*, 1999).

As mentioned previously, sufficient electric field/voltage must be applied in order to introduce to the liquid polymer to overcome the surface tension. Jeun *et al* studied the effects of voltage on electrospinning by varying the voltage range from 5kV to 25kV. The results showed that the weak electric field generated by using a voltage of 5kV was unable to overcome surface tension and viscoelasticity. Further increases in the electric field, by increasing the voltage to 20kV, were found to lead to an increase in the fibre diameter, which was due to the liquid being removed more quickly at the tip of the capillary as the jet was ejected from the Taylor cone.

Whereas at 25kV, corona discharge was generated and this inhibited the electrospinning process (generating neutralising ions and neutralising the charges on the jet). Changing the tip to a larger diameter was also found to increase fibre diameter. However, at the same time it also increases the solution flow rate. If the solution flow rate exceeds a critical point, then the delivery rate will exceed the solution removal rate and this will lead to an unstable jet and hence the fibres having a larger diameter (Jeun *et al.*, 2007).

The collecting plate used for electrospinning processes are usually a metal screen plate or a rotating mandrel. Flat metal screen plates usually produce random fibre alignment, due to instability of the highly charged liquid jet. Use of a rotating collecting drum has been shown to be able to produce fibres aligned parallel to each other. However, alignment is dependent on the type of rotating collector and rotating speed. Heath *et al*. demonstrated fabricating aligned fibres by electrospinning methacrylic terpolymer biomaterials on a rotating mandrel. It was found that the degree of fibre alignment increased when increasing the rotation speed of the collector from 0 to 15.2m/s (Figure 3.5) (Heath *et al.*, 2010).

Humidity, has also been shown to influence the electrospinning process. For example, Casper *et al*., showed that varying the humidity (<25%, 31- 38%, 40-45%, 50-59%, and 60-72%) resulted in changes to the morphology of the electrospun fibres. The workers also showed that increasing the humidity resulted in an increase in the pore diameter on the fibre surface (Casper *et al.*, 2003). Moreover, changing the temperature was found to change the physical properties of the solution such as viscosity, surface tension and conductivity, all of which will affect the electrospinning process (Mit-uppatham *et al.*, 2004).

The advantages of electrospinning are that it can be relatively easy to electrospun fibers within the range of <3nm to 1µm, the process is easy to learn and has low operating and capital cost. The main disadvantage of electrospinning techniques are that then cannot precisely control where the fiber is deposited on the collecting plate, although a large cylindrical mandrel with a high rotational speed could force fibre alignment. However, with this technique there is an inability to control the spacing between the electrospun fibres.

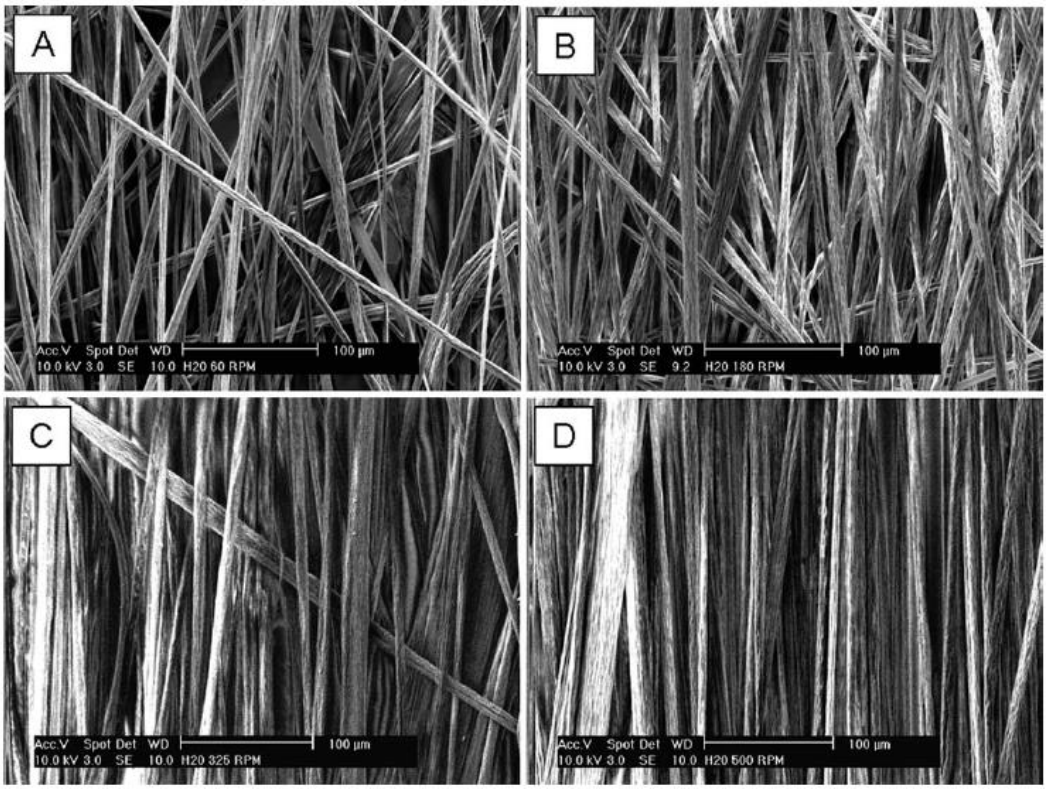

Figure 3.5 SEM images of fiber alignment generated using different speeds of the rotating collector: (a) 1.8 m/s, (b) 5.5 m/s, (c) 9.9 m/s, and (d) 15.2 m/s (reproduced with permission of Heath *et al.*, 2010).

3.4 Direct Laser Patterning

The term direct laser patterning can be defined as creating patterns by directly irradiating a surface using a laser. The laser set-up can be either a fixed-laser beam, with a movable substrate on a multi-axis computer control translation stage (Figure 3.6a), or a moveable laser beam controlled by a galvanometer, which uses an x-y axis mirror to reflect the laser beam (figure 3.6b).

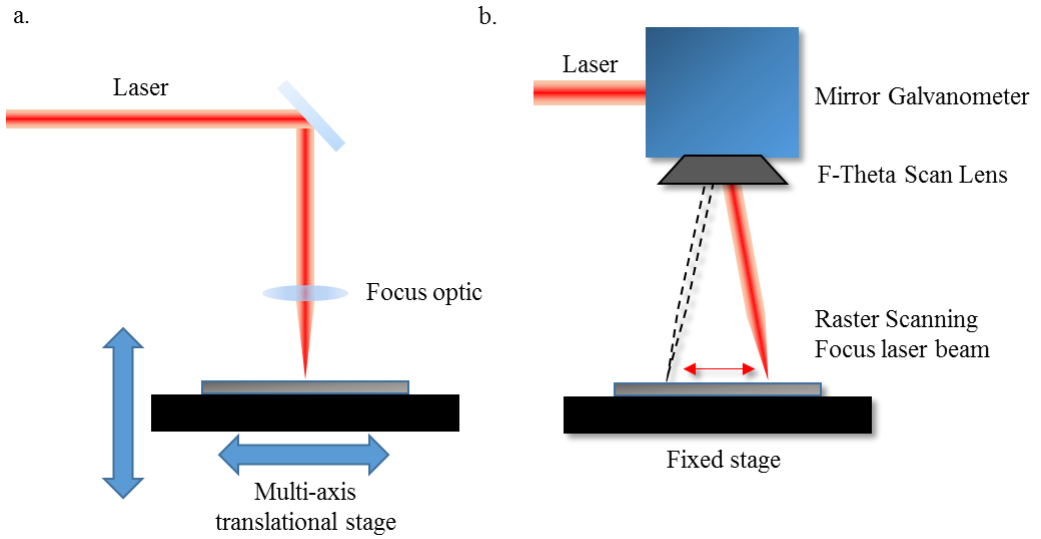

Figure 3.6 Schematic diagram of a laser set-up for direct laser patterning. (a) Laser set-up with a fixed laser beam and a multi-axis movable stage. (b) Moveable focused laser beam controlled by a mirror galvanometer.

Direct laser patterning is usually carried out using a solid state or carbon dioxide laser system, because these lasers generally exhibit good beam quality. They also have a laser beam profile which is related to a low M^2 factor number and propagate in a well-defined Gaussian beam mode with low divergence. Laser processing parameter optimisation is very important for direct laser patterning, because the ablation relies on the overlap laser pulse density, hatching spacing (laser translational distance) and the direction of movement of the substrate. Furthermore, the depth and roughness are determined by the laser power, scanning rate and number of passes. Ulerich *et al.*, showed that a micro-textured Ti-6Al-4V surface with micron size spacing, grooves and walls. In contrast, when a larger spacing was used it produced shallower grooves having lower sloped walls. The authors

also showed that increasing the laser energy can be used to generate surfaces having sub-micron scaled topographies, (e.g. pillars) which are generated by a melting effect (Ulerich *et al.*, 2007).

The laser ablation process can be either photo-thermal or photo-chemical ablation. Photo-thermal ablation mainly occurs using lasers having long wavelengths and low photon energy (in the visible and infrared spectrum), which transforms the excitation energy into heat. If long laser pulses (milli-to nanoseconds) or continuous wave (CW) lasers are used, the heat will conduct away from the bulk material. Photo-chemical ablation mainly occurs in the ultraviolet spectrum, where the absorbed photon is energetic enough to break the covalent chemical bond within the material without converting to heat. However, choice of laser source is material-adsorption dependent, especially with the ablation process through single photon absorption by CW or nanosecond duration laser pulses. However, ultra-short pulse (pico- and femtosecond) lasers generate a high instantaneous intensity, which significantly decreases absorption depths, through phenomena a such as optical breakdown or multiple photon absorption (Brown and Arnold, 2010).

Moreover, laser pulse length will also affect the ablation quality, due to different ablation mechanisms. A study by Leitz *et al* showed the ablation mechanisms of micro, nano, pico and femtosecond laser pulses on stainless steel substrates (Leitz *et al.*, 2011). The authors showed that at the first phase of the microsecond laser ablation process, it can be clearly seen that the mechanism is thermal and ablation by evaporation plays only a minor role. The diameter of the ablation zone increases when the number of laser pulses (N) increases up to N=100. They suggested that this was due to thermal incubation effects. As the pulse number increases, the ablation process is dominated by melt expulsion due to evaporation of the material (Figure 3.7).

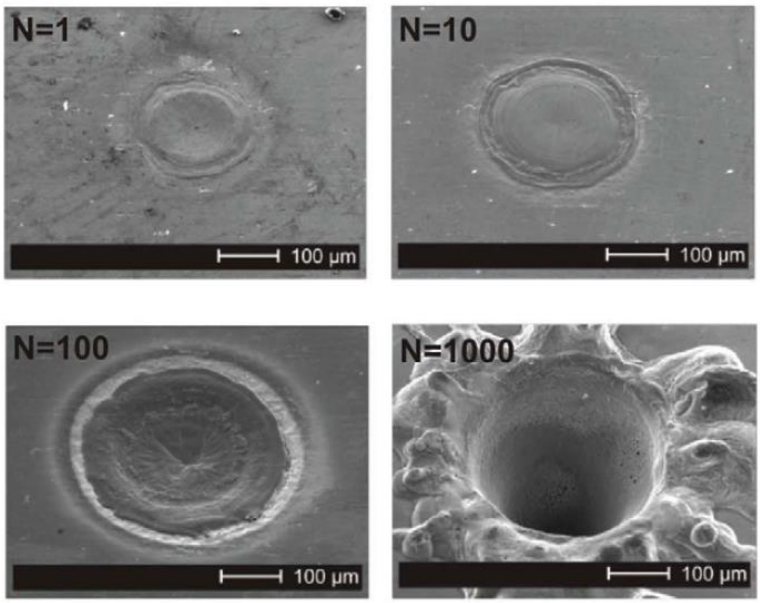

Figure 3.7 SEM images of microsecond laser drilling using laser pulse numbers of 1, 10, 100, and 1000 (reproduced with permission of Leitz *et al.*, 2011).

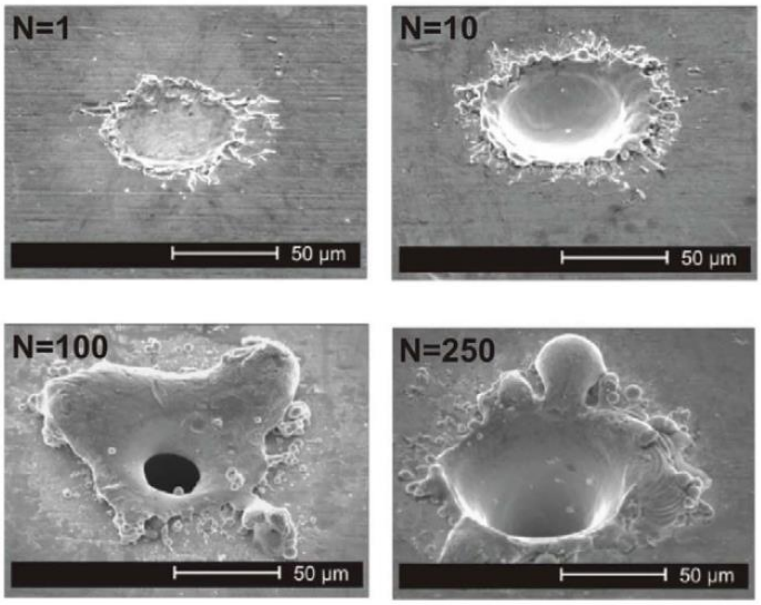

Figure 3.8 SEM images of nanosecond laser drilling using laser pulse numbers of 1, 10, 100, and 250 (reproduced with permission of Leitz *et al.*, 2011).

The authors also showed that the nanosecond ablation process is dominated by classical beam-matter interactions. From the start of the laser pulse-matter interaction, evaporation and melt expulsion occurs, which leads to significant

material removal. With increasing pulse number the diameter of the ablation zone increases. As the drill hole-depth increases, the expulsion of the melt becomes less efficient, leading to a partial reclosure of the hole (Figure 3.8).

In contrast to micro and nanosecond lasers, the picosecond laser pulse ablation process is dominated by laser induced phase explosion, which is due to the formation of a cleft structure in the centre of the ablation spot, with the deposition of droplets and metallic particles (N=500 pulses). The peak fluence ablation per pulse is significantly lower with the picosecond laser, producing only a small increment of the hole diameter with increasing pulse number. When increasing the pulse number, a soft burr at the edge of the processed hole and molten and ripple-like structures were observed at the deeper centre of the hole. Thermal effects were still found to occur because the laser fluence is still higher than the ablation threshold (Figure 3.9).

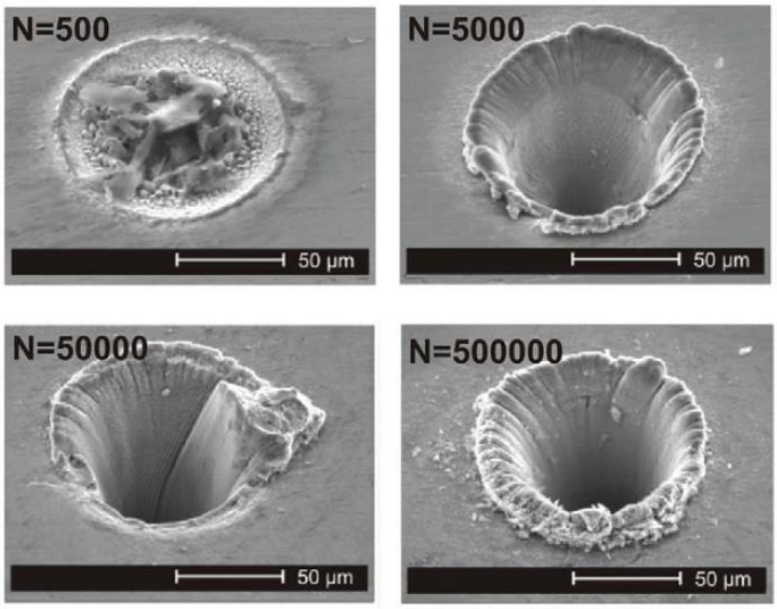

Figure 3.9 SEM image of picosecond laser drilling using laser pulse numbers of 500, 5000, 50000, and 500000 (reproduced with permission of Leitz *et al.*, 2011).

The authors also showed that ripple structures were observed at the edge of the ablation area and fine melt sputter indicated the occurrence of laser-induced phase explosion at the first stage of the femtosecond ablation process. When increasing the laser pulses to N=1000, the burr at the edge of the ablation area increased in

height, with only small increments in width due to material re-condensation. However, further increasing the laser pulse to N=5000 leads to a decrease in the burr height (figure 3.10). The authors suggested that incubation effects in combination with increased absorption at the rough surface caused an ablation of the burr at fluence below the ablation threshold (Leitz *et al.*, 2011).

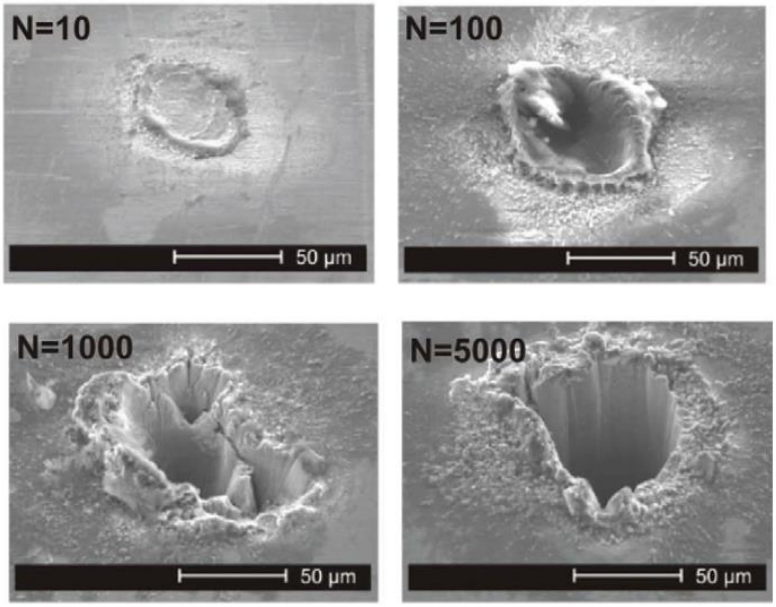

Figure 3.10 SEM images of picosecond laser drilling using laser pulse numbers of 10, 100, 1000, and 5000 (reproduced with permission of Leitz *et al.*, 2011).

The quality of surface patterning is dependent on the laser system used (ranging from micro to femtosecond pulses) and laser parameter optimisation. The main advantages of direct laser pattering is that it allows the user to arbitrarily micro-pattern the substrate with a custom designed micro-pattern through the use of a laser galvanometer or x-y-z computer translation stage. However, the disadvantages of this methods is that the patterning feature size is limited by the diffraction limit and is restricted to a microscale range.

3.5 Direct Laser Interference Patterning

The MEMS manufacturing technology discussed above requires multiple steps and is time consuming (e.g., electron and ion beam lithography) to generate micron and submicron sized periodical structures, especially when processing large areas (i.e. more than several cm^2). However, direct laser interference patterning (DLIP) is a promising maskless direct patterning technique. This method offers an efficient, fast-direct laser micro and nano periodical array patterning on different types of materials including; metals, polymer, and ceramics, achieved through laser interference. The laser interference periodical pattern is generated by coinciding two coherent laser beams at the same area. The periodicity of structure (ʌ) can be manipulated by changing the angle of the two coherent laser beams exposed to the substrate. The smaller the angle between two beam interference beams, the larger the fringe spacing. For example, Bremus-Köebberlinga and Beckemper (2012) showed DLIP polyimide (PI) substrates with varied lateral dimensions of periodic nanogrooves by changing the angles between the two interfering beams. They demonstrated that changing the angle of the laser beam at the 5º, 10º, 20º, and 45º could generate nanogrooves with periodicities of 1000, 500, 250, and 125nm, respectively (Bremus-Koebberling *et al.*, 2012).

The periodical structure (ʌ) equation is shown below:

$$\Lambda = \frac{\lambda}{\sin(\theta_1) + \sin(\theta_2)} \tag{3.2}$$

Where λ is the laser wavelength, θ_1 and θ_2 are the angles of coherent laser beam 1 and beam 2 that are exposed to the substrate as illustrated in Figure 3.11.

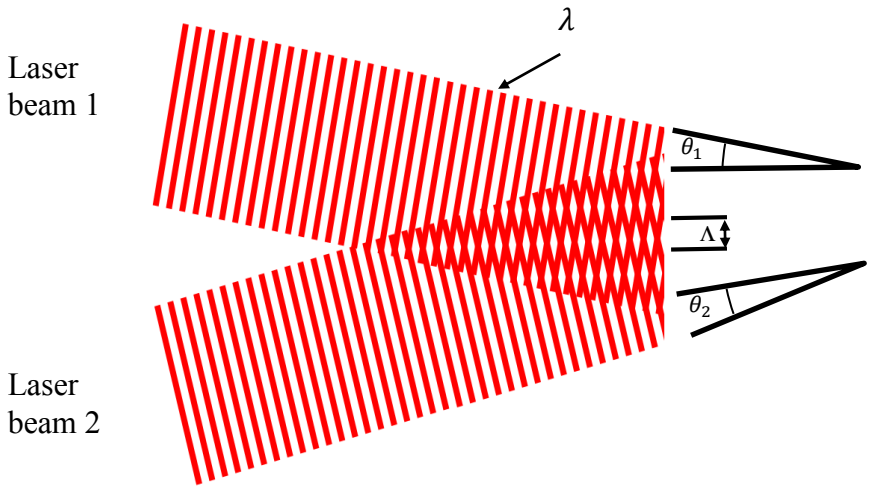

Figure 3.11 The diagram illustrates two coherent laser beam interference.

Many elements have to be taken into consideration for DLIP patterning, including laser choice, laser fluence and the number of laser pulses. The choice of laser type is dependent upon the application and the material used as the substrate. The fringe spacing is also directly proportional to the laser wavelength, the shorter the laser wavelength the smaller the fringe spacing. Laser wavelength is also very important in DLIP and must match the sensitivity and photon absorption of the substrate. For example, polyimide (PI) absorbs at a wavelength of 355nm, polystyrene (PS), and poly(ethylene terephthalate) (PET) at 266nm. Moreover, the refractive index (n) must also be taken into account for DLIP processing. A highly reflective substrate, such as metal and silicon, will cause secondary interference and form a standing wave in the vertical direction. If DLIP is applied to a photoresist layer, then the standing wave can cause a 'wave' effect on the sidewall of the resist to form a narrow waist and could weaken the resist. Bottom antireflective coatings (BARC) can be used to minimise standing waves caused by second interference (Carvalho *et al.*, 2006).

In the following example, different laser types, wavelengths, laser fluences and the number of pulses used for DLIP will be discussed. Yu *et al*. demonstrated DLIP line patterning on a PET substrate through laser interference using a Q-switched Nd:YAG laser, with 4 harmonic laser beams, at a wavelength of 266nm. They showed that the depth of the grooves are dependent upon laser fluence and the

number of pulses. Increasing the number of laser pulses from 1 to 10, linearly increased groove depth from ~0.5-3.5µm, respectively. However, the groove depth reached a plateau at a laser fluence of 0.2J/cm^{-2}. Further increases in laser fluence from 0.2 to 5.0 J/cm^{-2} did not increase groove depth (Yu *et al.*, 2005). In a similar study by Langheinrich *et al*. it was found that using a frequency tripled Nd:YAG laser (with wavelength of 355nm) DLIP PI substrates with periodic grooves ranging from 500nm to 10µm, could be generated using laser fluences from 0.2 to 1.0 J/cm^{-2}. They showed that lower fluence must be used to preserve the morphology of smaller spatial periods (Langheinrich *et al.*, 2012).

Some of the research carried out in this area has used polymers doped with different substances, such as dyes, to enhance photon absorption. For example, Broglia *et al*. showed that DLIP PS with 20µm periodic microgrooves could be generated using high-power single-pulsed Nd:YAG laser with a wavelength of 355nm. They showed that the PS weakly absorbed at this wavelength and no patterning was observed on plain PS through DLIP. To increase the PS absorption coefficient at this wavelength, PS film was doped with an azo dye, which has a high absorption coefficient between 300 and 450nm. Broglia *et al* observed that at a higher laser fluence (1125 J/cm^{-2}) more regular and uniform microgrooves were produced when compared to the microgrooves produced using a lower laser fluence (525 and 750 J/cm^{-2}). Also, the authors also found that when using a lower laser fluence, a 'swollen' region was produced, which was located at the maximum interference position (constructive interference). It is thought that this swollen region was generated by trapped gases from the decomposed azo group. At higher laser fluence the swollen region at the maximum interference position was found to have 'burst' forming holes on the doped PS surface. The authors suggest that there are two possible ablation mechanisms that could be involved for this patterning process: (i) The photons absorbed by the azo group may lead to a decomposition and release of nitrogen, which has assisted in ejecting solid material at supersonic velocity at the laser irradiated region; (ii) the heat absorbed by the azo group is transferred to the PS and leads to breakage of the polymer chain (Broglia *et al.*, 2014).

The advantages of the direct laser interference patterning method is that it can produce an array of sub-wavelength periodic patterns which is not limited by beam spot size (Stankevicius *et al.*, 2012). Besides that, this method also allows rapid patterning over a large area (patterning of areas over 1 cm^2 by a single exposure)(Wu *et al.*, 2005). However, the main disadvantage is that it can only generate a limited set of periodic patterns, such as interference grooves, circular holes, posts, and hexagonal or quadratic matrixes (Stay *et al.*, 2011).

3.6 Laser Induced Periodic Surface Structure

The phenomenon of laser-induced periodic surface structures (LIPSS) has attracted attention in the past few years. Nanoscale wavelike structures can be generated through linearly polarized ultra-short pulses on any material at fluences near the material's ablation threshold in a single pulse. The generated LIPSS can be either parallel, or orientated perpendicularly to the linearly polarized laser beam. Two distinct types of LPISS have been observed, an LIPSS with a periodicity approximately equal to the laser wavelength (λ) is termed a *low spatial frequency* LIPSS (LSFL), while a LIPSS with a periodicity smaller than the laser (λ) is termed a *high spatial frequency* LIPSS (HSFL).

A linearly polarized laser beam is irradiated on a strongly absorbing material such as metal, or semiconductors, generating a LSFL with periodicity (ΛLSFL) smaller or equal to the irradiated laser wavelength (λ) and oriented perpendicular to the polarized laser beam. The orientation of the LSFL formations are dependent on the material as well. When irradiated on dielectric material, the orientation of LSFL (wide band gap or called energy gap) can be either perpendicular or parallel to the polarized laser beam. The periodicity of the LSFL on dielectric materials is often equal to λ or λ/n, where n is the refractive index of the dielectric materials. The formation of the LSFL is explained by interference between the incident laser beam, the surface electromagnetic wave (SEW) generated by the scattering of laser radiation at the rough surface, and surface plasmon polaritons (SPP) (Bonse *et al.*, 2009)(Sipe *et al.*, 1983)(Garrelie *et al.*, 2011). The formation of HSFL is

predominantly observed on transparent materials with periodicity smaller than the laser irradiated wavelength and mostly perpendicular to the polarized laser beam. However, sometimes the HSFL also forms parallel to the polarized laser beam. The physical explanation of HSFL formation mechanisms are still under debate and it has been proposed that HSFL is generated by a second harmonic generation (Le Harzic *et al.*, 2011), self-organization (Costache *et al.*, 2002) or coulomb explosion (Dong and Molian, 2004).

The explanation of LIPSS formation is due to the fact that the nanoripple formation is strongly influenced by laser parameters including, laser fluence, number of laser pulses, and laser scanning speed. Yang *et al*. induced sub-wavelength, self-assembled periodicity in fused silica, by using a tightly focused linearly polarized femtosecond laser beam. They showed that the LIPSS periodicity could be decreased by increasing laser fluence. Moreover, the periodicity of the LIPSS was also found to be dependent on laser wavelength, with the shorter wavelength yielding smaller structures (Yang *et al.*, 2006). Höhm *et al*. induced LIPSS on silica using a femtosecond laser with different laser fluence and pulse numbers. The results showed that HSFL perpendicular to the polarized laser beam could be generated at a laser fluence of 5J/cm^2 (Figure 3.12a) and below this laser fluence no HSLF was observed. The transition of LIPSS morphology from HSFL to LSFL was observed at a laser fluence of ~6 J/cm^2 (Figures 3.12c and d). Below a laser fluence of 6 J/cm^2, HSFL was observed with periodicities of between 170 and 450nm. The LSFL was observed to increasingly dominate the area of the laser spot, with periods between of between 500 and 880nm by gradually increasing laser fluence (Figures 3.13e and f). Ultimately, only LSFL was observed at a laser fluence of 9.6 J/cm^2. Furthermore, the authors investigated the formation of LIPSS with a fixed laser fluence (5.4 J/cm^2) and varied pulse numbers. The authors observed that the transition of LIPSS morphology from HSFL to LSFL occurred when using laser pulses numbers of N=20. When increasing the laser pulses numbers to N=50, LSFL dominated and no HSFL was observed around the LSFL region. This phenomenon indicated that HSFL is only formed at a fluence close to the ablation threshold. No LIPSS was observed by further increasing the laser pulses numbers to N=100 (Höhm *et al.*, 2012).

The advantage of this method is that it allows the generation of a sub-wavelength nano ripple-like periodical structure within the laser spot with single or multiple exposures. Although this method allows the generation of periodic surface structures, the main disadvantage is that it is only capable of generating ripple-like structures.

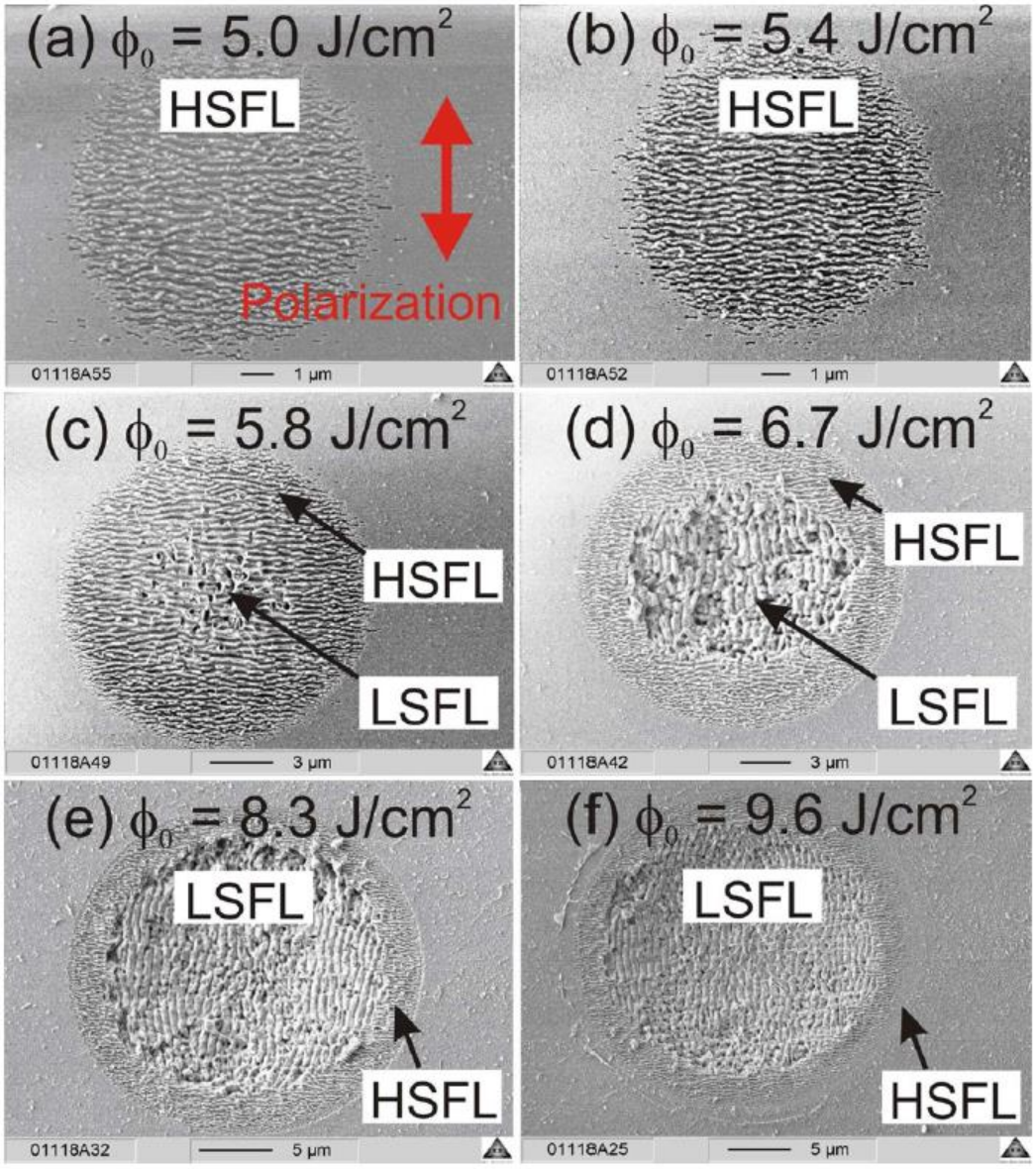

Figure 3.12 SEM images of the single-crystalline synthetic quartz surface irradiated with linearly polarized single laser pulses (λ=800 nm, τ=150 fs) with 10 laser pulses and (a-f) different laser fluence between 5.0 J/cm^2 and 9.6 J/cm^2 (reproduced with permission of Höhm *et al.*, 2012).

3.7 Two-Photon Polymerization Technique

For most of the conventional methods 2D and 3D pattern resolution is limited by the optical diffraction limit and requires expensive photomasking, or deep ultraviolet light (DUV) systems for nanofabrication. Two photon polymerization (TPP) techniques offer many advantages for tissue engineering applications, as this method can produce submicron scale complex three dimension architectures in photosensitive liquid materials. TPP is based on simultaneous absorption of two photons to induce the chemical reaction between the photoinitiator and monomer for polymer propagation in the transparent material. The TPP system setup is shown in Figure 3.13

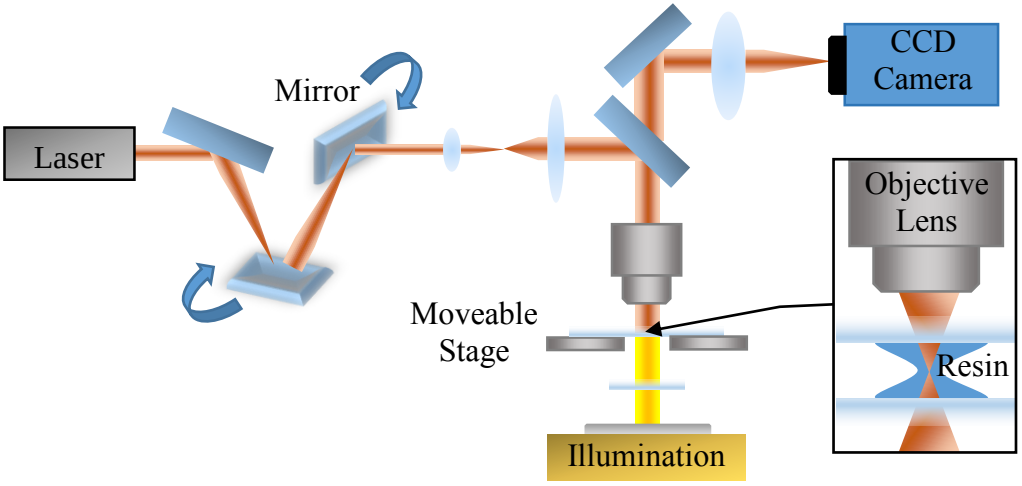

Figure 3.13 Two photon polymerization system using a laser scanning system, x-y-z computer-controlled translational stage and a CCD camera for real-time image process monitoring. The resin is sandwiched between two glass coverslips and a high numerical (NA) objective lens is used to focus the laser into the volume of the resin.

The initiation of simultaneous absorption of two-photons requires high peak laser intensity. This is because once the first photon is absorbed by the absorbing species, a virtual state is created, which has a relatively short lifetime (10^{-15} s). Therefore the second photon must be absorbed in this period, so as to reaches the higher energy electronic state before it decays. Hence, Ti: sapphire lasers are the most widely used laser system, because they produce an ultrahigh peak power with a very short pulse width of approximately 100 femtoseconds (fs), which fulfils the mechanism of simultaneous absorption of two-photons. Besides this, the Ti: sapphire laser has advantages in TPP, in that its near infrared 800nm wavelength

is transparent to photosensitive resins and can be closely focused into the volume of the resin to induce polymer polymerization. The polymer polymerization mechanism induced by TPP involves three steps: (i) initiation, (ii) propagation, and (iii) termination. When the laser beam is focused into the liquid-state resin, the photosensitizer chromophore becomes excited, through simultaneous absorption of the two photons and emits fluorescent light in the UV-vis regime. The emitted fluorescent light is then absorbed by the photoinitiator which generates radicals (initiation). The radicals then react with the monomer (or oligomer) thus producing a radical monomer. The monomer radicals then expand in a chain reaction (propagation) until two radical monomers meet (termination) (Lee *et al.*, 2006).

The TPP can be arbitrarily patterned in the volume medium because only the laser focus region with a high photon density can trigger simultaneous absorption of two photons and initiate polymer polymerization (Wu *et al.*, 2006). Hence, the rate of two photon absorption is proportional to the square of the field intensity (Obata *et al.*, 2013). Arbitrary three dimensional patterning in the volume of the resin can be achieved by using piezo-electric computer controlled stages, or optical scanning systems, which either move the resin relative to a static laser focus, or move the focused laser in the volume of the resin. Unlike conventional UV stereolithography, the polymer polymerization process is induced through single photon absorption and the photosensitive materials are highly absorptive in the UV region. Therefore, photon absorption is at the surface of the resin and can only fabricate 3D structures layer by layer, with the assist of a Z-translational stage. Once the layer is solidified the Z-translational stage is moved down by submerging the solidified layer into the liquid polymer to continue the next new layer on top of the previous layer. Typically the process is around several 100µm/s and the working area has dimensions of 15 x 10 cm^2 (Wong and Hernandez, 2012).

TPP can achieve minimum lateral resolutions by using a high numerical aperture (NA) lens and low aspect ratio processing parameters, such as low laser power and low exposure time. There are a wide variety of photosensitive materials that can be processed by TPP, including, zirconium sol-gel, acrylate-based polymers, titanium-containing hybrid materials and organically-modified ceramic materials. For example, Claeyssens *et al*. produced a three dimensional wafer structure 50µm

in height and with an array of ~10x10µm square holes within the structure. The wafer structure was fabricated layer by layer, using a biodegradable polycaprolactone-based triblock copolymer through TPP, with a minimum laser power of 30mW to initiate a 4,4′-bis(diethylamino)benzophenone photoinitiator (Claeyssens *et al.*, 2009). However, the softness of this photosensitive material caused distortion of the square structures due to polymer shrinkage during polymerization (Figure 3.14a).

In another study by Ovsianikov *et al.*, it was shown that three-dimensional high resolution woodpile structures could be created through TPP by using an ultra-low shrinking zirconium sol-gel hybrid photo-sensitive material and laser powers ranging between 8-12mW, and a constant scanning speed of 200µm/s (Figure 3.14b) (Ovsianikov *et al.*, 2008).

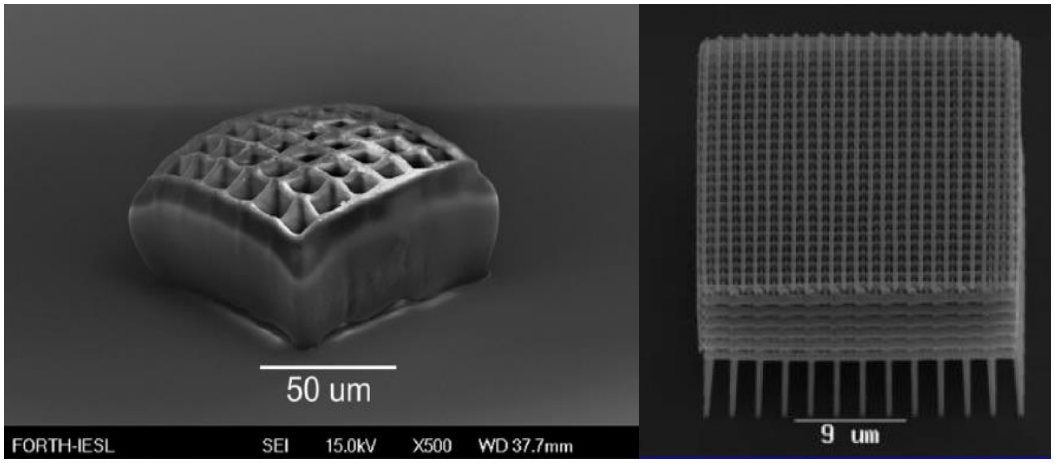

Figure 3.14 SEM image showing the structure of (a) square box which has undergone polymer shrinkage (Claeyssens et al., 2009) and (b) a three dimensional woodpile structure produced by TPP (reproduced with permission of Ovsianikov et al., 2008).

Other studies have demonstrated, using different photosensitive materials and processing parameters, that it is possible to produce 3D microstructures including a Venus sculpture (Serbin *et al.*, 2003), microneedles (Gittard *et al.*, 2009) and micropumps (Maruo and Inoue, 2006).

Although TPP methods allow the arbitrary patterning of sub-wavelength features, TPP is a time consuming production process which is not suitable for large implant

fabrication and only a limited number of materials can be used for this fabrication process. Currently TPP is still under development, and one approach taken by many researchers is to introduce micro-array lenses into the TPP system to generate multiple beam spots to overcome the slow production process (Formanek *et al.*, 2006).

All the technology discussed above have their own advantages and disadvantages in surface patterning. There is no single system or technique that can fulfil all of the application requirements in this field of surface modification. Hence, it is important to consider which surface topography scales are more effective to influence cells. In this thesis, direct laser patterning techniques were used to produce feature with sizes ranging from ~4 to 6µm, which is smaller than the laser beam spot size (~25-30µm), using an overlapping technique. This laser machining procedure involved the processing spot of the laser beam being partially overlaid on top of the previous laser spot's interaction with the surface of the substrate. This technique formed a micro laser pattern on the metal surface. The next chapter will discuss the effect of surface topography on cell behaviour and the impact of surface topography on stent applications.

Chapter 4

4.0 The Effects of Micro and Nano topographies on Cell Behaviour and Their Impact on Stent Technology

4.1 The Effect of Surface Topography on Cell Behaviour

The effect of surface topography on cell morphology and behaviours was identified, as early as 1911, by Ross Granville Harrison (Harrison, 1911). He found that embryonic frog spinal neurons only extended along the web filaments when cultured on a meshwork of spider web (Figure 4.1a) (Harrison, 1914). Later in 1945, Paul Weiss observed similar behaviour, when he cultured embryonic chicken spinal neurons on grooved surfaces, which were generated by brushing blood clots onto a glass coverslip. He described the phenomenon as contact guidance (Figure 4.1b)(Weiss, 1945).

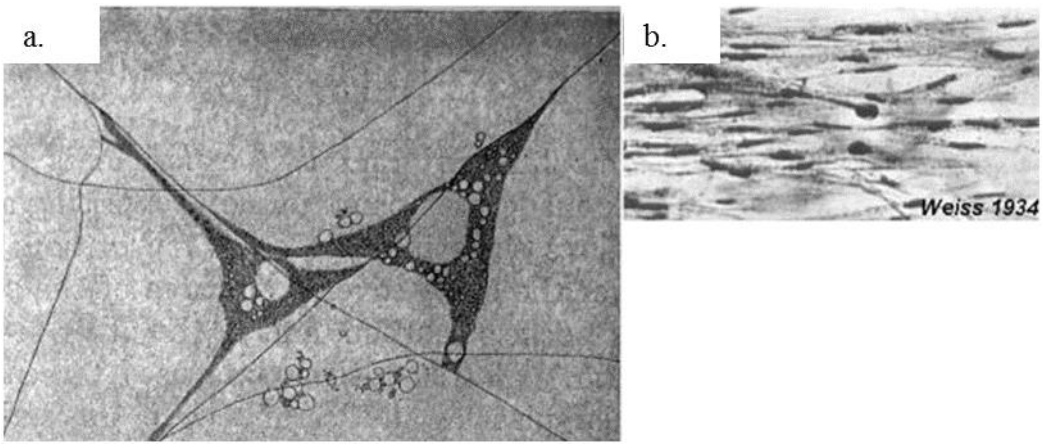

Figure 4.1 (a) Ross Granville Harrison cultured embryonic frog spinal neurons cells on spider web (reproduced with permission of Harrison, 1914). (b) Paul Weiss cultured embryonic chicken spinal neurons on a surface with grooves generated by brushing blood clotting onto the glass coverslip (reproduced with permission of Weiss, 1934).

In a similar study, Curtis and Varde cultured chick-heart fibroblast cells (fragmented from 9-day embryos) on different types of substrates including glass, silica coated polystyrene replicas of diffraction gratings (with groove and ridge features), and silica fibers (8 to 40µm). They observed that cell morphology and behaviour was not only affected by substrate topography, but also by cell density (Curtis and Varde, 1964). However, the lack of micro and nano-fabrication technology at that time restricted the insight and understanding of cell surface interactions.

It was therefore not until the 1990's, which saw the rapid development of semi-conductor manufacturing techniques, that researchers were able to generate surfaces having a well-defined micro-topography and thus had the ability to study the effects of surface topography on cell behaviour. Clark *et al*. investigated the effect of patterned substrates on baby hamster kidney (BHK) cell behaviour. Using substrates having different step heights (1-18µm), generated using photolithography, Clark observed that the cells aligned at the edge of the step, with increased cell alignment at the higher steps (10 and 18µm) (Figure 4.2). They also found that the frequency of the cells crossing over the 1µm step height, was not significantly different compared to the control, but the crossing over frequency was found to be decreased for the 3µm step height and higher (Clark *et al.*, 1987).

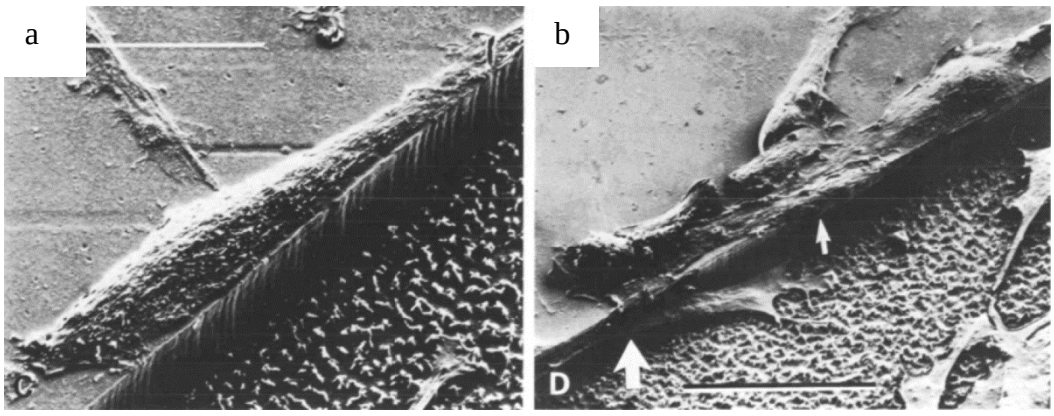

Figure 4.2 SEM images of BHK cultured on 10µm height steps. (a) The cells aligned on the upper surface of the step. (b) Cells aligned on lower surface of the step (reproduced with permission of Clark *et al.*, 1987).

Following this work, Clark *et al*. generated grooved substrates with varying dimensions (4-24µm pitch (grooves + ridges), 0.2-2µm depth) to examine their effect microgrooves. The study showed that substrates with a 6µm pitch and 2µm depth had more effect on cell alignment than substrates with a 12µm pitch and the same depth. The authors also examined the effect of depth on BHK cell alignment and found no cells aligned on substrates with a 6µm pitch and 0.3µm depth. In contrast, cells aligned on substrates with the 6µm pitch and 2µm depth (Figure 4.3). The result suggested that BHK cell alignment increases with increasing groove depth, but decreases with increasing pitch. (Clark *et al.*, 1990).

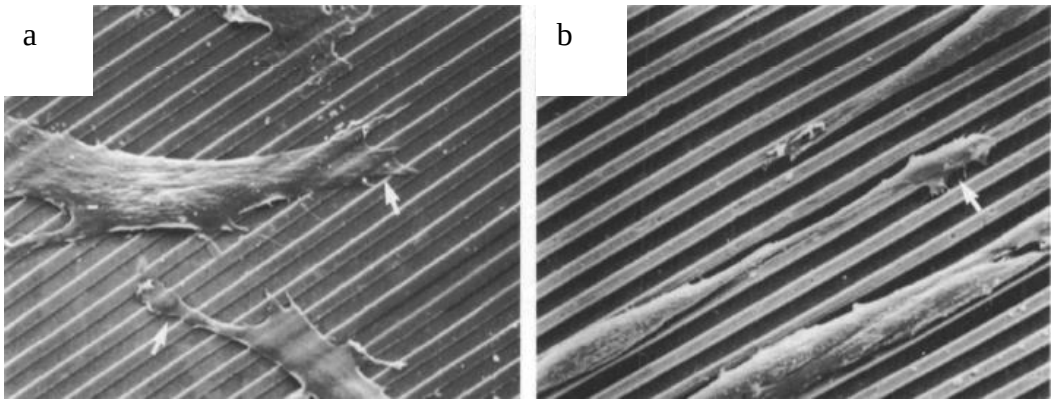

Figure 4.3 SEM image of BHK cells on grooved substrates. (a) 6µm pitch, 0.3µm deep grooves, (b) 6µm pitch, 2µm deep groove (reproduced with permission of Clark *et al.*, 1990).

Currently, more advanced MEMS and other micro-nanofabrication technology (discussed previously), has enabled scientists to produce a variety of surface topographies that can be used to manipulate cell behaviour for specific applications. For example, experiments have been conducted by researchers using different mammalian cell types including epithelial, endothelial, fibroblast, nerve and muscle cells, in order to study the cell's response to a variety of different topographies. The most commonly studied topography has been the micro-nano groove. The work of Clark et al. has proven that the depth dimension has a profound influence on cell migration, orientation, cytoskeleton arrangement, and focal adhesion establishment, especially on the narrowest and deepest grooves. Other micro-nano surface topographies (such as pillars, pits and holes) have also been shown to affect cell behaviour (Pan *et al.*, 2012)(Seo *et al.*, 2014)(Charnley

et al., 2009). For example, in a study skeletal stem cells were cultured on nanopits with a controlled disorder of ±50nm (NSQ50), and it was demonstrated that the skeletal stem cells expressed particularly high levels of bone cell markers. The result was comparable to the skeletal stem cells cultured on a planar substrate in medium supplemented with dexamethasone and ascorbic acid, a chemical enhancer of skeletal stem cell differentiation down the oestrogenic lineage (Dalby *et al.*, 2007).

In vivo, Schwann cells (SCs) are important in eliminating cellular debris, directing neuron growth and myelinating axons. During axon regeneration, SCs rapidly proliferate to form longitudinal cell strands, termed as bands of Büngner, which guide axonal regrowth in a specific direction in order to reach the target for motion or sensation (Bhatheja and Field, 2006) (Ribeiro-Resende *et al.*, 2009)(Bunge, 1993). Miller *et al*. examined SC growth on biodegradable Polylactic acid (PDLA) microgrooved surfaces with varied width, spacing and depth. They found that microgrooves with a width of between 5-10µm and spacing between 10-20µm are optimal for SC alignment. Microgrooves with a width smaller or larger than the SCs, did not promote SC alignment. Groove depths of between 1.4 and 3.3µm and with constant width of 10µm, were observed to promote cell alignment along the grooves. Furthermore, Miller *et al*., showed that the initial cell seeding density also affects SC alignment. Lower SC seeding densities result in a lower alignment rate, which they suggested was due to the probability of less cell-to-cell communication (Miller *et al.*, 2001).

Other studies have also shown that micro-patterned substrates can affect the behaviour of neuronal cells. For example, Sørensen *et al.*, examined spinal cord neuron alignment on a monolayer of astrocytes, which had been cultured on top of a microgrooved surface. They found that microgrooves with a width of 5µm, 12.5µm and 25µm respectively, significantly enhanced spinal cord neuron alignment, when compared to 100µm wide microgrooves. However, the authors suggest that only microgrooves with widths of 12.5µm and 25µm, were found to be optimal for long term (>3weeks) neurite alignment support (Sipe *et al.*, 1983). In a similar study, Yao *et al.*, examined pheochromocytoma (PC12) neurite outgrowth on functionalised micro-patterned poly (lactide-co-glycolide) (PLGA),

coated with laminin peptide and type I Collagen. They observed that at the early stage of PC12 neurite outgrowth, 5µm microgrooves have a more profound effect on neurite elongation and alignment, compared to 10µm wide microgrooves. They also found that microgrooves coated with laminin peptide encouraged a more parallel neurite growth, compared to type I collagen. Their results indicated that microgrooves having widths of 5µm and conjugated with laminin peptide, could enhance guidance of PC12 neurite growth (Yao *et al.*, 2009).

Likewise, Su *et al* examined the effect of growing PC12 cells on parallel nano-grooves, having widths of 100nm and 800nm, and a depth of 1200nm. The effect of growing PC12 cells on nano-pillars was also investigated. These pillars had a diameter of 461nm, spacing of 339nm and a height of 1200nm. The results showed that PC12 cells extended in a bipolar phenotype, with more than 90% of the cells being found to be aligned parallel (within 10^{o}) along nano-grooves. However, the authors also found that the nano-grooved patterns reduced PC12 cell migration velocity. They also showed that the nano-pillars increased the mean number of neurites per cell, but that all PC12 cells were randomly oriented and exhibited a shorter average neurite length, compared to PC12 cells grown on nano-grooves. Overall, the results indicate that both nano-groove and nano-pillars are not suitable for neurite growth, due to the slowing down of PC12 migration and short neurite length, respectively (Su *et al.*, 2013). Other experiments have showed that azobenzene copolymer (Poly(methylmethacrylate)-co-(Disperse Red 1 acrylate) with grooves having a 1µm period with 250nm depth, can improve human astrocyte adhesion and promote strong alignment (Baac *et al.*, 2004). In contrast, rat astrocytes on polystyrene with 10µm grooves/ridges, and 3µm in depth, showed less adhesion and strong alignment (Recknor *et al.*, 2004).

Other cells have also been investigated. For example, rat bone marrow osteoblast-like (RBM) cell attachment and growth behaviour has been studied on microgrooved polystyrene substrates, having a groove depth of between 0.5–1.5µm and a groove ridge width of between 1–10µm. In this work it was demonstrated that osteoblast-like RBM cell growth followed the geometry of the microgrooves, but only when groove width was larger than 5µm. The focal adhesion points for the RBM cells were found to form all over the microgrooves.

Whereas, the focal adhesions of osteoblast-like RBM cells grown on microgrooved substrates, having a groove width smaller than 2µm, were predominantly located at edge of the ridge, without contact with the grooves (Matsuzaka *et al.*, 1999). In this study it was also observed that the focal adhesions were found formed all over the microgrooves. In contrast, focal adhesion formation on microgrooves with a width smaller than 2µm were predominantly located on the edge of the ridge and not on the grooves (Matsuzaka *et al.*, 2003).

In a study by Braber *et al.*, similar behaviours were observed using rat dermal fibroblast cells (RDFs) grown on microgrooves. In this study it was found that, only grooves having a width greater than 5µm allowed RDFs cells to descend onto the bottom of the grooves and establish focal adhesion points (FAP). When the groove width was less than 5µm the FAPs were predominantly established at the edge of the ridges. It is thought that this was due to accessibility restrictions of the cells to the bottom on the grooves (den Braber, Jansen, *et al.*, 1998). Other experiments have shown that the highest cell densities were not found on the deepest (5.4µm) and narrowest (1µm) grooves, even though the surface area was large. It was suggested that the RDF cells did not descend onto the bottom of the grooves and thus were not able to establish contact guidance. Therefore, RDFs cells were found to bridge the deepest and narrowest grooves, whereas the cells on wide and shallow microgrooves followed the geometry (Walboomers *et al.*, 1999).

In another study Mak *et al.*, examined the effects of growing human hepatoma (BEL-7402) cells on PDMS microgrooves (10µm, 30µm, and 50µm in width, and 2µm in depth) and nanoporous PDMS substrates (140nm in diameter). The results showed that BEL-7402 cells aligned along the microgrooves and that there was no significant difference in the mean cell migration velocity, compared to when cells were grown on the flat PDMS. However, BEL-7402 cell migration velocity was found to be higher on nanoporous PDMS, but no specific cell alignment was observed. The authors of this study suggest that nanoporous PDMS may have increased cell migration velocity because the surface allowed sufficient levels of cell adhesion (Mak *et al.*, 2013).

Biela *et al* examined the response sensitivity of different vascular cell types, including fibroblast cells, endothelial and smooth muscle cells, to microgrooves

with a lateral dimension of 2-10µm and depths ranging from 50-200nm. Their results demonstrated that all three cell types aligned along those microgrooves having a 2µm width and 200nm depth. In contrast, less cell alignment was observed on grooves having a 10µm width, but of the same depth. All three cell types growing on narrower and deeper microgrooves have shown increased order parameters of cell polarity (S=0 if cells are randomly orientated, S=1 if cells are aligned parallel with the grooves, and S=-1 if cells are aligned perpendicular to the grooves) and elongation (E=1 if the cell is perfectly circular, and E=0 if cell has a thin elongated shape). The author compared the ordered parameter between three cell types and showed that FCs were more sensitive than ECs and SMCs, as FCs had a higher order parameter in cell polarity on 2µm microgrooves with 100nm depth (S=0.85 compared to ECs S=0.35) and SMCs (S=0.4). Moreover, the FCs also had a higher order parameter with respect to cell elongation in all microgrooves, except microgrooves with 50nm depth (Biela *et al.*, 2009).

All the previously described experiments have shown that different types of patterned surface, particularly microgrooves, can affect aspects of cell behaviour and this can be cell specific. Although different cell types have different response sensitivities. However, narrower (<5µm) and deeper (>2µm) surface topographies seem to have a strong effect on focal adhesion, actin filament organisation, cell migration and cell alignment. Many more experiments have been carried out in this area. These are outlined in the appendices (Table A1.2).

4.2 Coronary Heart Disease and the Development of Stent Technology

Coronary heart disease (CHD) is the leading cause of mortality in the UK with approximately 2.3 million people affected with CHD in the UK alone. CHD accounts for approximately 72,000 deaths per year, with an average mortality rate

of 200 deaths per day. This is economically expensive, costing the UK billions of pounds in healthcare costs for CHD treatments each year (Townsend *et al.*, 2012).

The major risk factor of CHD is atherosclerosis, which results from fatty substances, such as cholesterol, being progressively deposited within the arterial vessel wall, resulting in the formation of atheroma plaques. This build-up of plaque leads to a narrowing of the arterial lumen. As a consequence, there is impaired blood flow through the artery and this impedes nutrient and oxygen supply to the myocardium. The reduction in the oxygen supply to the heart may cause angina and if the blockage remains untreated, it can lead to more serious conditions including a heart attack, heart failure, or even death (Nayler, 1995). Atherosclerosis affects all ages and genders and is not geographically selective. It is usually caused by poor personal lifestyle habits such as smoking, poor diet, lack of exercise and excessive alcohol consumption. Such conditions can lead to stress, high blood cholesterol, high blood pressure and diabetes, respectively (Vogel, 1997)(de Waure *et al.*, 2013). The current therapeutic approaches, to restoring blood flow, are through the implantation of percutaneous devices and via coronary artery bypass graft surgery.

Coronary artery bypass graft (CABG) surgery was first introduced by a team led by Dr. Robert Goetz in 1960 in the US, at the Albert Einstein College of Medicine, Bronx Municipal Hospital Centre. During this procedure, healthy blood vessel segments are obtained from the patient's body, e.g. saphenous vein from the legs, the radial artery from the arms or the internal artery from the chest (Dee, 2013). The grafted blood vessel is then used to bypass around the blocked portion of the coronary artery and restores blood and oxygen supply to the myocardium. The major disadvantages of CABG are that it requires invasive surgery and a relatively long associated recovery period, typically 4 to 7 days in hospital with up to 3 months to fully recover (Michaels, 2002). Moreover, more than 30% of the patients have poor quality or inadequate veins due to previous surgery (Laflamme *et al.*, 2005).

A decade later, balloon angioplasty was pioneered by Gruentzig in 1977 (King, 1996). This technique involved passing a deflated balloon using a thin, flexible catheter, into the artery through the groin, or arm, to an affected coronary artery.

This is then followed by balloon inflation to widen the narrowed artery, by compressing the plaque against the vessel wall to restore blood flow. The majority of patients develop restenosis and lose up to 50% of the lumen area, which requires revascularisation within 6 months. This is due to neointimal hyperplasia and vessel remodelling, or immediate elastic recoil of the overstretched vessel wall. The chance of restenosis for balloon angioplasty is 40% (Michaels, 2002).

Later, in 1977 Sigwart introduced the coronary stent, or metallic mesh tubes, to serve as a medical device to prevent possibility of elastic recoil and vessel remodelling after angioplasty, or percutaneous coronary intervention (PCI). The details of this procedure is illustrated in Figure 4.4 below. The introduction of the stent has resolved vascular remodelling and reduced the restenosis rate to between 15 to 20% (Teirstein *et al.*, 1994). However, experimental studies in animals (Hanke *et al.*, 1995) and humans (Teirstein *et al.*, 1994) have shown that expanding the stent strut during PCI results in deep vascular trauma and induced abundant intimal hyperplasia.

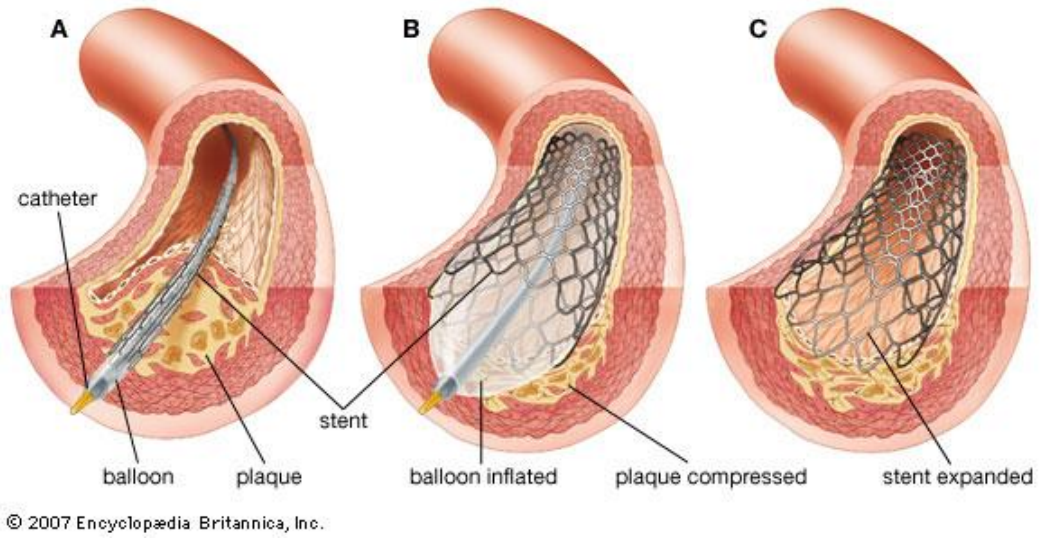

Figure 4.4 The diagram illustrates the balloon angioplasty procedure. (a) A thin, flexible catheter with deflated balloon and stent is inserted into the artery. (b) The balloon is inflated causing the stent to expand against the artery wall and compressing the plaque. (c) The expanded stent remains permanently in the artery for mechanical support (reproduced with permission of Angioplasty, 2014)

Endothelial and smooth muscle cells have major influences in artery restenosis. The coronary artery consists of three different layers, known as the tunica adventitia, media, and intima. Each layer consists of different types of cells and ECM: (1) Tunica adventitia is the outer layer that covers the entire artery and consists of connective tissue, collagen, and fibroblast cells (2) Tunica medial is the middle layer of the artery and consists of smooth muscle cells. (3) The innermost layer is the tunica intima and this has direct contact with circulating blood and consists of endothelial cells that form the lumen (Kim *et al.*, 2013).

Endothelial cell denudation is caused by stent expansion during the PCI procedure, triggering a "wound healing program". The wound healing response initiates platelet attachment, aggregation, release of platelet derived growth factors (PDGF) and other mitogenic factors at the site of injury. The increase in stimulatory growth factors and cytokines (PDGF, interleukin-1, interleukin-6, and tumour necrosis factor-α) and reduced endothelium-derived inhibitory factors (nitric oxide, heparin sulfate proteoglycan), leads to the activation of medial layer quiescent SMCs causing migration and proliferation into the intimal layer, eventually re-narrowing the artery lumen through neointimal hyperplasia (Garg and Hassid, 1989) (Marx *et al.*, 2011).

4.2.1 Drug Eluting Stents and Their Complications

Currently, drug eluting stents (DES) have been used to minimise the risk of restenosis and initially proved superior compared to BMS. Numerous commercial DES have been approved by the FDA (the Food and Drugs Administration), for instance, Cypher (sirolimus-eluting stent; Cordis Corporation, Johnson & Johnson, Warren, NJ), Taxus, Endeavour, and Xience V. These anti-proliferative pharmaceutical agents are blended with a polymer and coated on DES to inhibit smooth muscle cell proliferation/migration in the coronary artery, after stent placement. DESs have minimized the rate of restenosis to between 50-70% compared to BMS (Windecker and Meier, 2007). However, the current major concern of DES are late (1month - 1year) and very late stent thrombosis (ST) (>1 year) following DES placement. This is due to a delayed stent strut endothelization,

caused by the anti-proliferative drugs used on DES. Late stent thrombosis is a catastrophic complication which can lead to myocardial infarction, or sudden cardiac death. Although the latest generation of DES have thinner metallic platforms, biodegradable polymers and precise drug release profiles in order to minimize the risk of restenosis. However a risk still exists with DES (Garg and Serruys, 2010).

4.2.2 The Impact of Surface Topography on Clinical Stent Applications

Surface topography has been well studied and might be the alternative solution to physically manipulate EC and SMC behavior on the stent surface, in order to minimize restenosis and late stent thrombosis without using pharmaceutical drugs. Currently, most of the studies have been carried out *in vitro*, to examine the response of ECs and SMCs, in an attempt to enhance the cellular function using micro-nanofabricated surfaces. For instance, Lu *et al.*, attempted to improve rat aortic endothelial cell (RAECs) adhesion using micro/nano-grooved substrates, with the grooves having a width ranging from 750nm to 100μm. The results showed that the narrowest groove (750nm) had the highest cell adhesion and proliferation density, compared to the larger sized microgrooves and a smooth surface (i.e. no grooves). Cell adhesion and proliferation density were significantly increased as the microgroove decreased in lateral dimension (Lu *et al.*, 2008).

A number of research groups have imitated the physiological conditions in the coronary artery, by exposing shear stress on vascular cells in order to investigate the effectiveness of the surface topography. For example, Uttayarat *et al.*, examined BAEC migration on parallel and orthogonal microgrooves (having a lateral dimension of 2-5μm and a depth of 1μm) under shear stress. The results showed that BAECs were aligned to and migrated along the parallel and orthogonal microgrooves under static conditions. Furthermore, the actin filaments were aligned along the grooves and the focal adhesions of the cell were distributed on the edge of the ridge, the exception being on the widest microgrooves, where

FAs were found distributed on the ridge and channel walls. No significant effect on BAEC alignment was observed when the cells were exposed to a moderate shear stress (13.5dyn/cm^2), even on the orthogonal microgrooves. In contrast, when exposed to a higher shear stress (58dyn/cm^2), the cells were observed to migrate orthogonal to the microgroove and followed the direction of the flow. However, the authors observed that the actin filaments and FA still remained aligned parallel to the microgrooves. This suggested that the surface topography was more effective in guiding cell migration than mechanical shear stress (Uttayarat *et al.*, 2005).

Sprague *et al*. demonstrated the impact of 15µm parallel micro-engineered grooves on a stent surface with respect to endothelial cell migration, proliferation, and function, both *in vitro* and *in vivo* (Figure 4.5). In their study, two identical stainless steel stents, with and without luminal microgrooves, were used in the investigation. The *in vitro* results showed that the endothelial cells, at 7 days post cell-seeding, migrated up to two fold further on the grooved stent. The endothelial cell proliferation rate and nitric oxide production was also found to be increased while the apoptosis rate was decreased. The *in vivo* results were obtained using a porcine coronary injury model and, at 3 days post-stent deployment, it was found that the endothelial coverage was significantly increased in the grooved stent compared to the non-grooved stent (81.3% versus 67.5%, P=0.0002). After 28 days of stent deployment, the grooved stent showed lower neointimal thickness compared with a non-grooved stent (21.1%, P=0.011) and a MLVS stent (40.8%, P=0.014) (Sprague *et al.*, 2012).

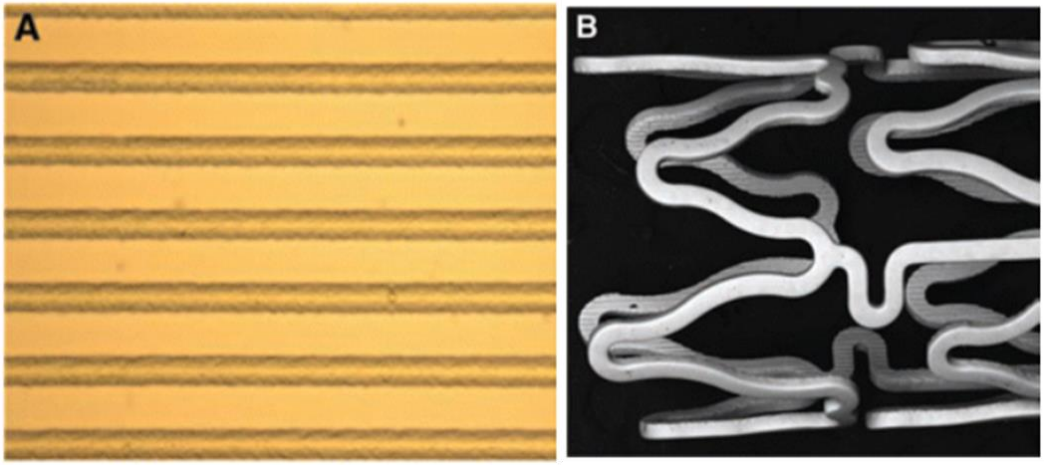

Figure 4.5 (a) Photomicrograph of 15µm microgrooved surface and (b) SEM

image of stainless steel stent with a luminal 15µm microgrooved surface (reproduced with permission of Sprague *et al.*, 2012).

Dibra *et al.*, performed a randomized double-blind controlled trial to study the effect of stent surface topography on the outcome of patients undergoing coronary stenting. The 316 L stainless steel slotted-tube coronary stents were laser machined. This was then followed by electro-polishing some of the stents to produce a smooth surfaced stent (Figure 4.6a) while other stents were sand blasted to produce a rough surfaced stent, with a surface roughness (RMS) of 0.09 and 0.21 µm, respectively (figure 4.6b). A total of 200 patients with stenosis were randomly assigned in the double-blind study and received either a rough stent or a smooth stent. The authors reported that those patients who received a rough surface stent had a mean lower late lumen loss of 1.0±0.7mm and also a mean lower angiographic restenosis rate of 25%. In contrast, those that received a smooth surfaced stent were found to have a mean late lumen loss of 1.2±0.7mm and a mean angiographic restenosis rate of 35%. Overall these results show that the rough surface performed better than the smooth surfaced stent (Dibra *et al.*, 2005).

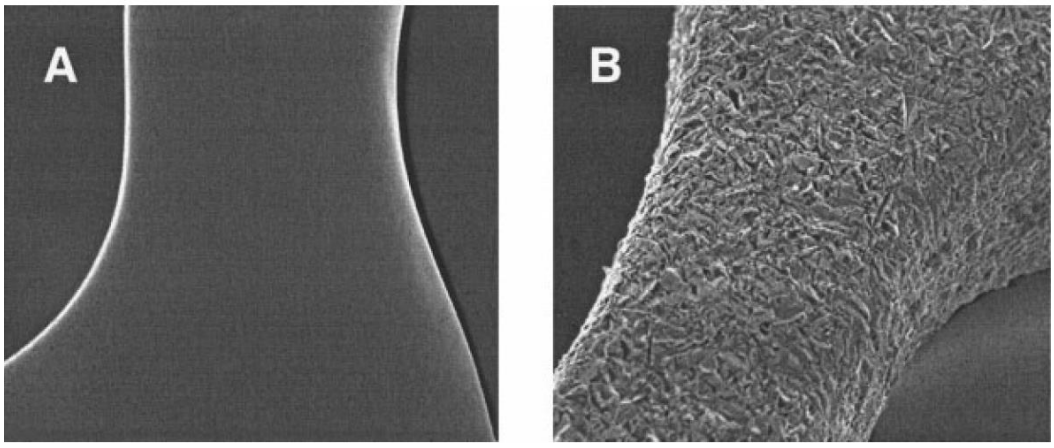

Figure 4.6 showed the SEM image of (a) smooth surface stent produced by electro-polishing and (b) rough surface stent produced by sand blasting (reproduced with permission of Dibra *et al.*, 2005).

Vascular smooth muscle cells play an important role in vascular remodeling under pathological conditions. The progression of converting SMC morphology from a quiescent phenotype to proliferative phenotype leads to atherosclerosis and

restenosis (Marx *et al.*, 2011). Some researchers have showed that manipulation of the SMC shape alone could regulate DNA synthesis and suppress SMC proliferation. Thakar *et al*. examined DNA synthesis of human aortic smooth muscle cells (HASMCs), by manipulating their morphology by growing them on microgrooves having a 10µm width and 2.8µm depth. They demonstrated that HASMCs grown on microgrooves exhibited an elongated morphology, lower cell proliferation rate, less spreading, and a lower cell and nucleus shape index (cell and nucleus shape index values were between one (a circular shape) and zero (an elongated, linear morphology)). The most interesting result was that there was a lower expression of neuron derived orphan receptor-1 (NOR-1) in the elongated HASMCs and that knocking down NOR-1 leads to DNA synthesis suppression. These results indicate that regulation of HASMC DNA synthesis could be achieved by micro-patterning and confining the cells to a small area (Thakar *et al.*, 2003) (Thakar *et al.*, 2009).

Although there has been a limited amount of research done to study the effects of nano- and micro-patterning on vascular cells, the work has demonstrated that vascular cell behaviour is influenced by the pattern dimensions. Microgroove and ridge features between 2-5µm have a profound effect upon BAEC focal adhesion formation, actin alignment and cell migration under static and flow conditions. HASMCs grown on microgrooves with a dimension of 10µm width and 2.8µm depth, exhibited an elongated morphology, lower cell proliferation rate, less spreading, and a lower cell and nucleus shape index. Even a random rough surface topography (RMS=0.21µm) have shown lower late lumen loss.

This thesis aims to develop a novel micro-topography which could physically enhance stent performance by accelerating vascular endothelial cell adhesion and proliferation, whilst suppressing vascular smooth muscle cell proliferation. This is desirable for minimizing nominal hyperplasia after stent placement. Laser beam overlapping technique are described that are capable of generating microfringe and ripple structures, ranging from ~4-6µm in width. In this study, a novel durable biocompatible Z1A1 polyurethane with ultimate tensile strength (39.6MPa) which is suitable for stent coating, was used to replicate the micro-textured from laser micro-textured stainless steel mould. The benefit of direct laser patterning and

laser overlapping techniques offers lower production, operating, and set-up costs (the SPI solid state laser system costs less than £10,000).

Chapter 5

5.0 Experimental Design

The data presented in thesis were obtained from a range of experiments that were designed and performed in an attempt to ultimately enhance endothelial cell adhesion and proliferation. This was achieved by designing laser micro-textured polymer surfaces that would promote endothelial cell adhesion (over a relatively short time period, i.e. 2 hours) and proliferation. This work will find applications in biomedical implant technology, particularly in stent development, where rapid colonisation of the stents with endothelial cells has the potential to minimise the risk of restenosis.

The polymer used in this work was polyurethane (Z1A1) and was provided by Biomer Technology Ltd. The exact details of this novel polymer's chemistry are not provided due to commercial sensitivity. The principal equipment used in these experiments was an SPI 20W 1064nm infrared fiber laser, which allows the direct microfabrication of polished stainless steel. Once processed, the stainless steel can be used as a master template for surface replication through polyurethane casting.

The replicated or cast-off polyurethanes having a novel micro-topography, were characterized using the Wyko NT1100 optical profiling system. A FLUOstar OPTIMA fluorescent microplate reader, SpectraMax 250 microplate reader and confocal laser scanning microscope (CLSM), were the main pieces of equipment used to study the behaviour of the cells on the micro-textured polyurethanes. Experiments were carried out under physiological conditions and were repeated under static conditions (no flow) and also when subjected to shear stresses generated by a flow of its culture medium over the cells, so as to mimic the physical arterial environment.

Two different cell types were used throughout the work described in this thesis namely, bovine aorta endothelium cells (BAE-1) and primary human coronary

artery smooth muscle cells (HCASMCs). BAE-1 cells are an economical alternative to the primary endothelial cell which have been used extensively to study endothelial cell behaviour. These cells are described in more detail in Section 6.3.4.

The general aims of the work presented in this thesis were:

1. To use laser technology to develop polyurethane substrates having novel surface micro-topographies.
2. To investigate the effects of these novel micro-topographies on BAE-1 and HCASMC cell adhesion, proliferation and migration under physiologically static conditions.
3. To investigate the effects of the novel micro-topographies on BAE-1 and HCASMC cell focal adhesion formation and actin cytoskeleton organization under physiologically static conditions.
4. To investigate the effects of the novel micro-topographies on BAE-1 cell focal adhesion formation and actin cytoskeleton organization under shear stresses that mimic the physical *in vivo* conditions.

5.1 Direct Laser Micro-fabricating Topography on Stainless Steel

Two different types of topography were laser microfabricated on the stainless steel moulds and then the inverse pattern was replicated onto the polyurethane surface. The specific features that were generated were:

(a) Microfringes (Figure 5.1a)

(b) Microripples (Figure 5.1b)

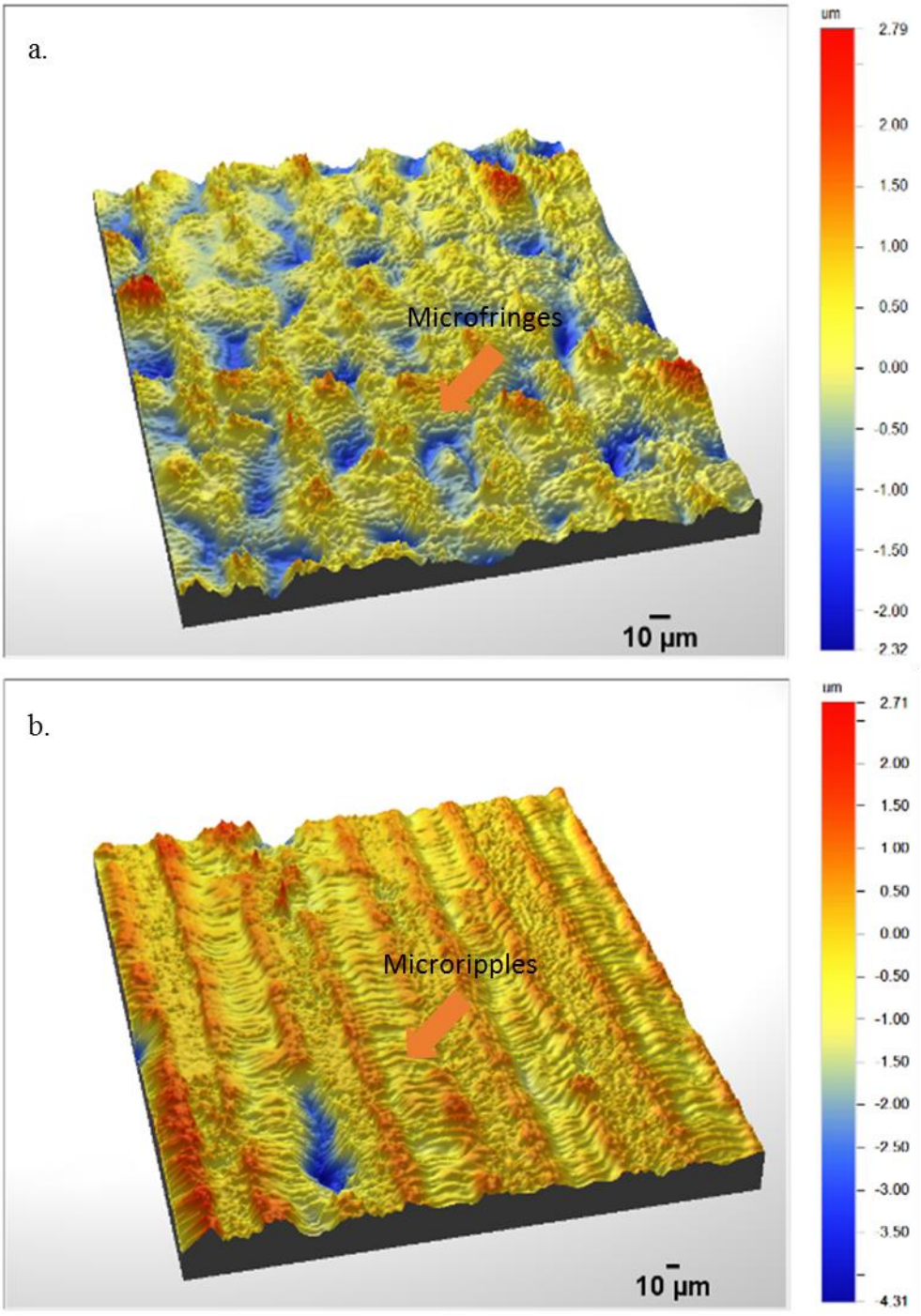

Figure 5.1 White light interferometer image of direct micro-textured surface 3D on stainless steel. (a) Microfringes, and (b) Microripples structure.

As mentioned previously in Chapter 2, most of the studies used to develop patterned surfaces incur high capital costs and are time-consuming multistep techniques, e.g. microelectromechanical systems (MEMS). This work used a cost effective, user friendly and portable solid state SPI laser system. In this laser

system, the laser beam was delivered by a fibre, to a beam expander which expands the beam ×5 before entering the galvanometer. The incoming beam is then focused using a 100mm lens (Linos F-Theta-Ronar 1064 nm+VIS) with a laser beam diameter of 21µm. The limitation of this system is that the smallest feature that can be generated is 21µm. However, larger features than this spot size are usually produced due to the effect of material melting during laser processing. The BAE-1 cell diameter, when attached to a surface, is typically between 20-30um, which is similar to the surface features generated from direct laser micro-texturing. Such relatively large features may be used to confine cells, e.g. within grooves, however large features have been shown to lack the ability to manipulate cell behaviour. Therefore, to overcome this limit of feature size resolution and to produce features smaller than the size of the laser spot, a laser beam overlapping technique was developed. This method results in the laser beam overlapping as it processes the stainless steel surface. This overlapping technique is primarily achieved by controlling the laser scanning speed and laser fluence (see Figure 7.1 in Section 7.1). The features generated include microfringes and microripples, which are approximately 3-7µm in width (Figure 5.1) and can be used to manipulate BAE-1 cell interaction and behaviour.

5.2 BAE-1 Cell Response to Indirect Laser Micro-textured Polyurethane

The work described in this thesis employed different experimental methods and techniques in order to investigate the effects of indirect laser micro-textured polyurethanes on BAE-1 cell behaviour. In particular the work wanted to understand:

(a) How the micro-textured and non-textured polyurethane affects BAE-1 cell adhesion and level of spread (as measured by cell height).

(b) To what extent micro-textured and non-textured polyurethane has an effect on BAE-1 cell proliferation?

(c) To understand how micro-textured and non-textured polyurethane affects focal adhesion formation and actin organisation in BAE-1 cells. Such knowledge will complement the adhesion and proliferation studies.

(d) To understand how micro-textured and non-textured polyurethane affects β-actin expression levels in BAE-1 cells and to link this to parameters of cell migration, e.g. velocity.

(e) To understand how micro-textured and non-textured polyurethane affects focal adhesion formation and actin organisation in BAE-1 cells under flow conditions.

5.2.1 Investigating the effect of Indirect Laser Micro-textured and Non-textured Polyurethanes on BAE-1 Cells Adhesion and Height

Very little research has been done to investigate endothelial cell adhesion on micropatterned surfaces. However, limiting the ability of endothelial cells to attach and spread on a surface has been shown to trigger programmed cell death (apoptosis) (Ruoslahti and Reed, 1994)(McGill *et al.*, 1997)(Meredith Jr and Schwartz, 1997). Endothelial cell adhesion is very important in helping control early biological responses which help coordinate other biological behaviours, such as proliferation, migration and gene/protein expression.

To investigate the effect of indirect laser micro-textured polyurethanes on BAE-1 cell adhesion, short adhesion studies were carried out. This involved exposing the BAE-1 cells to the surfaces for 2 hours and using fluorescent based assays to quantifying the number of cells that had attached to the surface after this time. Cell height was also measured using fluorescent microscopy as this gives an indirect measure of the level of spread of the cells on the surface.

The attached BAE-1 cell density was measured using PrestoBlue® fluorescence dye. This enabled us to identify which micro-textured polyurethane promoted the greatest level of BAE-1 cell adhesion after 2 hours. The BAE-1 cell height was

measured through the generation of fluorescent 3D images of cells that had been previously labelled with the fluorescent CellMask™. This cell height data was correlated with the cell adhesion data. Well spread attached cells will appear flattened, i.e. have relatively low height. In contrast, cells that do not attach to the substrate appear more rounded and have a greater cell height.

5.2.2 Investigating the Effect of Indirect Laser Micro-textured and Non-textured Polyurethane on BAE-1 Cell Proliferation

Endothelization and stent coverage speed are very important in order to reduce stent restenosis (Inoue *et al.*, 2011). The surface topography must be suitable so that the nearby endothelial cells can proliferate onto the stent surface. In order to investigate the effect of indirect laser micro-textured and non-textured polyurethanes on BAE-1 cell proliferation, BAE-1 cells were allowed to proliferate on the polyurethane surfaces for 24, 48 and 72 hours post cell seeding. Cell density was quantified every 24 hours using the PrestoBlue® fluorescence assay in order to identify those surfaces that provide the greatest level of BAE-1 cell proliferation.

5.2.3 Investigating Focal Adhesion Formation and Actin Organisation of BAE-1 cells on Indirect Laser Micro-textured and Non-textured Polyurethane Under Static Conditions

Fluorescence microscopy was used to visualise focal adhesion formation and actin organisation of BAE-1 cells cultured on indirect laser micro-textured and non-textured polyurethanes. BAE-1 cells were labelled with phalloidin and a primary anti-mouse IgG monoclonal anti-vinculin antibody, followed by a secondary anti-mouse IgG-FITC conjugated antibody and imaged using confocal microscopy.

This allowed one to identify focal adhesion formation and localization on the surfaces. Such experiments are important in helping understand how the BAE-1 cells interact with the surfaces and can help develop a greater understanding of how the micron scale features promote and organise cell adhesion, proliferation and actin filament organisation.

5.2.4 Investigating the Effects of Laser Micro-textured and Non-textured Polyurethane on β-actin Expression, Migration Velocity, Distance, and Migration Direction of BAE-1 cells

Peckham *et al*. have previously shown that increasing the expression of β-actin in myoblast cells results in a significant increase (approximately double) in cell migration velocity (Peckham *et al.*, 2001). In order to investigate cell migration velocity and directionality, time-lapse imaging was performed on the BAE-1 cells growing on the each of the laser micro-textured and non-textured polyurethane substrates. To investigate β-actin expression levels in BAE-1 cells, an in-cell enzyme-linked immunosorbent assay (ELISA) was performed. The effect of surface topography on actin expression was correlated to the data obtained on cell migration velocity.

5.2.5 Investigating Focal Adhesion Formation and Actin Organisation of BAE-1 cells on Indirect Laser Micro-textures and Non-textured Polyurethane under Flow Conditions

To investigate the combined effect of indirect laser micro-textured surfaces and shear stress (20dyn/cm^2) on BAE-1 cells, a flow system was developed. This system enabled shear stress to be applied to the BAE-1 cells. The flow rate was adjusted to mimic the shear stress experienced by endothelial cells *in vivo*. This

work allowed one to determine the effects of shear stress on BAE-1 cell morphology, focal adhesion formation and actin organisation. Cells were fluorescently labelled with phalloidin for actin visualisation and with a primary anti-mouse IgG monoclonal anti-vinculin antibody, followed by a secondary anti-mouse IgG -FITC antibody. Cells were visualised under fluorescence microscopy. This data was then compared to the data obtained on BAE-1 cells under static conditions. Such experiments under shear stress are important, as *in vivo* endothelial cells are exposed to shear stress from blood flow. Therefore, these experiments provide a more accurate representation as to what the endothelial cells may experience *in vivo*.

5.3 Investigating the Effects of Indirect Laser Micro-textured Polyurethane and Non-textured Polyurethanes on HCASMCs Behaviour

As with the studies on BAE-1 cells the same approach was adopted in order to investigate the effects of micro-textured polyurethanes and non-textured polyurethanes upon the behaviour of HCASMCs. In particular the work wanted to investigate:

(a) The effect of indirect laser micro-textured and non-textured polyurethane on HCASMCs adhesion.
(b) The effect of indirect laser micro-textured and non-textured polyurethane on HCASMCs proliferation.
(c) Actin organisation of HCASMCs on indirect laser micro-textured polyurethane.

5.3.1 Investigating the Effect of Indirect Laser Micro-textured and Non-textured Polyurethane on HCASMCs Adhesion

To investigate HCASMC adhesion on laser micro-textured and non-textured polyurethane, an MTT assay was used. The replacement of the PrestoBlue® assay with the MTT assay was necessary because the fluorescence plate reader was not available. Earlier work comparing the sensitivity of MTT and PrestoBlue® assays was found to provide consistent results. The approaches used to study HCASMCs were the same as those used with BAE-1 cells. An adhesion assay was carried out, which involved exposing the HCASMCs to the surfaces for 2 hours and quantifying the number of cells that had attached to the surface after this time, using colorimetric based assays. The attached HCASMC density was measured using the MTT assay. This enabled one to identify the suppression/enhancement effect of micro-textured polyurethane on HCASMC adhesion after 2 hours.

5.3.2 Investigating the Effect of Indirect Laser Micro-textured and Non-textured Polyurethane on HCASMCs Proliferation

In order to investigate the effect of indirect laser micro-textured and non-textured polyurethanes on HCASMCs proliferation, HCASMCs were allowed to proliferate on the polyurethane surfaces for 24, 48 and 72 hours post cell seeding. Cell density was quantified every 24 hours using the MTT assay, in order to identify the suppression/enhancement effect of a micro-textured polyurethane substrate on HCASMC cell proliferation.

5.3.3 Investigating Actin Organisation of HCASMCs on Indirect Laser Micro-textured Polyurethane Under Static Conditions

Fluorescence microscopy was used to visualise the actin organisation of HCASMC cells cultured on indirect laser micro-textured and non-textured polyurethane. HCASMC cells were labelled with phalloidin and imaged using confocal microscopy. This allowed one to identify actin alignment on the surfaces. Such experiments are important for helping in comparing the response sensitivity of HCAMSC cells and BAE-1 cells to the surfaces.

Chapter 6

6.0 Materials and Methods

6.1 Materials

The following materials and equipment were obtained from the suppliers listed below:

Biomer Technology Ltd, UK

Series ‘A’ polyurethane Z1A1 Polyurethane

Sigma

Foetal bovine serum, Bovine serum albumin, Penicillin/streptomycin, Triton X-100, Paraformaldehyde, Fluoromount aqueous mounting medium, Primary anti-mouse IgG monoclonal anti-vinculin antibody, 3, 3’, 5, 5’-Tetramethylbenzidine liquid substrate (TMB), Secondary anti-mouse IgG -FITC antibody, Hydrogen peroxide, 1N hydrochloric acid, and 4',6-Diamidino-2-Phenylindole, Dihydrochloride (DAPI).

TED PELLA, Inc, USA

Harris Uni-Core™ punch

Cytoskeleton, Inc., USA

Acti-stainTM 555 fluorescent phalloidin

Appleton Woods, UK

Sterile serological pipettes (5 and 10ml), and glass microscope slides (75×25×1.1mm)

Scientific Laboratory Supplies Ltd, UK

Sure seal sterile universal tubes (25ml)

Severn Biotech, UK

Tris (hydroxymethyl)aminomethane (Tris)

Invitrogen, UK

Ham's F-12 Nutrient Mix, GlutaMAX™, PrestoBlue® Cell Viability Reagent, and CellMask™

Cell Signalling Technology, Inc.

Anti-rabbit IgG, and Horse Radish Peroxidase (HRP)-linked antibody

Ibidi, Germany

Sticky-Slide I Luer, Coverslips for sticky-Slides, No. 1.5 (170 µm +/- 10 µm) D 263 M Schott glass, unsterile, 25 mm x 75 mm, Silicone Tubing 1.6 mm ID, 5 m, silicone, sterile, and Elbow Luer connector, male Luer to single barb, elbow style for all µ-Slides Luer, white Polypropylene, sterile.

6.2 Major Equipment

The following equipment was used to perform the research described in this thesis:

BMG LABTECH, Germany

FLUOstar OPTIMA fluorescence plate reader

Molecular Devices, USA

SpectraMax 250 Microplate Reader

Zeiss, UK

Laser Scanning Confocal Microscope, model 510 META

Asylum Research, USA

Molecular Force Probe-3D Microscope (MFP-3D)

Watson-Marlow, UK

100 series 114DV flip-top single-channel pumphead

Veeco, UK

Wyko White Light Interferometer NT1100

SPI Laser, UK

20W Nano Second Pulsed Fibre Laser System

PeCon GmbH, Germany

Tempcontrol 37-2 and CTI-controller 3700

6.3 Methods

6.3.1 Laser surface Set-up and Surface micro-fabrication

The experiments were performed using an SPI solid state pulsed fibre laser system (SPI Laser, UK) with a maximum mean laser power (P) of 20W, wavelength (λ) of 1064 nm and variable pulse duration (τ) of 9-200ns. The laser beam was delivered through a fibre and then it was collimated and expanded up to 10mm through a 5x beam expander. The expanded beam was then propagated to a galvanometer (scanning head), which consists of two mirrors that control the laser beam path across the work piece. A translational x-y-z table (Aerotech Inc, UK) was used to accurately position the sample at the focal position of the processing lens. The reflected beam was then focused using a 100mm focal length lens (Linos F-Theta-Ronar 1064 nm+VIS) which produced a focused spot size of 21µm in diameter. The set-up of the experimental system is shown in Figure 6.1.

A 1mm thick stainless steel plate was used to laser machine micro-moulds in these experiments. Briefly, a medical grade stainless steel plate was laser micro-textured to produce a mould which was then used to transfer the inverse pattern of the micro-textured features onto a Z1A1 polyurethane thin film.

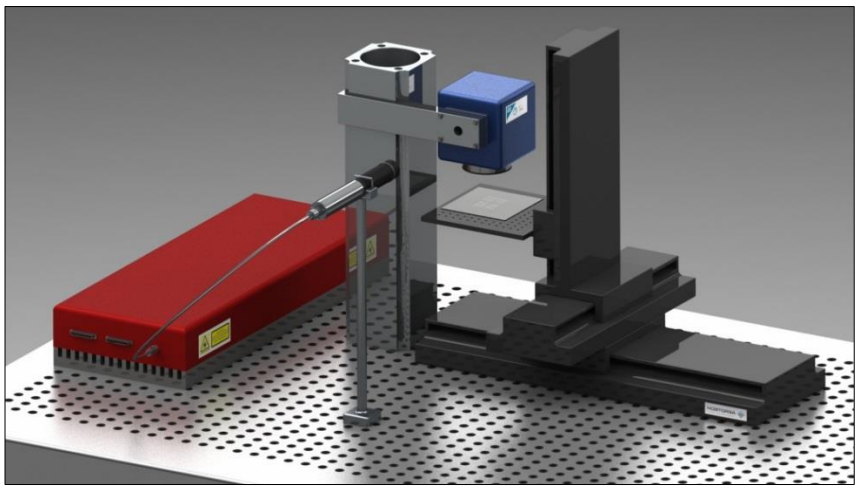

Figure 6.1 The set-up of the SPI solid state pulsed fibre laser system for microfabrication.

6.3.2 Polyurethane Casting

Z1A1 Polyurethane (Series 'A' polyurethane) was supplied by Biomer Technology Ltd. Briefly, 8% polyurethane pallets were dissolved in a solvent ratio of 2-Dimethylformamide (DMF): 1-Tetrahydrofuran (THF) and were mixed overnight on a roller mixer. Concentration of polyurethane in the range of between 5 to 20% was used to optimise and increase the efficiency of polyurethane casting. 8% polyurethane was found the best concentration for replication. The stainless steel micro-textured template was clamped with a square metal frame to control the polyurethane thickness. Ready-made polyurethane solution was poured onto the mould and swirled until the polyurethane solution made full contact with the edge of the frame. The polyurethane was then cured in the oven at 60˚C for 2 hours.

6.3.3 Characterization of Laser Micro-textured Patterns on Polyurethanes

The polyurethane solution was poured onto the laser micro-machined stainless steel master template to create a thin film. The film was then cured in an oven for two hours so that the solvent was driven off. Both laser micro-textured and non-textured polyurethane films were cast. The laser micro-textured pattern on polyurethane surfaces were characterized using a white light interferometer Wyko NT1100 at 10x magnification (University of Liverpool) and analysed using Veeco vision software.

6.3.4 Routine Cell Culture

Bovine aorta endothelial cells (BAE-1) were obtained from Sigma-Aldrich UK. Cells were cultured in Ham's F-12 Nutrient Mix, GlutaMAX™ (F-12, Life Technologies, USA) supplemented with 10% foetal bovine serum (FBS, Sigma-Aldrich) and 100units/mL penicillin/streptomycin (P/S, Sigma-Aldrich). The cells were incubated at 37°C/ 5% CO2 in a 95% humidified atmosphere and sub-

cultured every 2-3 days at a ratio of 1:4. Human Coronary Artery Smooth Muscle Cells (HCASMCs -a gift from Professor Rachael William, Liverpool University), were maintained in smooth muscle cell growth medium 2 (PromoCell GmbH, Germany) supplemented with 0.05 ml/ml foetal calf serum, 0.5ng/ml epidermal growth factor (recombinant human), 2ng/ml basic fibroblast growth factor (recombinant human), 5µg/ml insulin (recombinant human) and 100units/mL penicillin/streptomycin (P/S, Sigma-Aldrich). The cells were incubated at 37°C/5% CO2 in a 95% humidified atmosphere and sub-cultured when 70-90% confluent.

6.3.5 Cell Adhesion and Proliferation Assays

PrestoBlue® Cell Viability Reagent (Life Technologies, USA) was used to study BAE-1 cell adhesion and proliferation on both the laser micro-textured and non-textured Z1A1 polyurethane substrates. A FLUOstar OPTIMA fluorescence plate reader (BMG LABTECH, Germany) was used to acquire the fluorescent readings.

A MTT (Thiazolyl Blue Tetrazolium Bromide, Sigma-Aldrich) assay was used to study HCASMCs adhesion and proliferation on both the laser micro-textured and non-textured Z1A1 polyurethane substrates. The absorbance was measured by using a SpectraMAX 190 (Molecular biology) and a fluorescence spectrometer.

6.3.6 Focal adhesion and actin staining

BAE-1 cells were seeded onto the polymer substrates at a cell density of 10,000 cells/cm^2 and left to incubate at 37°C for 2 hours. Next, the cells were fixed in 3.75% (w/v) paraformaldehyde (Sigma-Aldrich) then permeabilised with 0.1% (v/v) Triton X-100 (Sigma-Aldrich). The samples were then blocked with 1% (w/v) bovine serum albumin (BSA, Sigma-Aldrich) for 1 hours. Double staining techniques were used for staining vinculin (focal adhesion). Both primary anti-mouse IgG monoclonal anti-vinculin antibody (dilution 1 in 25, 50, and 100) and secondary anti-mouse IgG -FITC antibody (dilution 1 in 500, 1000, and 2000)

were optimized. First the cells were incubated with a primary anti-mouse IgG monoclonal anti-vinculin antibody for 24 hours (1 in 50 dilution, Sigma-Aldrich). The cells were then incubated in the dark with a secondary anti-mouse IgG -FITC antibody (1 in 1000 dilution Sigma-Aldrich) for 2 hours. For staining actin the samples were incubated with Acti-stainTM 555 fluorescent phalloidin (100nM, Cytoskeleton, Inc.). DAPI was used to stain the nucleus (25µg/mL, Sigma-Aldrich). The samples were mounted on a glass coverslip microscope slide using fluoromount aqueous mounting medium (Sigma-Aldrich). The samples were imaged using a Zeiss CLSM-510 confocal microscope using a 63× Plan-Apo/1.4 NA Oil in a differential interference contrast mode (DIC).

6.3.7 Cell Height Profile Measurement

In order to investigate the effects of the micro-textured substrates on cell height, the cell membranes of BAE-1 cells were stained and the cells imaged using confocal microscopy. BAE-1 cells were seeded onto the polymer substrates at a cell density of 10,000 cells/cm^2 and left for 2 hours to attach. After 2 hours the BAE-1 cells were fixed with 3.75% (w/v) formaldehyde in PBS for 10 minutes and were then washed (x3) with PBS. Next, the cells were incubated with CellMask^{TM} in PBS (2.5µg/mL, Life Technologies, USA) for 10minutes at room temperature. The samples were then washed (x3) with PBS and inverted onto glass microscope slides using fluoromount aqueous mounting medium. The cells were imaged using z-stacked mode under a Zeiss LSM-510 confocal microscope with a 40× Plan-Neo/1.3 NA Oil objective lens. Images were analysed using the Zeiss Zen 2012 imaging software.

6.3.8 Live Cell Imaging for Cell Migration, Velocity, Distance, Forward Migration Index and Directionality

Micro-textured and non-textured polyurethane substrates were prepared as described in Section 6.3. The polymer substrates were attached to the 35mm petri dish and the cells seeded onto the substrates at a density of 10,000 cells/cm^2. The 35mm petri dish (containing cells/substrates) were immediately incubated in the microscope's environmental chamber (S-2, PeCon GmbH, Germany). The S-2 chamber was maintained at 37˚C/5% CO_2 in a 60-70% humidified air atmosphere by use of the Tempcontrol 37-2 and CTI-controller 3700 (PeCon GmbH, Germany). Images were captured every 10 minutes for 8 hours using a 20× Plan-Apo/0.75 NA DIC objective lens and illuminated using a Helium-Neon (HeNe) laser at 543nm wavelength. An X-Y-Z automated control stage was programmed to automatically position the samples. ImageJ software (National Institute of Health's, NIH) with manual tracking plugin (Institute Curie, France) was used to analyse the data produced from the manual tracking data. The cell movements were analysed using a chemotaxis and migration tool software (ibidi, Germany).

In order to investigate the effects of the surface topography on cell migration directionality, the cell forward migration index (FMI) was used. The FMI represents the efficiency of cell migration in relation to the x_{FMI} (migration parallel to the microfringe or microripple structures) and y_{FMI} (migration perpendicular to the microfringe or microripple structures) axis. A high positive or negative FMI index indicates that a high number of cells within the population migrated either parallel to, or perpendicular to, the surface features.

6.3.9 β-actin protein expression level

For studying endogenous β-action protein expression, an in-cell ELISA assay was used. Micro-textured and non-textured polyurethanes were cut into 6mm circles using a 6mm Harris Uni-Core™ punch (TED PELLA, Inc, USA) and inserted into the wells of a 96 well plate. Each well was seeded with 20,000 cells which were cultured for 24 hours. After 24 hours the cells were fixed with 4% (w/v) formaldehyde in Tris buffered saline (TBS, 50mM Tris, 150mM NaCl, pH=7.) and permeabilised with 0.1% (v/v) Triton X-100 in TBS. The samples were incubated

in 1% (v/v) hydrogen peroxide (Sigma-Aldrich) in TBS to quench endogenous peroxidase. After blocking the cells with 1% (w/v) BSA, the cells were incubated with β-actin rabbit monoclonal antibody (1in1000 dilution, Cell Signalling Technology, Inc.) overnight at 4˚C. The samples were then incubated with anti-rabbit IgG, Horse Radish Peroxidase (HRP)-linked antibody (1:1000, Cell Signalling Technology, Inc.). The samples were incubated in supersensitive 3, 3', 5, 5'-Tetramethylbenzidine liquid substrate (TMB, Sigma-Aldrich). 1N hydrochloric acid (HCI, Sigma-Aldrich) stop solution was added to stop the reaction. The plates were then read at 450nm using a colorimetric spectrophotometer (SPECTRAMAX 190, Molecular device).

6.4 Shear Stress Flow System

The shear stress flow system is shown in Figure 6.2c. The polymer substrates were attached to the sticky-Slide I Luer (Ibidi, Germany) and the cells seeding density was optimized starting from 5,000 to 20,000 cells/cm^2. The sticky-Slide I Luer (containing cells/substrates) were immediately incubated in the microscope environmental chamber) (figure 6.2b). The S-2 chamber was maintained at 37˚C by the Tempcontrol 37-2 and CTI-controller 3700. The sticky-Slide I Luer was connected to the reservoir containing Ham's F-12 medium, which was maintained at 37˚C/5% CO2 in the temperature controlled water bath via the CTI-controller 3700. A peristaltic pump was clipped at the tube in between the reservoir and the sticky-Slide I Luer to generate a flow (Figure 6.2a). Confocal images were captured every 10 minutes for 8 hours using a 20× Plan-Apo/0.75 NA DIC objective lens and a Helium-Neon (HeNe) laser at 543nm wavelength to illuminate the cells. An X-Y-Z automated control stage was programmed to automatically position the samples. After 24 hours under flow conditions, all the samples were stained with primary anti-mouse IgG monoclonal anti-vinculin antibody, secondary anti-mouse IgG -FITC antibody, Acti-stainTM 555 fluorescent phalloidin and DAPI (the staining method was similar to section in 6.3.6, except the cells were exposed to shear stress). The viscosity of Ham F-12 medium and 20dyn/cm^2 shear stress were calculated using the equation shown below:

Dynamic Viscosity equation

$$\eta = Cpt \tag{6.1}$$

Where C is the instrument constant, p is the density of the fluid, t is the time of the fluid, and Φ is the flow rate.

Ibidi μ-slide $1^{0.6}$ Luer shear stress equation

$$\tau\left[\frac{dyne}{cm^2}\right] = \eta\left[\frac{dyne}{cm^2}\right] * 60.1\Phi\left[\frac{ml}{min}\right] \tag{6.2}$$

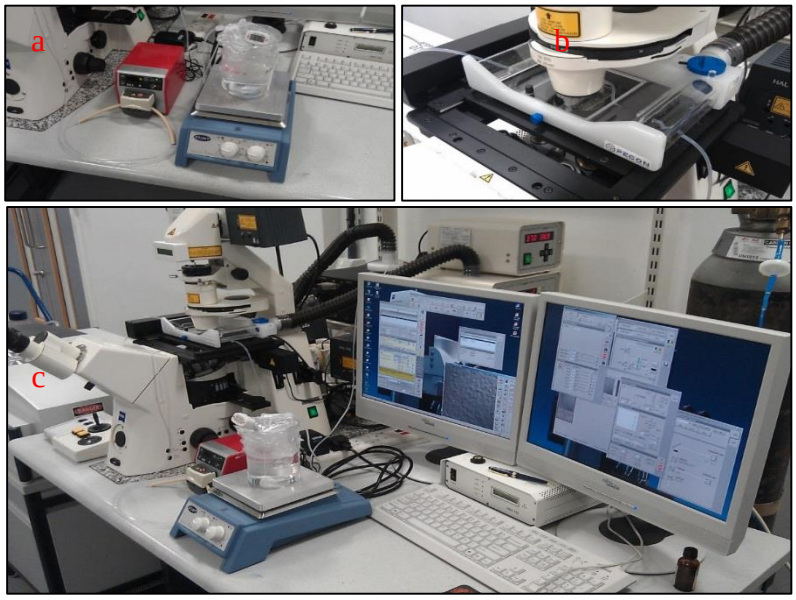

Figure 6.2 (a) A peristaltic pump was connected in between the reservoir and sticky-Slide I Luer. (b) The sticky-slide I Luer was placed in the S-2 chamber to maintain the temperature. (c) The overview of the whole system.

6.5 Statistical analysis

Data are presented as mean values ± standard error of the mean (StEM). Statistical significances were analysed using an unpaired t-test with an error probability,

$P \geq 0.05$, $P \geq 0.01$ and $P \geq 0.001$. Differences were considered as being statistically significant when $P < 0.05$.

Chapter 7

7.0 Results of Direct Laser Fabrication of Micro Topography on Stainless Steel

7.1 Investigating Laser Beam Spot interaction on a Single Hatching Line

At the beginning of the experiment, micropillars were produced to control cell adhesion and proliferation. However, the micropillar dimension was larger than the cellular diameter, which did not exhibit any great level of control on endothelial cell behaviour. Therefore, an alternative route for producing micro-structures smaller than the cellular dimension was sought, namely the laser beam-overlapping technique (the laser microfabricated pillars are shown in Appendix 2).

In the initial investigation of the laser microfabrication process, a single hatching line was micro-textured onto a stainless steel substrate at a scanning speed of 1800mm/s with an average laser power of 15W, a repetition rate of 25 KHz, and a pulse duration of 200ns. Using the above laser parameters a single line of separated laser beam spots were machined onto a stainless steel substrate and the profile of the interaction zones was captured with a microscope camera, (Figure 7.1a). It can be seen that each of the beam spot borders has an elevated rim. This phenomenon suggests that a melt expulsion mechanism is responsible for the production of this structure, where the evaporation and secondary recoil pressure (the pressure generated by vaporisation during vapour expansion) pushes the melt pool out from the centre of the beam spot during laser fabrication. This material then forms a solidified elevated rim from the liquid metal when it has cooled down.

A decrease was then made to the laser scanning speed reducing it to 800mm/s, but still keeping the same laser parameters, and it was observed that the laser beam spots became overlapped, (Figure 7.1b), and that the elevated rim was less uniform when compared to that produced by laser beam scan speeds of 1800 mm/sec. The

result suggests that a decrease in laser scanning speed can distort the uniformity of the rim formation. The reduction in laser scanning speed results in an increase in thermal incubation into the substrate and subsequently results in thermal distortion of the elevated rim formation. Hence, laser microfabrication parameters must be optimized to produce microfringes and microripple structures on a stainless steel substrate.

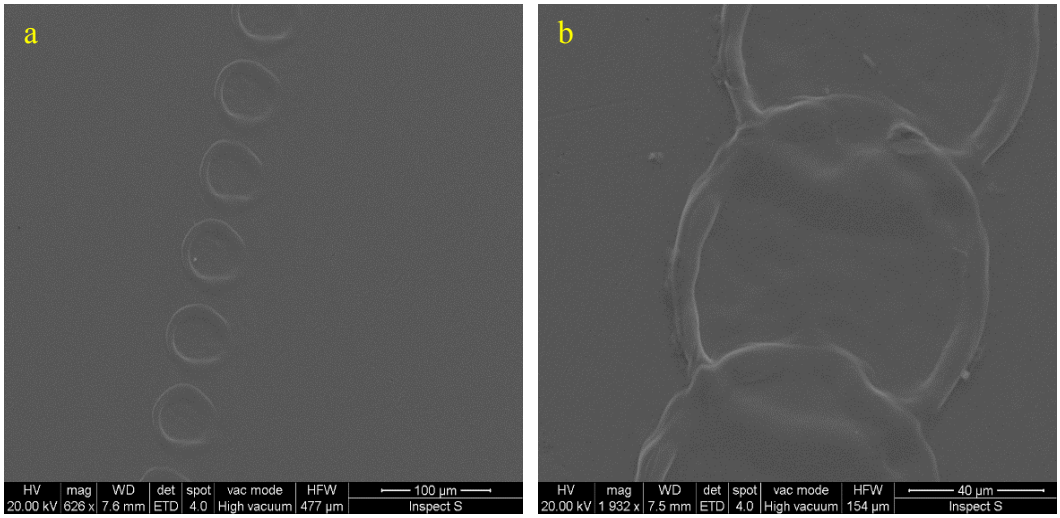

Figure 7.1 The SEM images showed the laser spot (a) Single hatching line micro-textured at 1800mm/s. (b) Single hatching line micro-textured at 800mm/s.

7.2 Optimization of Direct Laser Microfringe Microfabrication

Table 7.1 shows the parameter sets used in the optimisation experiments that generated the microfringe structures. These parameters were derived from initial experiments that mapped out the parameter space for different sets of laser parameters, as shown in Table 7.1. These were then used to optimize the laser for microfringe generation. The pulse energy and laser fluence was calculated using Equations 7.1 and 7.2, respectively.

$$Laser\ pulse\ \ enegry = \frac{Mean\ laser\ power}{Laser\ repetition\ rate} \tag{7.1}$$

$$Laser\ fluence\ = \frac{Laser\ pulse\ energy}{Laser\ focal\ Spot\ Area} \tag{7.2}$$

Laser parameter set 1, with a fluence of 0.03mJ/cm^2 was initially used to generate a microfringe topography on a stainless steel substrate. The 3D white light interferometer image of the surface shown in Figure 7.1a shows that the stainless steel surface was micro-textured with microridges and irregular features within the microgrooves. No obvious microfringe feature was observed within the microgrooves. Using laser parameter set 2 to generate microripple features, a larger irregular feature and some microfringes were observed by increasing the laser scanning passes from 15 to 25 passes (Figure 7.2b).

Using laser parameter set 3, microfringes were successfully generated by increasing the laser fluence to 0.06mJ/cm^2 (Figure 7.2c). Further laser parameter optimisation experiments were conducted, in which increasing or decreasing laser scanning passes or average laser power, was investigated, but no improvement in the generation of regular microfringe features was observed. It was observed however, that further experiments in which the average laser power and the number of scanning passes were increasing led to a reduction in microridge formation on the stainless steel surface. Therefore, laser parameter set 3 was selected as representing the best settings for direct laser textured surfaces 1A and 1D. Using laser parameter set 3, and surface 1D, these parameters were used to investigate the production of microfringes with small widths, by changing the laser hatching spacing to 10µm. This destroyed all of the microfringe topography, and instead, produced a wavy topography on the surface (Figure 7.3). This helped to identify the microfringe effect on BAE-1 cells. Direct laser textured surface 1A and 1D were used as master moulds for polyurethane casting.

Table 7.1 Three sets of laser parameters were used to optimize the laser for microfringe generation

Laser parameters	**Set 1**	**Set 2**	**Set 3**
Mean laser power	5W	5W	10W
Pulse duration	9ns	9ns	9ns
Repetition rate	500kHz	500kHz	500kHz
Laser scanning speed	500mm/s	500mm/s	500mm/s
Laser scanning passes	15	25	25

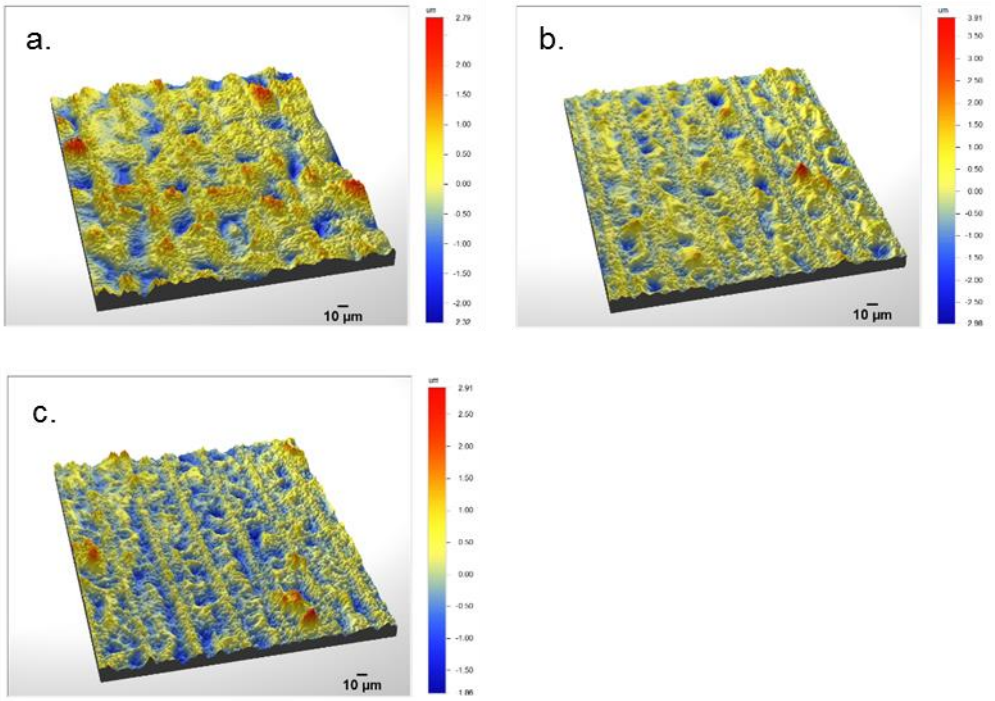

Figure 7.2 Surface topographies were generated using different set of laser parameter: (a) set 1, (b) set 2 and (c) set 3 laser parameters

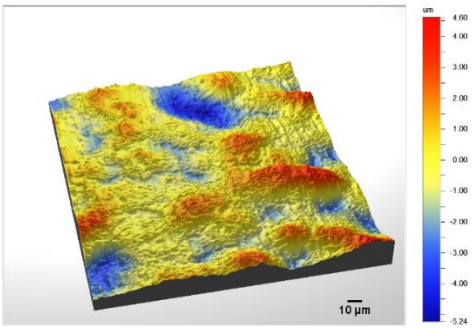

Figure 7.3 White light interferometer image of direct laser micro-textured surface 1D on stainless steel.

7.3 Optimization of Direct laser Microripple Microfabrication

Different laser parameter sets were investigated, for the generation and optimisation, of the microripple features on a stainless steel surface. An initial experiment was performed, using laser parameter set 1, shown in Table 7.2, to produce a microfringe topography with a laser fluence of 0.003J/cm^2 and 5 scan passes. No microripple features were observed on the surface of the steel substrate when using this configuration. A 3D white light interferometer image of the surface can be seen in Figure 7.4a.

A periodical microripple structure was successfully generated on the stainless steel by increasing the laser fluence to 0.005J/cm^2 using laser parameter set 2 with similar number of passes as used previously in set 1 (Figure 7.4b). Laser parameter set 2 was also used to generate microripples by increasing the laser scanning pass number to 10, i.e. 10 passes. The results showed that an increase in the number of laser scanning passes caused a widening in the widths of the microridge structures, while at the same time, a corresponding narrowing of the microgroove that contains the microripples, which is undesirable with respect to cell control (Figure 7.4c). The results from the laser optimization experiments showed that laser parameter set 2 was the best setting for microripple generation for direct laser textured surfaces 3A and 3D. The only difference between surfaces 3A and 3D was the hatch spacing, where the hatch spacing's for 3A and 3D, were 60µm and 30µm, respectively. A white light interferometer image of the direct micro-

textured 3D surface on stainless steel is shown in Figure 7.5. Direct laser textured surfaces 3A and 3D were then used as a master mould for polyurethane casting.

Table 7.2. Three sets of laser parameters were used to optimize the laser for microripple generation

Laser parameters	**Set 1**	**Set 2**	**Set 3**
Mean laser power	3W	4W	4W
Pulse duration	200ns	200ns	200ns
Repetition rate	25kHz	25kHz	25kHz
Laser scanning speed	170mm/s	170mm/s	170mm/s
Laser scanning passes	5	5	10

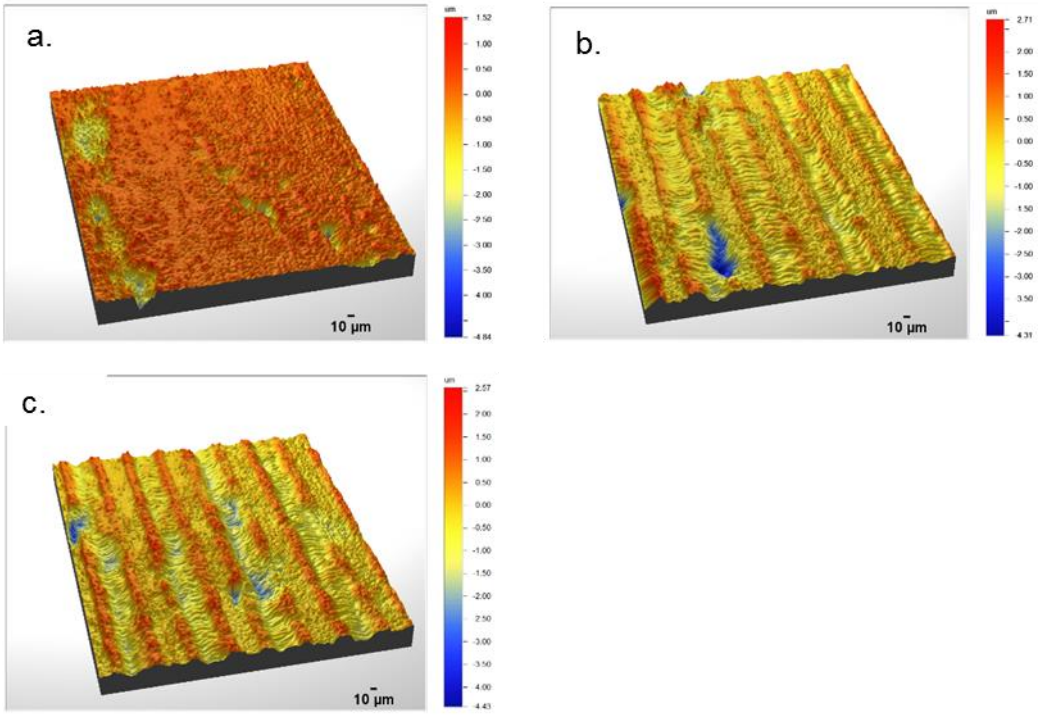

Figure 7.4 Surface topographies were generated on stainless steel using 3 sets of laser parameter for optimization of laser setting: (a) for set 1 laser parameter no fabrication was observed, (b) set 2 laser parameter produced microripple and microridges, and (c) set 3 laser parameters produced the same structure as shown set 2 laser parameter but with deeper microgrooves and higher microridges.

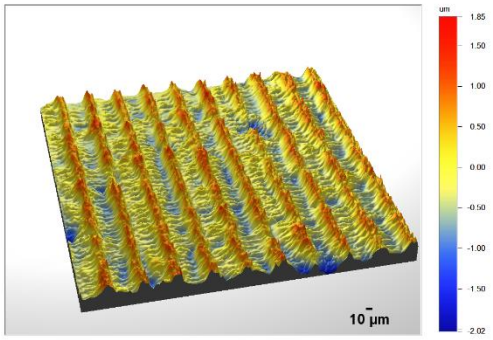

Figure 7.5 Set 2 laser parameter was used to produce another surface named 3D with deeper microgrooves and microridges with smaller in width.

7.4 Characterization of Laser Micro-textured Polyurethanes Cast off from a Stainless Steel Master Template

The laser micro-textured features were replicated/cast from a stainless steel mould using Z1A1 polyurethane provided from Biomer Technology Ltd and the microstructures were characterised using a vision 2D analysis package. The four indirect laser textured polyurethane films are shown in Figure 7.7 and 7.8. The four indirect laser micro-textured cast thin films were named as polyurethane 1A, 1D, 3A and 3D, respectively. Polyurethane films 1A, 1D, 3A, and 3D, the surface profiles, and the measurements are shown in Tables 7.3.1 and 7.3.2 and the surface description is shown in figure 7.6. Figure 7.7a showed that the polyurethane 1A surface contains discontinue microripple or named microfringes with some irregular features (i.e. burn and holes) and microgrooves. The surface for polyurethane 1D was wavy and without any microfringes and was used to identify the effect of microfringe structure on BAE-1 cells (Figure 7.7b). The microripple structures evident on polyurethane 3A were less when compared to those of polyurethane 3D (Figure 7.8). It was also observed that the microripple structure on polyurethane 3D were more regular, uniform and deeper in the microripple gap than the others.

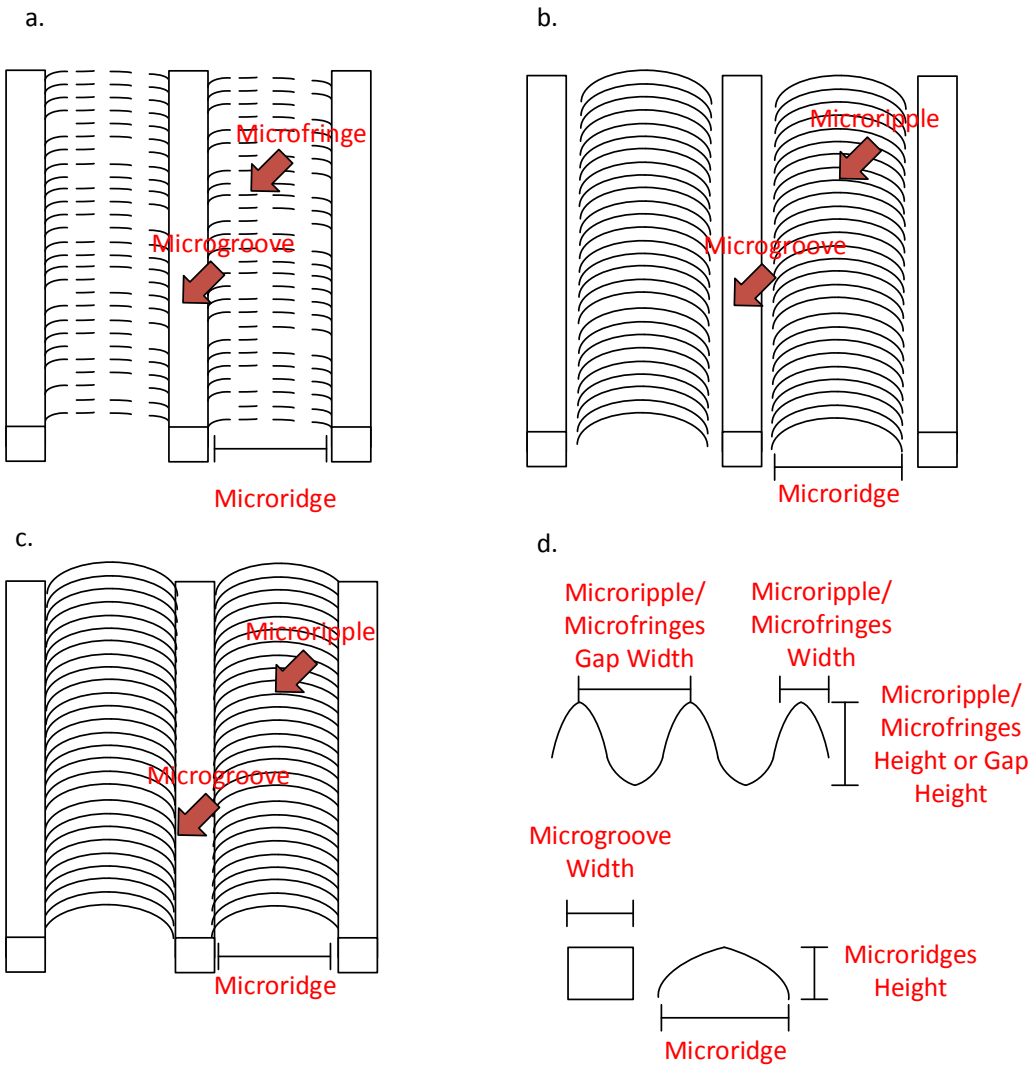

Figure 7.6 This diagram is used to help describe the laser micro-textured surface dimension measurement and characterisation process. (a) polyurethane 1A with discontinuous microripples, or named as microfringes, (b) polyurethane 3A with microripples, (c) polyurethane 3D with smaller microridge spacing, and (d) surface measurement and guidance.

Table 7.3. Surface measurement of indirect laser micro-textured polyurethanes 1A and 1D. Data are presented as mean ± SD, and ɳ=20.

Measurement area/samples	Polyurethane 1A	Polyurethane 1D
Microfringes width	4.05±0.67µm	n/a
Microfringes height	0.11±0.07µm	n/a
Microfringes gap	4.15±4.15µm	n/a
Microridge width	27.16±2.01µm	n/a
Microridge height	0.9±0.34µm	n/a
Microgroove	11.15±1.72µm	n/a

Table 7.4. Surface measurement of indirect laser micro-textured polyurethanes 3A and 3D. Data are presented as mean ± SD, and ɳ=20.

Measurement area/samples	Polyurethane 3A	Polyurethane 3D
Microripple width	6.23±1.26µm	6.27±0.82µm
Microripple height	0.17±0.06µm	0.21±0.07µm
Microripple gap	5.86±1.09µm	6.59±1.21µm
Microridge width	40.09±1.82µm	23.47±1.74µm
Microridge height	0.71±0.22µm	1.23±0.27µm
Microgroove	19.41±2.54µm	18.36±1.58µm

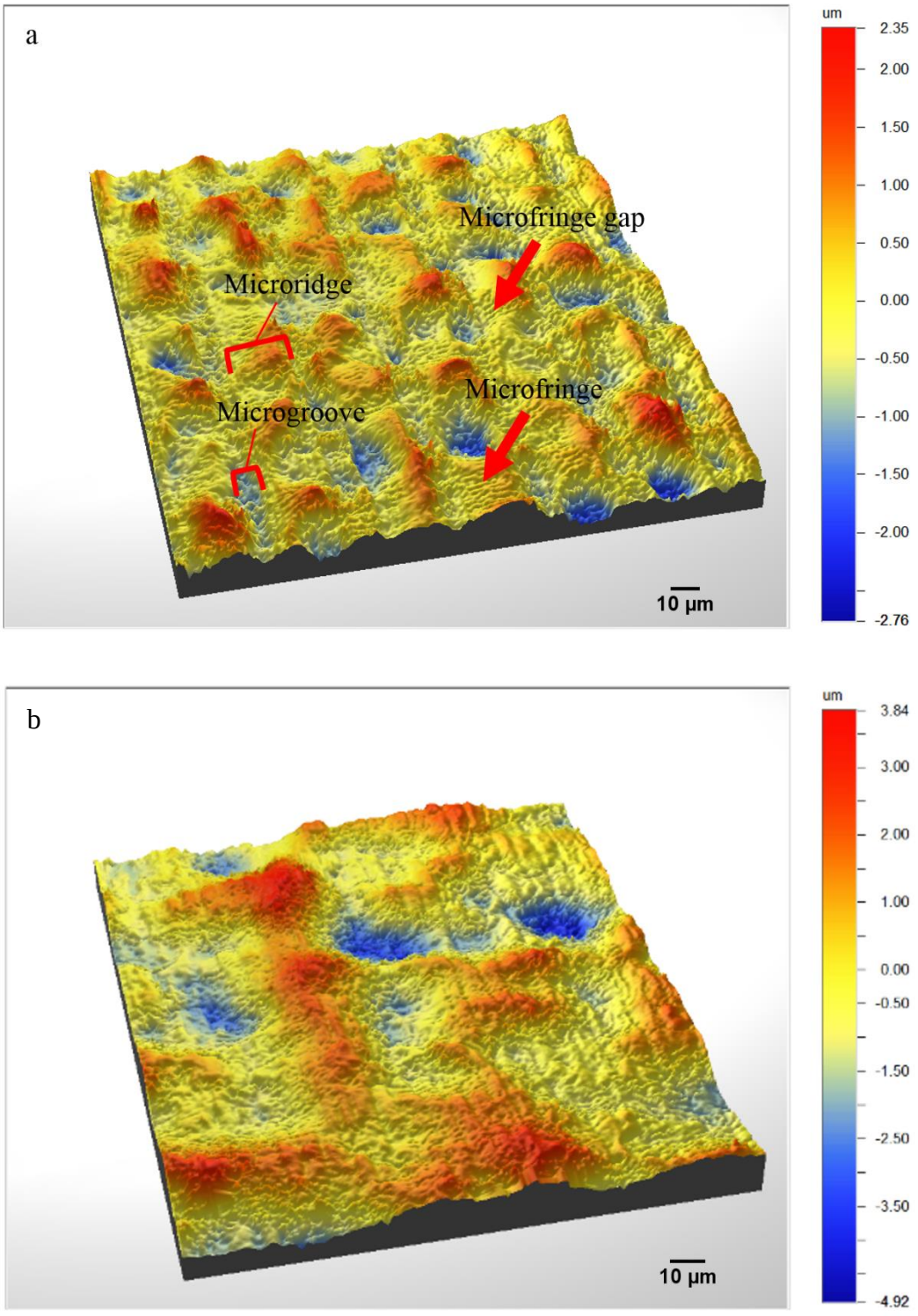

Figure 7.7 White light interferometer images of indirect laser micro-textured polyurethanes cast off from a stainless steel master template. (a) Polyurethane 1A. (b) Polyurethane 1D.

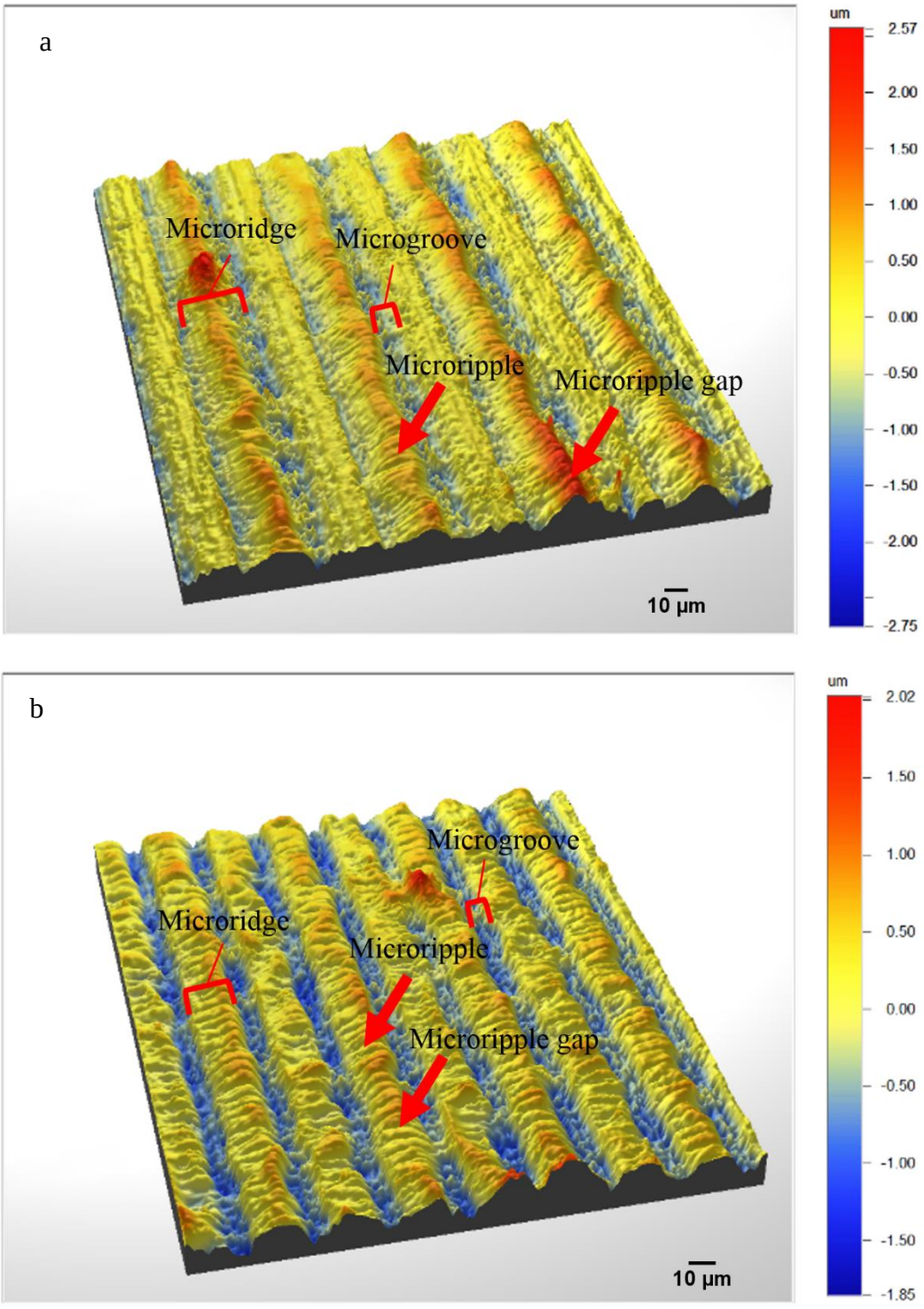

Figure 7.8 White light interferometer images of indirect laser micro-textured polyurethanes cast off from a stainless steel master template. (a) Polyurethane 3A and (b) Polyurethane 3D.

Chapter 8

8.0 Results of BAE-1 Cell Responses to Indirect Laser Micro-textured Polyurethane and Non-textured Polyurethane

8.1 Calibration Curve Generation for BAE-1 Cell Adhesion and Proliferation Assays

Before performing cell adhesion and proliferation assays using PrestoBlue®, a standard curve was produced. This was achieved by carrying out a serial dilution of BAE-1 cells (from 100,000 cells to 96 cells) which were seeded into the wells of a 96-well plate. The assay was then performed to obtain the fluorescent signal, which is relative to the number of cells. Figure 8.1 shows the calibration curve where it can be seen that there is a linear correction between the fluorescent signal and the absolute cell number.

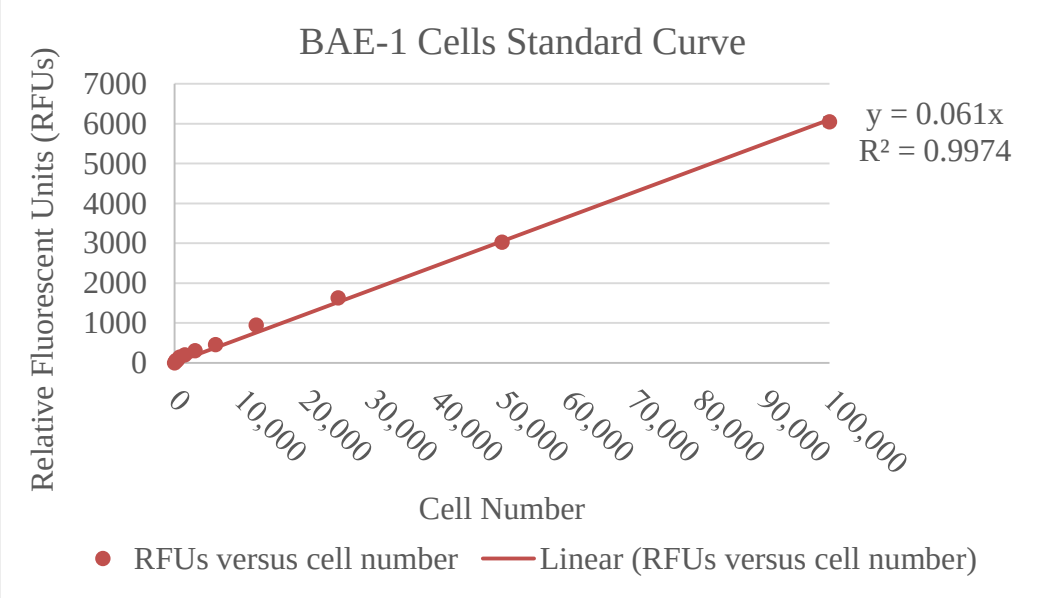

Figure 8.1 Standard curved generated by obtaining the fluorescent signal emitted from BAE-1 cells treated with PrestoBlue®. A linear correction was found between fluorescent signal and absolute cell number.

8.2 Investigating the Effect of Indirect Laser Micro-textured and Non-textured Polyurethanes on BAE-1 Cell Adhesion and Cell Height Profile Under Static Conditions

8.2.1 BAE-1 Cell Adhesion Assay

The effect of indirect laser micro-textured and non-textured polyurethanes on BAE-1 cell retention was investigated. Before performing the cell adhesion assay, BAE-1 cells density were optimised and seeded at a cell density of 10,000 cells on to the non-textured polyurethane to observe the cell attachment to the surface every hour. It was found that the minimum time required for cells to begin to form adhesions was 1 hour (Figure 8.2). Therefore a 2 hour period post seeding was used for the cell adhesion assay.

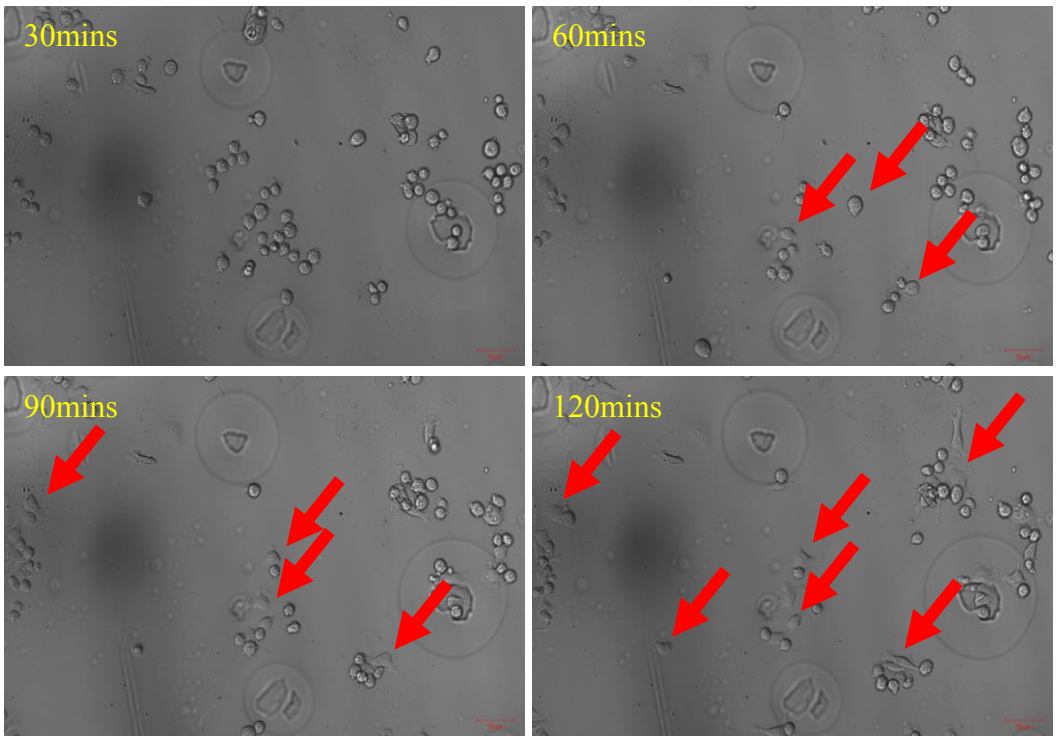

Figure 8.2 The differential interference contrast (DIC) images show the BAE-1 cell adhesion process at 20, 60, 90 and 120mins. The red arrows showthose BAE-1 cells attaching to the non-textured polyurethane after 60minutes, with a greater level of cell attachment being seen after 90 and 120 minutes respectively.

The cell adhesion assay was carried out using 10,000 cells per substrate and the cells were subsequently left to incubate for two hours. After two hours the cells were gently washed and the PrestoBlue® assay was carried out to quantify cell retention. As can be seen from Figure 8.3, the results show that the number of BAE-1 cells retained on polyurethane 1A was approximately 3-fold higher than the control with a significant difference of $P<0.001$. Moreover, the number of cells retained on polyurethane 1A was also found to be significantly higher compared with the other polymers: polyurethane 1D ($P<0.01$), 3A ($P<0.01$), and 3D ($P<0.01$). Ultimately, no significant difference was found between the mean number of cells attached to polyurethane 1D, 3A and 3D compared to the non-textured polyurethane control. These experiments were repeated three times and each time this basic trend was observed.

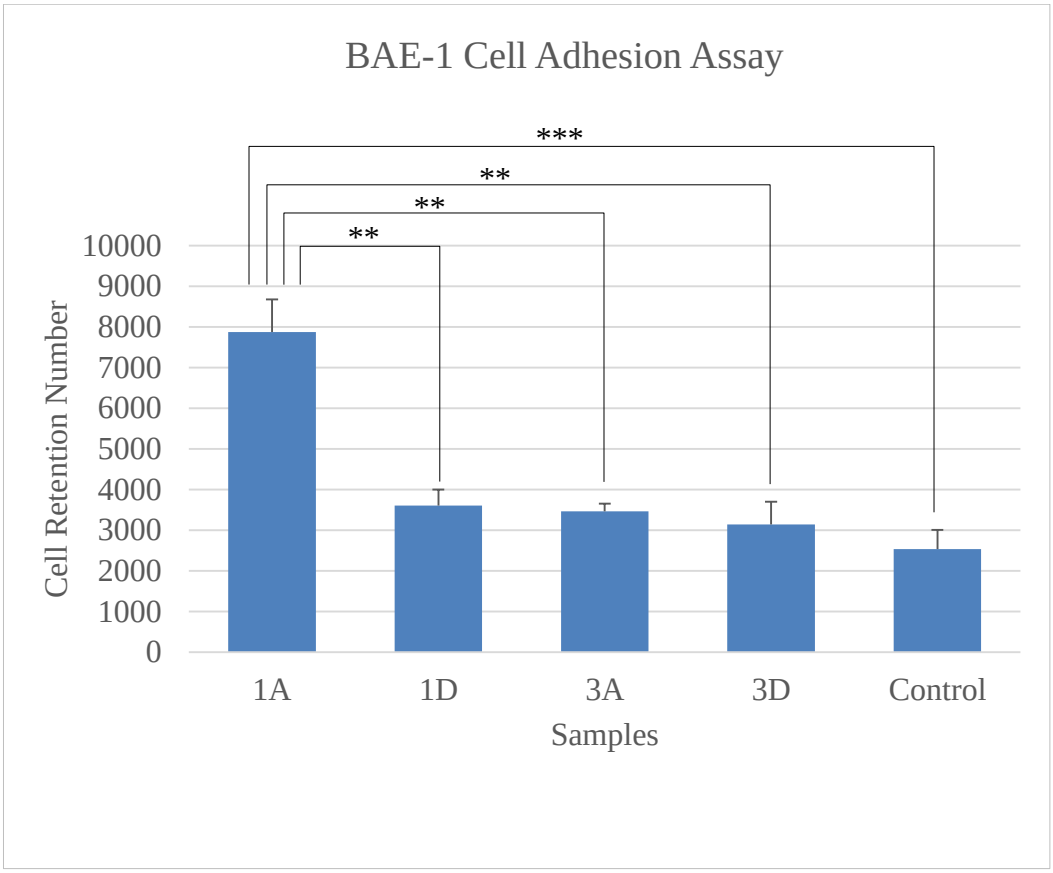

Figure 8.3 BAE-1 cell adhesion was significantly greater on polyurethane 1A compared to polyurethane 1D, 3A, 3D and non-textured polyurethanes at 2 hours post seeding. Data are presented as mean (± StEM).P<0.01, ***P<0.001 (η=6).**

8.2.2 BAE-1 Cell Height Profile

The first biological response of a cell to a surface is cell adhesion. This is followed by cell flattening, elongation, migration and proliferation. At the beginning of the cell adhesion process, the cells appeared rounded and were observed to have a relatively high cell height. However, once the cells were observed to have loosely adhered to the surface, the cells started to flatten and reduce in cell height (Figure 8.4). Hence, the cell height profile could be used to as a qualitative, indirect measure of cell adhesion.

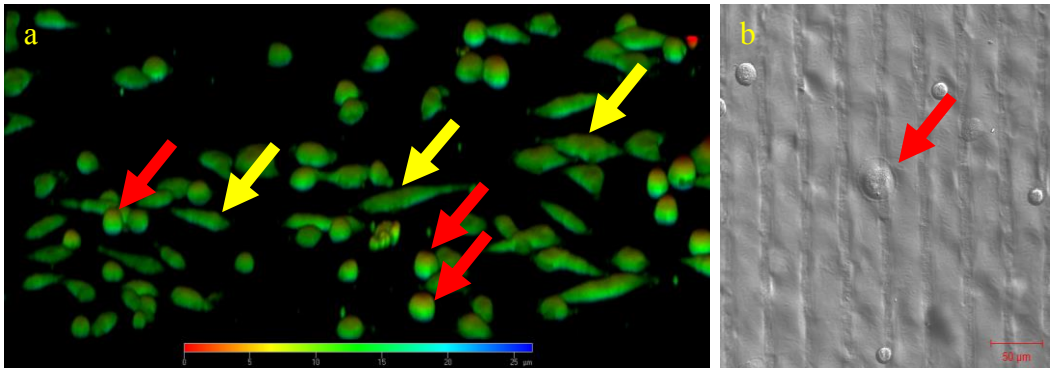

Figure 8.4 (a) Three dimensional z-stack colour coded height image at 1 hour post seeding showing rounded BAE-1 cells in the medium which appear to be loosely attached to the surface. Some cells can be seen to be flattening and elongating on the surface. The red arrows represent cells at an early stage of cell adhesion, while the yellow arrows represent those cells in the flattening stage. (b) DIC image at post 1 hour cell-seeding – the red arrow indicates a cell beginning to flatten and clearly shows the formation of lamellipodia.

In order to investigate if the differences in surface topography had differing effects on cell height, cells were cultured on the respective polymers and left for 2 hours. After 2 hours, the BAE-1 cells were stained with CellMask™ and the height of individual cells on each surface were measured using 3D confocal microscopy. Interestingly, it was found that cells growing on polyurethane 1A, which had the greatest cell retention after 2 hours, also had the lowest mean cell height (2.74µm, StEM=0.4µm), when compared to the mean height of BAE-1 cells growing on the other polyurethane substrates; 1D (3.20µm, StEM=0.5µm, $P<0.01$), 3A (3.25µm, StEM=0.37µm, $P<0.001$), 3D (3.37µm, StEM=0.57µm, $P<0.01$), and the non-textured polyurethane (3.37µm, StEM=0.6µm, $P<0.001$), respectively (Figure 8.5)

Both BAE-1 cell adhesion and cell height were found to have an inverse correlation, in that those BAE-1 cells that had the greatest to polyurethane 1A, proceeded into the flattening process more rapidly, compared to the BAE-1 cells, cells stayed rounded growing on the 1D, 3A, 3D and non-textured polyurethanes (Figure 8.5).

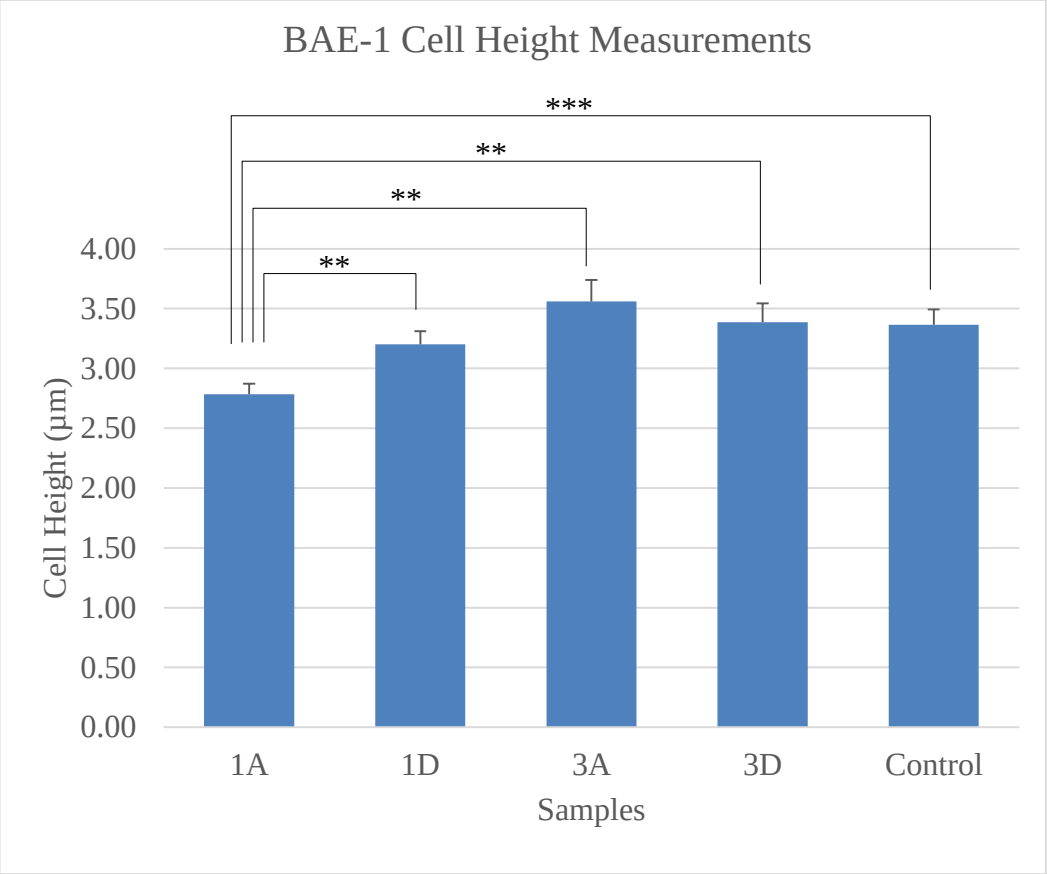

Figure 8.5 BAE-1 cell height (µm) when growing on micro-textured and non-textured polyurethanes. The mean BAE-1 cell height was significantly smaller on polyurethane 1A compared to the other substrates. Data are presented as mean (± SE); **P<0.01, ***P<0.001 (η=20).

8.3 Investigating the Effect of Indirect Laser Micro-textured and Non-textured Polyurethanes on BAE-1 Cell Proliferation Under Static Conditions

The BAE-1 adhesion assay demonstrated that polyurethane 1A accelerated cell adhesion and flattening (as evident by lowest mean cell height in µm) compared to all other polyurethane substrates. In order to determine the effects of the patterned substrates on cell proliferation, a cell proliferation assay was performed. Briefly, 10,000 cells were seeded on to the respective substrates and left to incubate for 24, 48 and 72 hours respectively. At each time point the cell number was determined using the fluorescent PrestoBlue® assay.

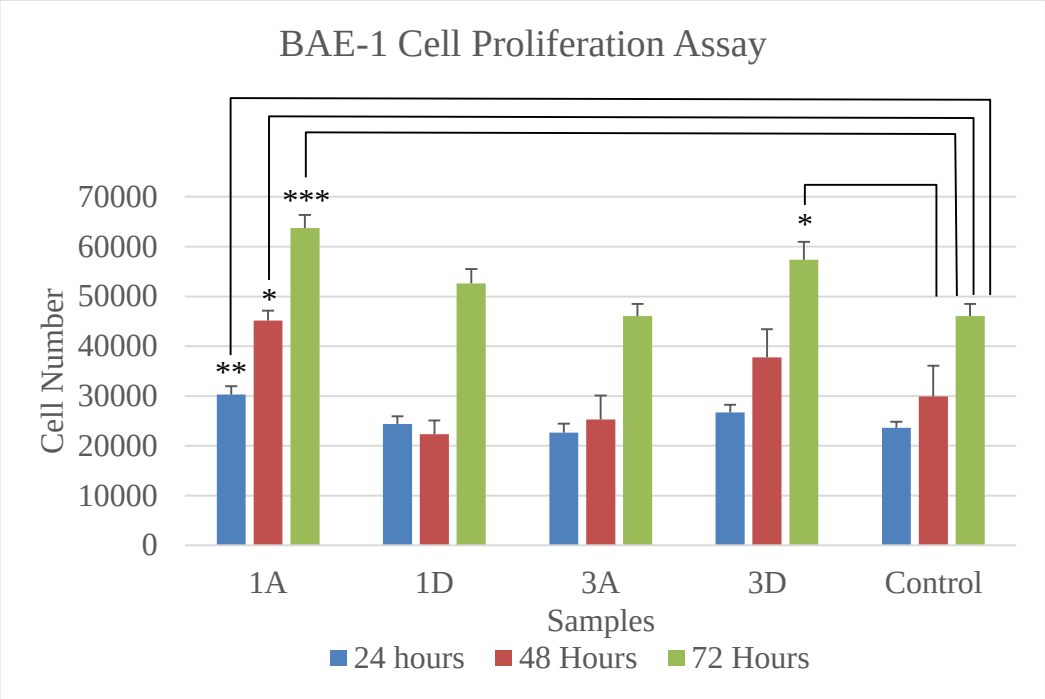

Figure 8.6 BAE-1 cell proliferation was significantly increased on polyurethane 1A compared to control for 24, 48, 72 hours. Data are presented as mean (± SE) *P<0.05; **P<0.01, ***P<0.001 (η=6).

As can be seen from Figure 8.6 the cell density on polyurethane 1A was significantly higher at 24 (P<0.01), 48 (P<0.05), and 72 (P<0.001) hours compared to the non-textured polyurethane. Interestingly, it was also found that polyurethane 3D had a greater cell density than the non-textured polyurethane at

72hours post seeding (P<0.05). There were no significant differences in cell density between 3A & 1D and the non-textured polyurethane (Figure. 8.6). These experiments were repeated and each time this basic trend was observed.

8.4 Investigating Focal Adhesion Formation and Actin Organisation of BAE-1 Cells on Indirect Laser Micro-textured and Non-textured Polyurethanes under Static Conditions

Both the BAE-1 cell adhesion and the proliferation results have demonstrated that polyurethane 1A accelerated cell adhesion and increased the cell proliferation rate compared to non-textured polyurethane. We were therefore interested to know if there was any change in the level of focal adhesion formation and actin organization, so as to further understand the how the cells are forming interactions with the surfaces. Both actin filaments and vinculin (which is a main component of the focal adhesion complex) were fluorescently labelled at 2 and 48 hours post cell seeding and imaged using confocal microscopy.

It was difficult to observe any differences in focal adhesion and actin filament organisation at 2 hours post seeding on polyurethanes 1A (Figure 8.7a), 1D (Figure 8.7b), 3A (Figure 8.7c), 3D (Figure 8.7d) and non-textured polyurethane (Figure 8.7e), because the nascent adhesion were distributed throughout the cells and the actin filaments were dendritic in organisation.

However, it was observed that after 48 hours, focal adhesion complexes had formed at a relatively high density on the microfringes of polyurethane 1A (Figure 8.8a). These focal adhesions appeared elongated and mature and seemed to be dictated by microfringe shape. Furthermore, dense actin stress fibers were also observed organized parallel to the microfringe structures and each end of the actin stress fiber terminated between two mature focal adhesions (Figure 8.8a). In contrast to focal adhesion on polyurethane 1A, the focal adhesion formation on the non-textured polyurethane appeared to be very random, rounded, and generally

smaller. Moreover, less dense actin stress fiber formation was observed with the arrangement of the actin filaments being mostly dendritic in nature (Figure 8.8e).

The most interesting observation was on polyurethane 3D, where it was observed that after 48 hours, focal adhesions were found formed in the 'microripple gap' instead of on the microripple structure. A cross-linked mesh-like actin filament arrangement was also observed, which ran parallel along the 'microripple gap and orthogonal to the microridge (Figure 8.8d). The parallel dense actin stress fibers seem confined within the microridge and terminated at the edge of the microridge (the overall length of the parallel actin stress fibers seemed to be determined by the width of the microridge). In contrast, less focal adhesions were observed on polyurethane 3A and some were found to localise in the microripple 'gap'. No cross-linked, mesh-like actin stress fiber organisation was observed along the microripple gap on polymer 3A and mostly actin splinter stress fibers were evident (Figure 8.8c). When BAE-1 cells were grown on polyurethane 1D, mostly splinter actin stress fiber and dendritic actin filaments were observed (Figure 8.8b).

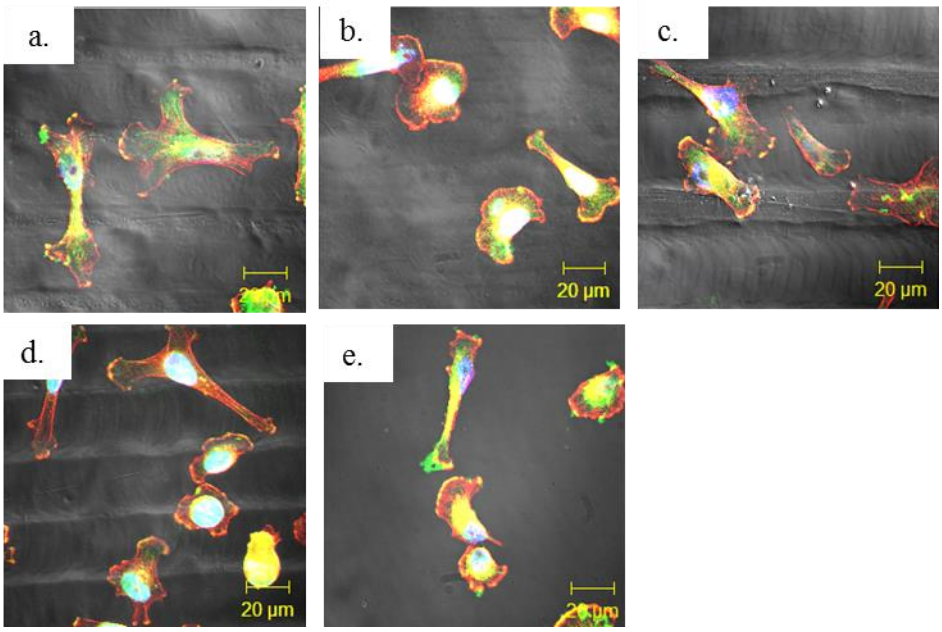

Figure 8.7 Fluorescence image of BAE-1 cells actin filaments organisation and focal adhesion formation on polyurethane (a) 1A, (b) 1D, (c) 3A, (d) 3D, and (e) control after 2 hours cell seeding. Actin red, nuclei blue and vinculin green.

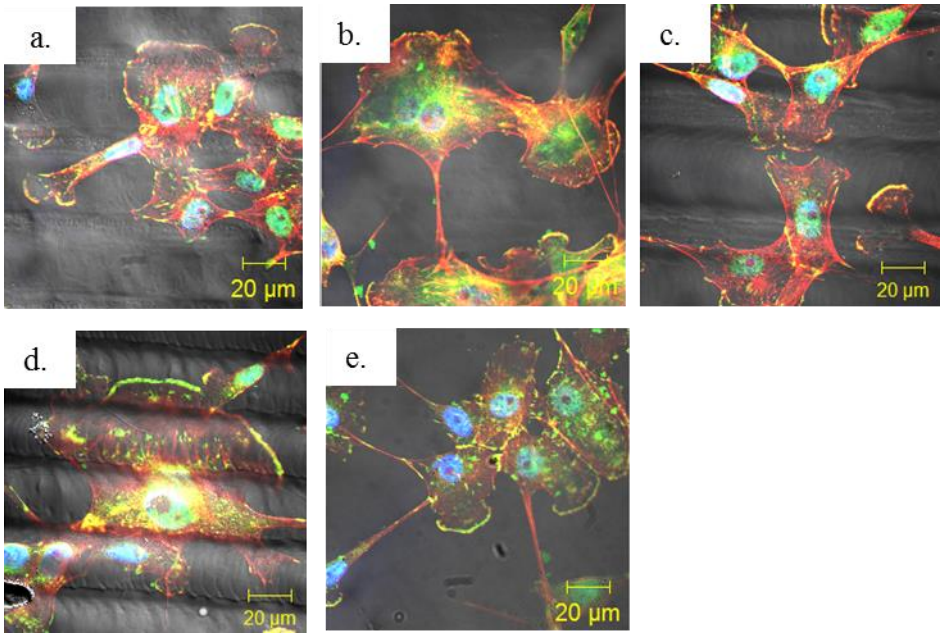

Figure 8.8 Fluorescence image of BAE-1 cells actin filaments organisation and focal adhesion formation on polyurethane (a) 1A, (b) 1D, (c) 3A, (d) 3D, and (e) control after 48 hours cell seeding. Actin red, nuclei blue and vinculin green.

8.5 Investigating BAE-1 Cell β-Actin Expression Levels on Laser Micro-textured and Non-textured Polyurethanes Under Static Conditions

The fluorescence images have shown that BAE-1 cells possessed a higher level of actin stress fibres when grown on polyurethane 1A and 3D, compared to when grown on polyurethane 1D, 3A, and the non-textured polyurethane. To determine if there were any differences in the actual expression levels of β-actin in the BAE-1 cells cultured on the respective polymers, an In-Cell ELISA assay was performed. The results of the In-Cell ELISA assay are displayed in Figure 8.17. As can be seen from Figure 8.9, BAE-1 cells growing on polyurethane 1A and 3D had significantly higher levels of β-actin compared to BAE-1 cells growing on the non-textured polyurethane (**$p \leq 0.01$). No significant differences were found when comparing polyurethanes 1D and 3A with the non-textured polyurethane.

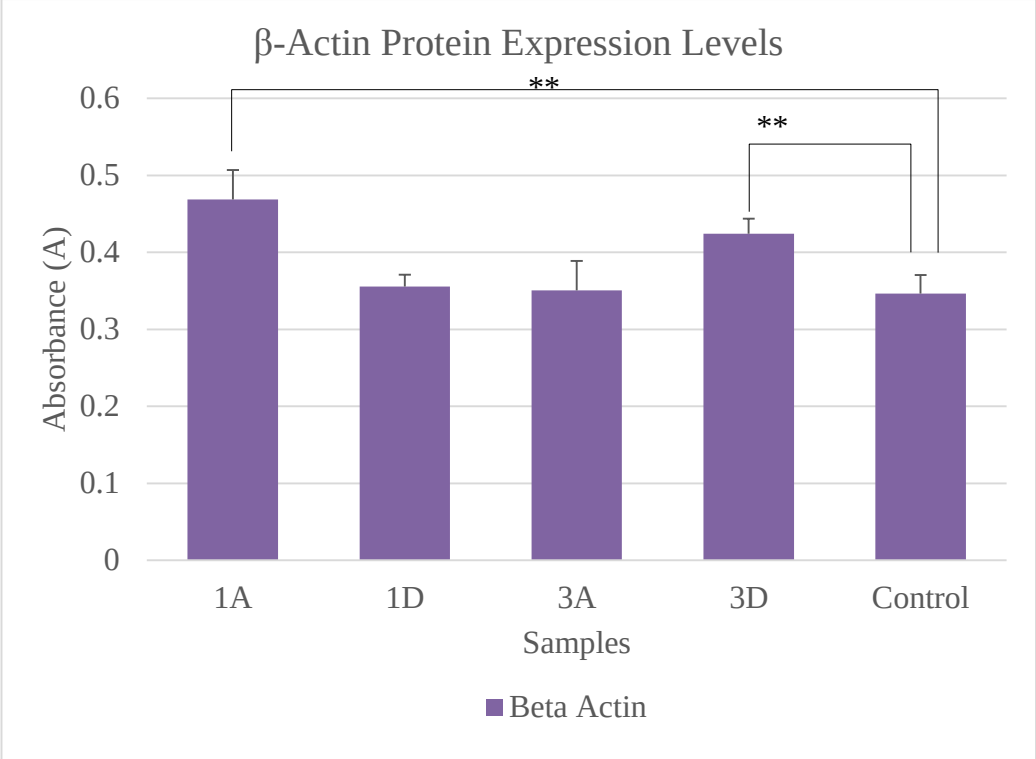

Figure 8.9 BAE-1 cells growing on polyurethane 1A and 3D had significantly increased β-actin levels compared to non-textured polyurethane. Data are presented as mean (± SE) *P<0.05; **P<0.01, ***P<0.001(η=9)

8.6 Investigating BAE-1 Cell Migration Velocity, Distance and Forward Migration Index on Indirect Laser Micro-textured and Non-textured Polyurethanes Under Static Conditions

8.6.1 BAE-1 Cell Migration Velocity and Distance

To correlate β-actin expression levels with BAE-1 cell migration velocity and distance, time-lapse microscopy was performed. This allowed post image analysis, using ImageJ, to track cell migration velocity, distance and directionality. As can be seen from Figure 8.10, BAE-1 cells growing on polyurethane 1A had the lowest mean cell velocity (0.41µm/min, SD=0.09µm/min). It was also observed that polyurethane 3D has the greatest mean cell migration velocity (0.52µm/min, SD=0.12µm/min, *P*<0.001), which was 1.4 fold greater than those cells growing

on the non-textured polyurethane. Other polyurethanes including, 1D (0.43µm/min, SD=0.08µm/min, $P<0.05$), and 3A (0.45µm/min, SD=0.11µm/min, $P<0.05$) also increased the mean cell migration velocity compared to non-textured polyurethane. Surprisingly, no significant difference in mean cell velocity was found for BAE-1 cells growing on polyurethane 1A compared to non-textured polyurethane, even though this polymer was shown to have the greatest actin expression levels. It was observed that the deeper microripple gap depth on polyurethane 3D (compared to polyurethane 3A) increases in mean cell migration velocity. On the other hand, polyurethane 1A with a microfringe structure smaller than the microripple structure decreased mean cell velocity.

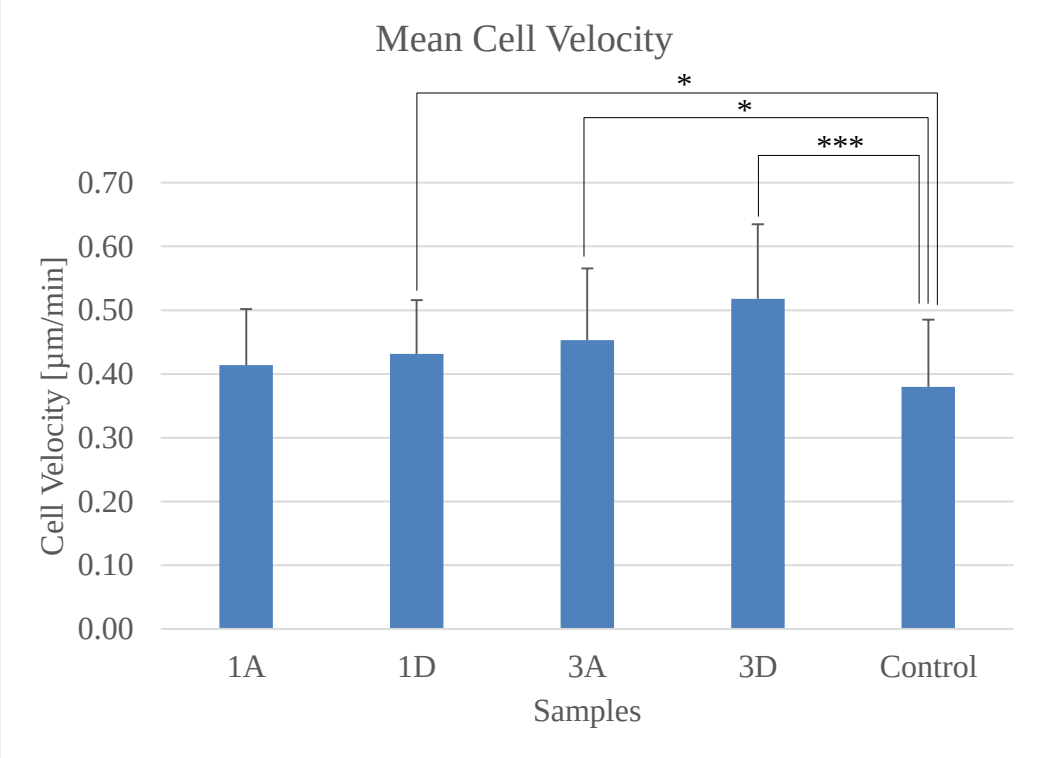

Figure 8.10 Migration velocity of BAE-1 cells cultured on laser micro-textured and non-textured polyurethanes. The results show that mean BAE-1 cell velocity was significantly higher on polyurethane 1D ($P<0.05$), 3A ($P<0.05$), and 3D ($P<0.05$) compared to the non-textured polyurethane. The results also show that 3D had the greatest mean cell velocity overall. Data are presented as mean ± SD, *P<0.05; **P<0.01, ***P<0.001 and η=30.

In addition, it was also observed that the substrate that promoted the highest mean cell migration velocity also had the highest mean accumulated distance. Cells

grown on polyurethane 3D, which had the greatest mean cell migration velocity, also has the highest mean accumulated distance (367µm, SD=83µm). While cells growing on polyurethane 1A, which had the lowest mean cell migration velocity, also had the lowest mean accumulated distance (292µm, SD=61µm). For the other polyurethane substrates the mean cell accumulated distance was 1D (306µm, SD=56µm), 3A (323µm, SD=79µm) and non-textured polyurethane (266µm, SD=73µm). These results suggest that cell migration distance is dependent upon the mean cell migration velocity.

8.6.2 BAE-1 Cell Forward Migration Index

In order to investigate the effect of surface topography on cell migration, the cell forward migration index (FMI) was used. The FMI represent the efficiency of cell migration in relation to the x_{FMI} (migration parallel to microfringes or microripple structures) and y_{FMI} (migration perpendicular to the microfringes or microripple structures) axis. The position and negative FMI indicates the cell migration frequency to a particular direction. For example, an increase in positive or negative FMI index indicates that there is an increase in number of cells within the population are migrating in that direction (migrating either parallel to the microripple/microfringes or to the microridges).

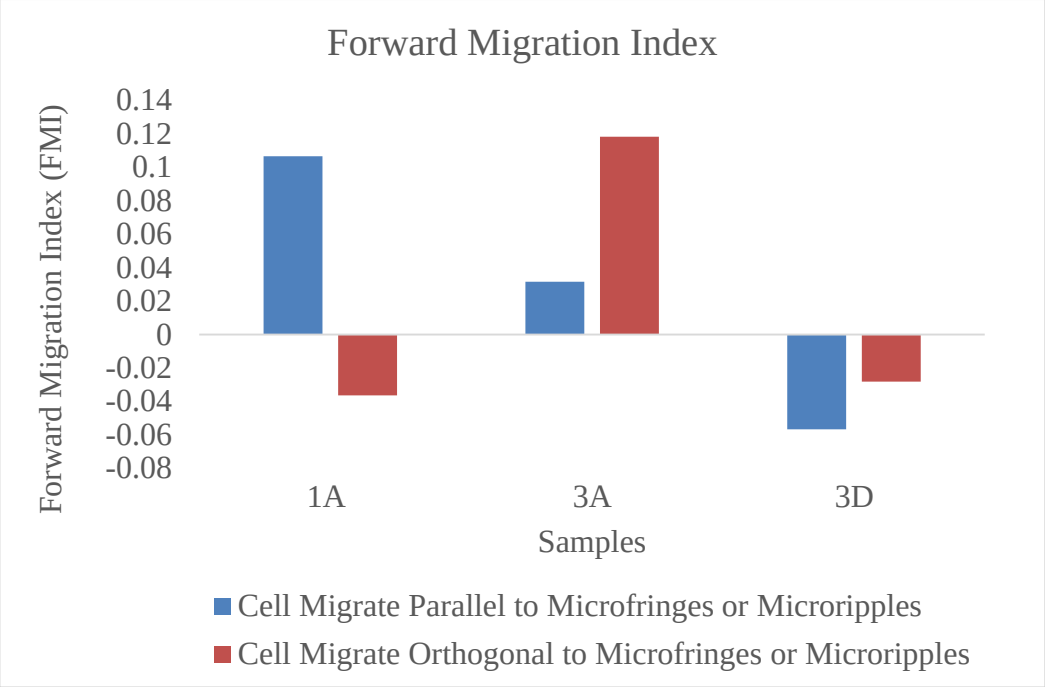

Figure 8.11 The forward migration index (FMI) of BAE-1 cells on all laser micro-textured polyurethanes

As can be seen in Figure 8.11, it was observed that, polyurethane for 1A, more BAE-1 cells preferentially migrated parallel to the microfringes (FMI=0.11) compared to those migrated perpendicular to the microfringes (FMI=-0.04). Interestingly, it was found that BAE-1 cells preferentially migrated orthogonal to the microripple structures on polyurethane 3A (FMI=0.12). Polyurethane 3D, which has a deeper microripple gap and more microripple structures, seemed to direct the cells to migrate parallel to the microripples (FMI=-0.05). In contrast to cell migration on polyurethane 1A, it was found that the BAE-1 cells migrated parallel to the microridge structures on polyurethane 1D. Interestingly, these microridges do not contain microfringes, or microripple structures (FMI=0.13).

FMI is used to analyse the effect of surface topography on cell migration. Therefore FMI analysis is not relevant for the non-textured polyurethane and thus was not included in these results.

Time-lapse imaging was also performed to compare with the results of the FMI data. With respect with the microfringes on polyurethane 1A, it was observed that numerous cells migrated parallel along the microridge, but were observed to change migration direction when encountering the microfringe structures. This is

highlighted in Figure 8.12, which shows that when the cells encounter the microfringe structures (Figure 8.12a) the migration direction changes and the cells are observed to elongate parallel to the microfringe structures (Figure 8.12c). Ultimately, the cells were found to switch direction and migrate perpendicular to the microridge (Figure 8.12d). This was a common occurrence for many cells growing on polyurethane on this substrate.

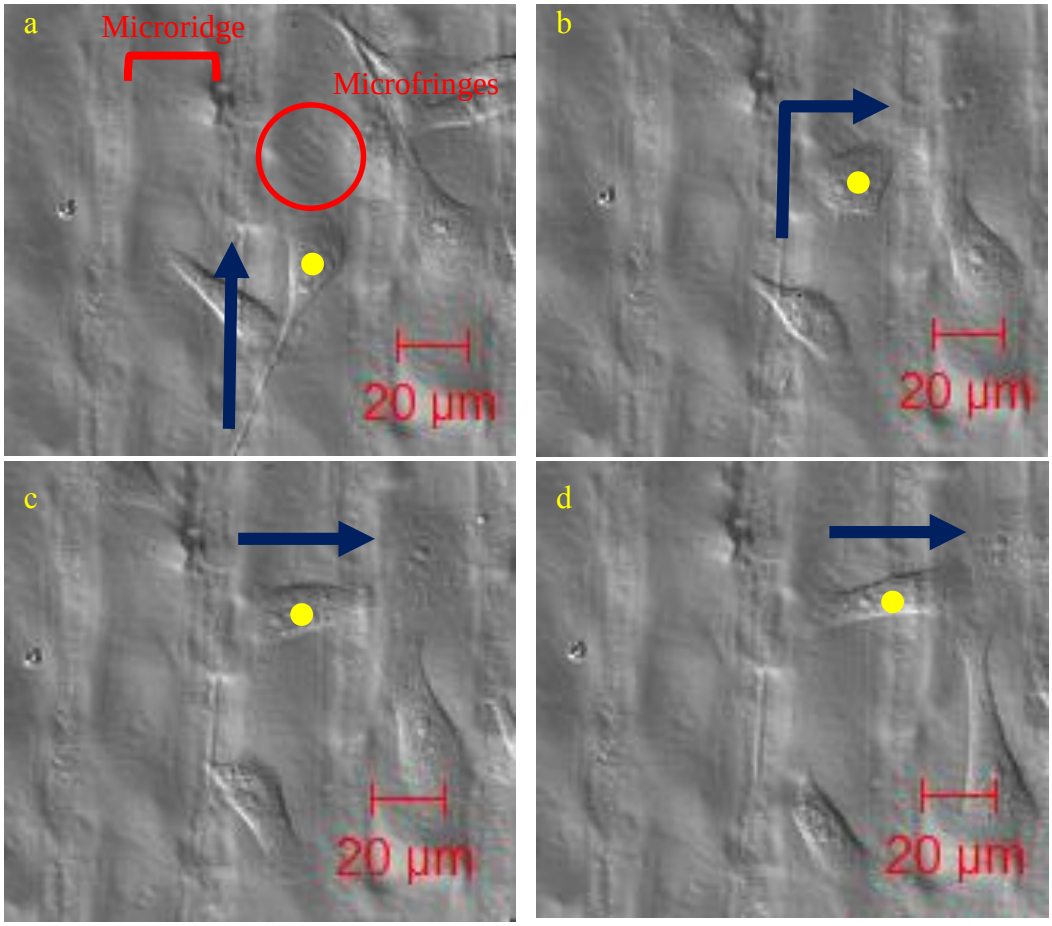

Figure 8.12 Time-lapse imaging showing the migration direction of a BAE-1 cell (yellow dot). The red circle highlights the microfringe structures. The blue arrow shows the BAE-1 cell migration direction. (a-b) cell migrates along the microridge toward the microfringe structures. (c-d) cell elongates parallel to the microfringes and changes its migration direction, which is now parallel to the microfringe structures. Only 1 cell is highlighted here, however this behaviour was a common occurrence.

In contrast to the migration behaviour observed on polyurethane 1A, it was observed that the microripple structures on polyurethane 3D had a similar effect on cell migration. It was observed that the cells either migrated along the channels, between the two microridges, or migrated parallel to the microripples (Figure 8.13).

Compared to polyurethane 3A, it was observed that less cells migrated parallel to the microripple structure and most of the cells migrated perpendicular to the microripples.

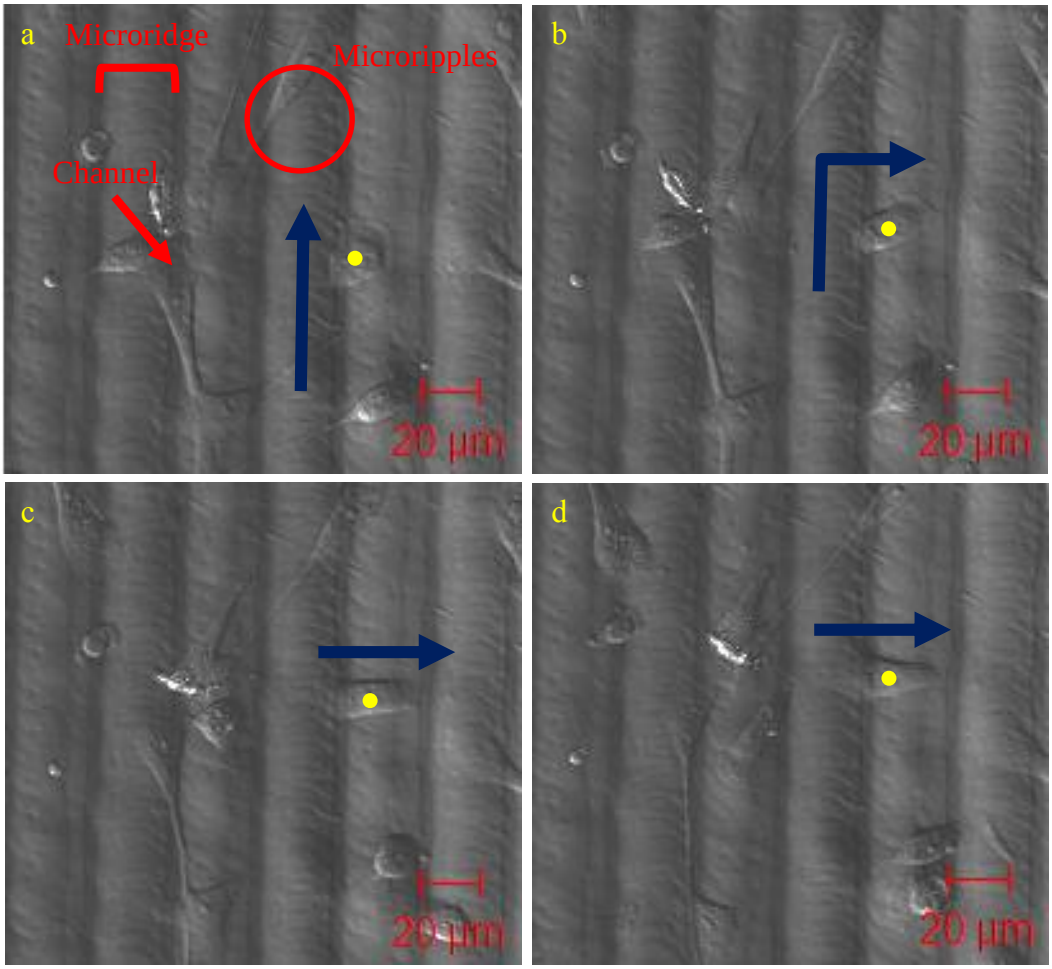

Figure 8.13 Time-lapse images showing a migrating BAE-1 cell (yellow dot). The red circle highlights the microripple structures. The blue arrow shows the BAE-1 cell migration direction. (a) cell migrates along the channel. (b-d) cell elongates parallel to the microripples and changes its migration direction parallel to the microripple structure. Only 1 cell is highlighted here however this behaviour was a common occurrence.

These results suggest that the microfringe structures on polyurethane 1A control cell migration direction parallel to the microfringe structures. In contrast to polyurethane 3A, the microripple gap on polyurethane 3D was deeper and seemed to direct more cells to migrate parallel to the microripple structures. Polyurethane 3A, with a shallower microripple gap, was found to have relatively less cells

migrating parallel to the microripple structure, even though the width dimension of the microripples was roughly similar to that of polyurethane 3D (polyurethane 3A =6.23±1.26µm, and polyurethane 3D=6.27±0.82µm). These results suggest that the microripple gap depth has a greater effect on BAE-1 cell migration than the microripple width.

8.7 Investigating Cell Morphology, Focal Adhesion Formation and Actin Organisation of BAE-1 Cells on Indirect Laser Micro-textured and Non-textured Polyurethanes Under Flow Conditions

The above experiments were all carried out under static conditions, in that the BAE-1 endothelial cells were not subjected to any shear force during the experiments. *In vivo* endothelial cells would be subjected to shear force, generated by blood flow through the vascular system. Therefore, some of the above experiments were carried out with the BAE-1 cells exposed to a physiological shear stress level of 20dyne/cm^2 over a 24hr period, in order to try and mimic *in vivo* stress conditions.

8.7.1 BAE-1 Cell Morphology

With respect to cell morphology, it was observed that only a few cells elongated in morphology when grown on polyurethane 1A, 1D, 3A, 3D and the non-textured polyurethane, with most of the BAE-1 cells appearing to be rounded in morphology under physiological shear stress level of 20dyne/cm^2 for 24 hours (Figure 8.14a-8.14e).

8.7.2 BAE-1 Cell Focal Adhesion and Actin Organisation

It was observed that, after 24 hours, BAE-1 cells growing on all micro-textured and non-textured polyurethane displayed a high level of actin stress fibers compared to the BAE-1 cells under static conditions, which had less actin stress fibers. Moreover, the nuclei were found to remain rounded and located in the centre of the cells when under flow. Also, the BAE-1 cells exposed to shear stress, grown on polyurethanes 3A and 3D, displayed a much denser actin organisation, with actin stress fibers aligning parallel along the microripple gap. The actin stress fibers were also found to be confined to the width of the microgroove (polyurethane 3A) or microridge (polyurethane 3D) (Figures 8.14c and 8.14d). The focal adhesions were mainly observed to be elongated along the microripple gap. A simplified schematic diagram in Figure 8.15a illustrates actin organisation, confinement and the formation of focal adhesion on polyurethanes 3A and 3D under flow conditions.

Surprisingly, focal adhesions do not appear on the microfringes on polyurethane 1A under flow conditions. Also, the focal adhesions appear less elongated and appear to be greater in number and randomly orientated. Shorter, splinter-like, actin filaments are also observed under flow conditions (Figure 8.14a) compared to static conditions (see Figure 8.8 in Section 8.4). For the non-textured polyurethane, BAE-1 cells appear to possess smaller and fewer focal adhesion complexes, when compared to all the micro-textured polyurethanes. It was also observed on non-textured polyurethane that the actin filaments were in a dendritic organisation and were less dense (Figure 8.14e). A simplified schematic diagram (Figure 8.15b) illustrates the actin organisation and the formation focal adhesions on polyurethane 1A and non-textured polyurethane.

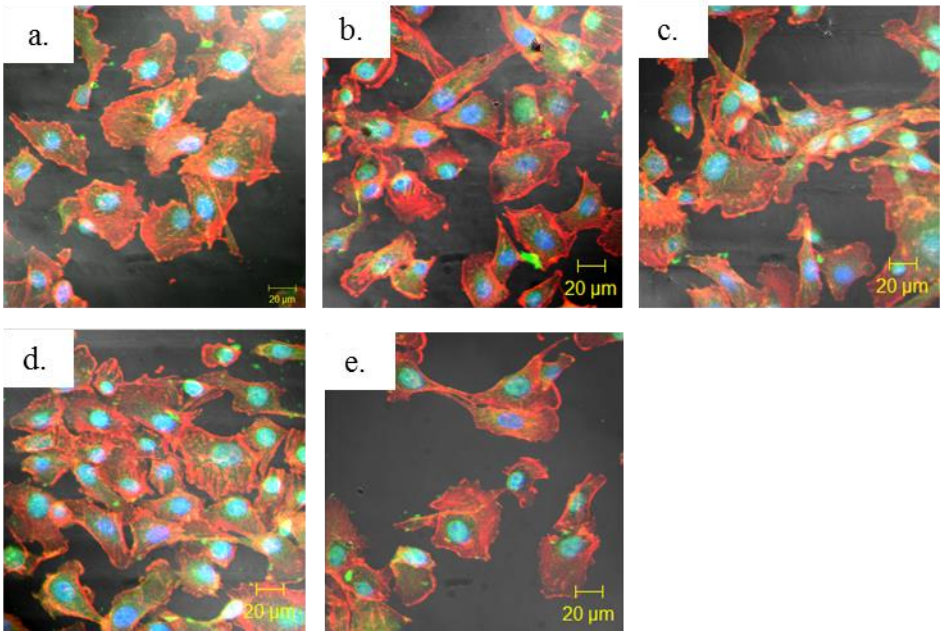

Figure 8.14 Fluorescence image of BAE-1 cells actin filaments organisation and focal adhesion formation on polyurethane (a) 1A, (b) 1D, (c) 3A, (d) 3D, and (e) control after 24 hours of applied shear stress (20dyn/cm^2). Actin-red, nuclei-blue, vinculin-green.

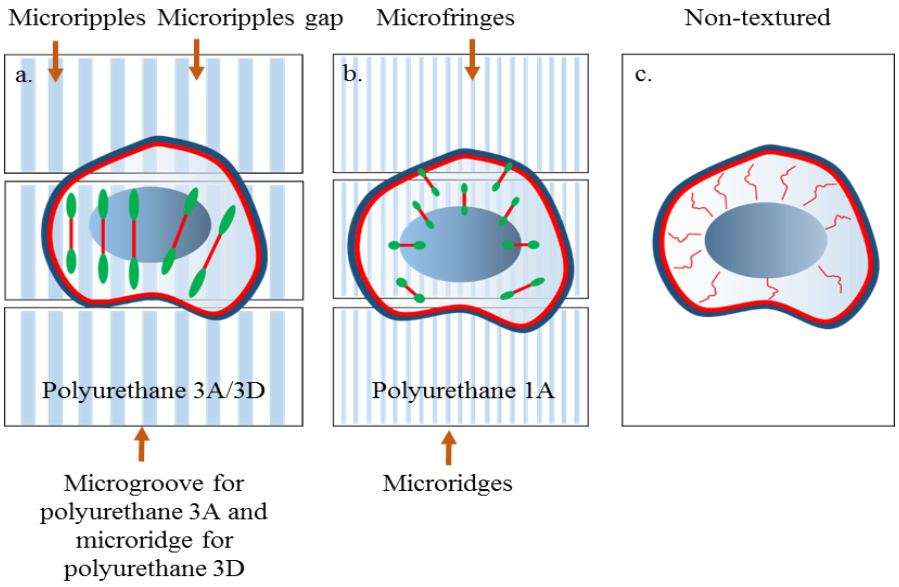

Figure 8.15 The schematic diagram shows focal adhesion and actin organisation on polyurethane 1A, 3A, 3D and on non-textured polyurethane under flow conditions. (a) Focal adhesions tend to be formed and confined within the microripple gap (Polyurethanes 3A or 3D). (b) The focal adhesions were randomly formed and shorter splinter-like actin stress fibers were observed on the microfringe structures. (c) The focal adhesions were smaller and actin filament organisation was dendritic in nature (non-textured polyurethane).

8.8 Standard Curve Generation for the HCASMCs Adhesion and Proliferation Assay

For the adhesion and proliferation assays on human coronary smooth muscle cells (HCAMSCs) the MTT assay was used. This was because the fluorescence plate reader was not available for the Presto blue assay. However, earlier work comparing the sensitivity of the MTT and PrestoBlue® assays was found to provide consistent results. Before performing the cell adhesion and proliferation assays, an MTT calibration curve was generated for HCASMCs cell number versus absorbance. As described earlier in Section 8.1, a serial dilution was performed by serially diluting 100,000 cells to 96 cells. These cells were then seeded into the wells of a 96 well plate and the MTT assay was carried out immediately. The results showed a linear correlation between absorbance and absolute cell number (Figure 8.16).

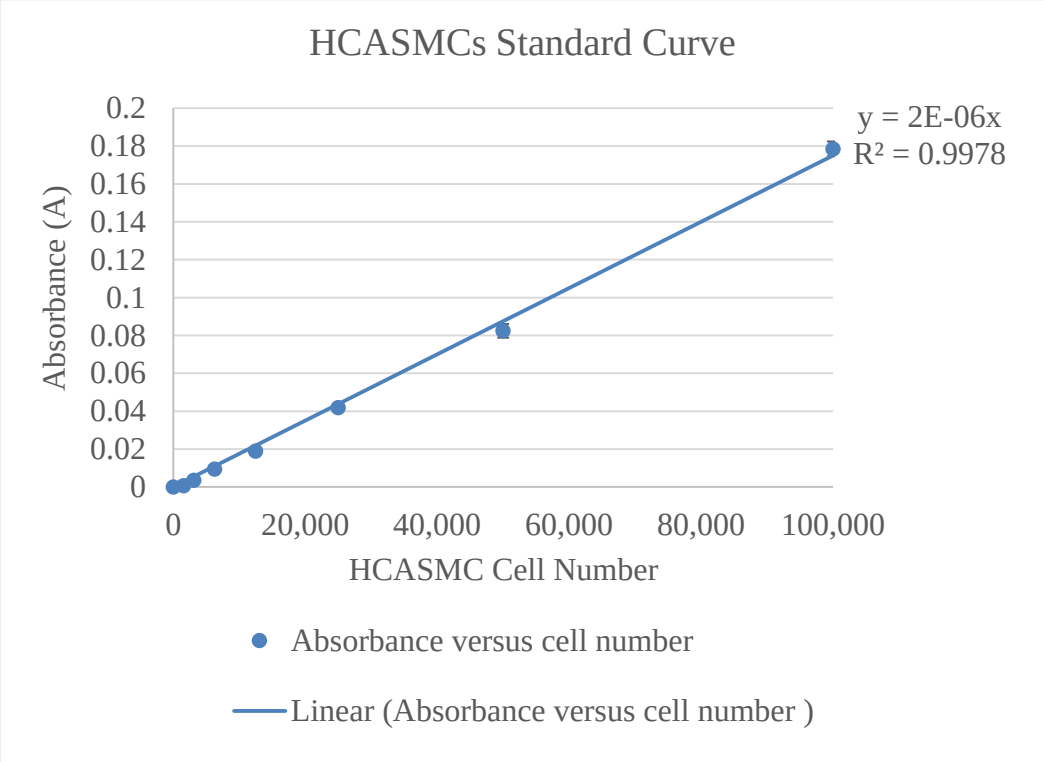

Figure 8.16 Standard curve generated by obtaining the fluorescent signal emitted from HCASMC cells treated with MTT dye. A linear correction was found between absorbance and absolute cell number.

8.9 Investigating the effect of Indirect Laser Micro-textured and Non-textured Polyurethanes on HCASMCs Adhesion under Static Conditions

For investigating cell adhesion the same assay procedure was used to analyse HCASMCs retention, except the PrestoBlue® assay was replaced with the MTT assay. Each substrate was seeded with a cell density of 10,000 cells. After 2 hours post seeding the MTT assay was carried out (Note that, the MTT assay reaction required 4 hours to take place after adding the MTT solution). The results showed that no HCASMCs had attached to polyurethanes 1A, 1D, 3A, 3D, and to the non-textured polyurethane. To confirm these results the assay was carried out a number of times and each time the results were repeatable.

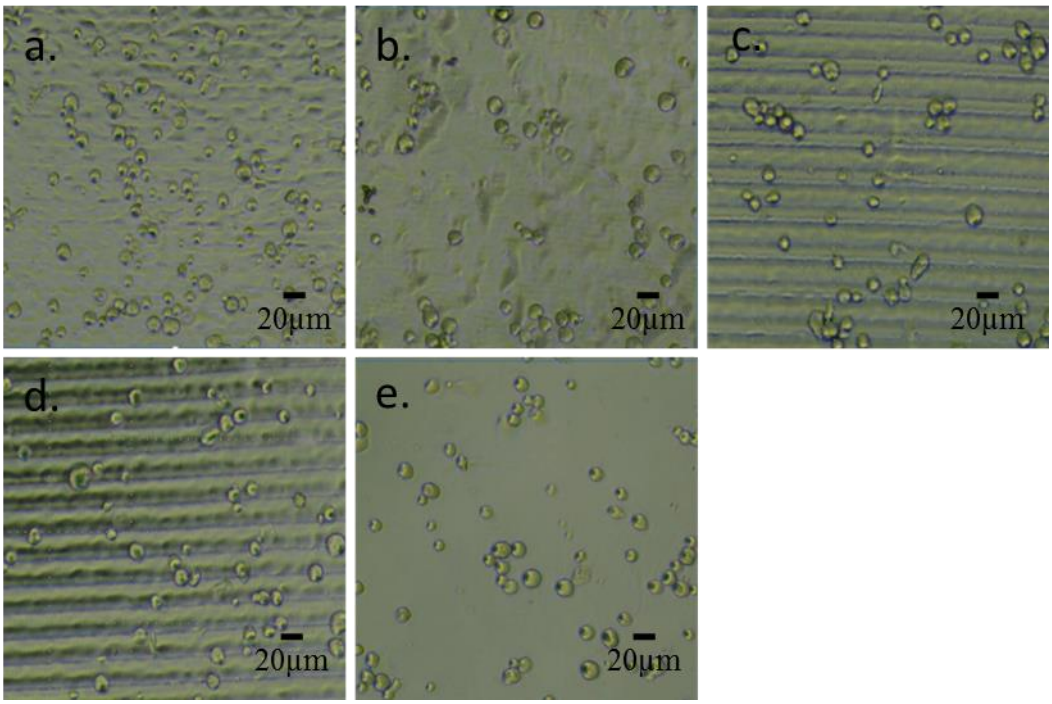

Figure 8.17 Phase contrast images show the HCASMCs to be rounded in morphology and not spread on the micro-textured and non-textured polyurethanes, 2 hours post seeding. (a) Polyurethane 1A, (b) Polyurethane 1D, (c) Polyurethane 3A, (d) Polyurethane 3D, and (e) Non-textured polyurethane.

Real time, phase contrast microscopy, was also carried out at 2 hours post seeding to capture images of HCASMCs on the polyurethanes. As can be seen from Figure

8.17, the microscopy images revealed that the HCASMCs remained in a rounded morphology and were suspended in the medium. No adhered cells were observed on either the micro-textured, or non-textured polyurethanes. Again these experiments were repeated a number of times and in each case the results were consistent. This suggests that the Z1A1 polyurethane has properties that delayed HCASMC adhesion. However, at present the actual mechanism is not clear.

8.10 Investigating the Effect of Indirect Laser Micro-textured and Non-textured Polyurethanes on HCASMC Proliferation Under Static Conditions

In order to investigate HCASMC proliferation on the polyurethane substrates proliferation assays were carried out. As with the BAE-1 proliferation assay the HCASMC proliferation assay was carried out at 24, 48, and 72 hour intervals post seeding. Statistical analysis revealed no significant difference between the micro-textured polymers and the control (Figure 8.18). In contrast to BAE-1 cell proliferation on non-textured polyurethane at 72 hours post seeding, it was observed that the HCASMC proliferation levels were approximately 2.8-fold higher. These results suggest that the normal HCASMC proliferation rate was faster than that of BAE-1 cell proliferation, even on non-textured polyurethane. Moreover, the micro-textured surfaces were found not to enhance, or supress, HCASMC proliferation.

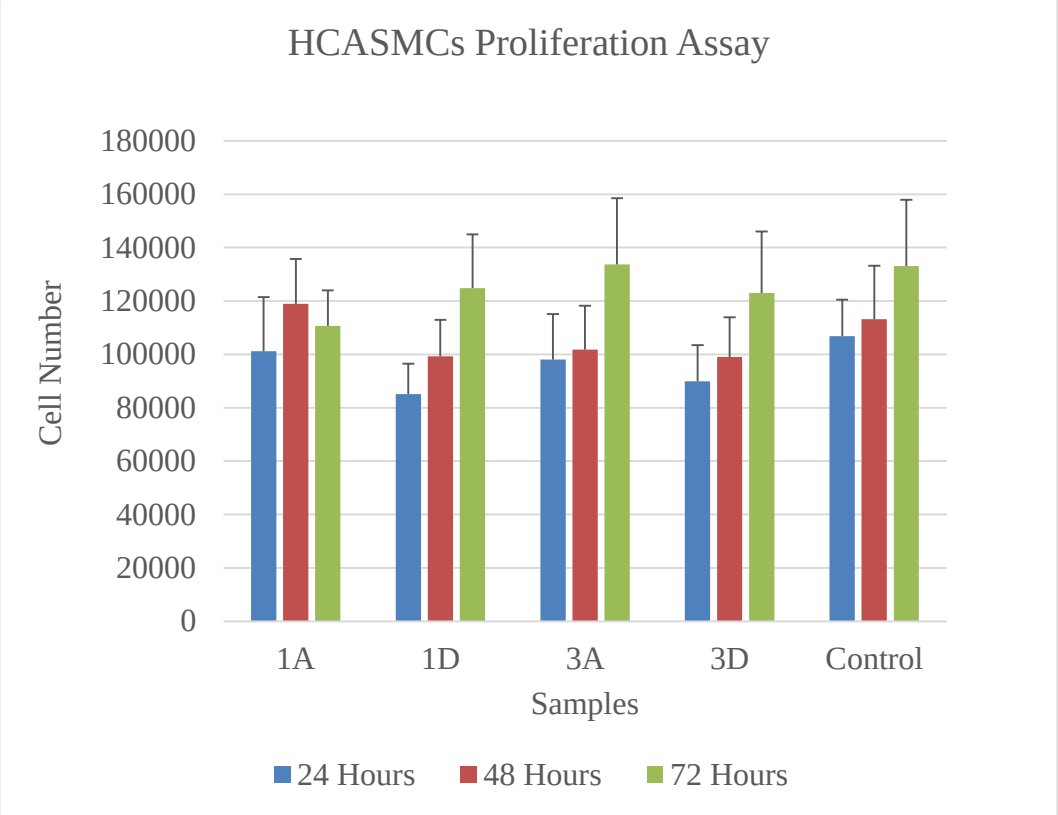

Figure 8.18 No significant differences were found in HCASMC proliferation by comparing micro-textured polyurethane with non-textured polyurethane for 24, 48, 72 hours.

8.11 Investigating Actin Organisation of HCASMC on Indirect Laser Micro-textured Polyurethane under Static Conditions

In contrast to BAE-1 actin organisation on polyurethanes 1A, 1D, 3A, and 3D, it was observed that the HCASMCs actin filaments aligned parallel to the microridges on polyurethane 1A, 3A and 3D, instead of the microfringes or microripples (Figures 8.19, 8.21 and 8.22). No actin filaments were seen to align along the microridges on polyurethane 1D and non-textured polyurethane (figures 8.20 and 8.23). Overall, the results suggest that the microridge height is the major factor influence on actin filament alignment.

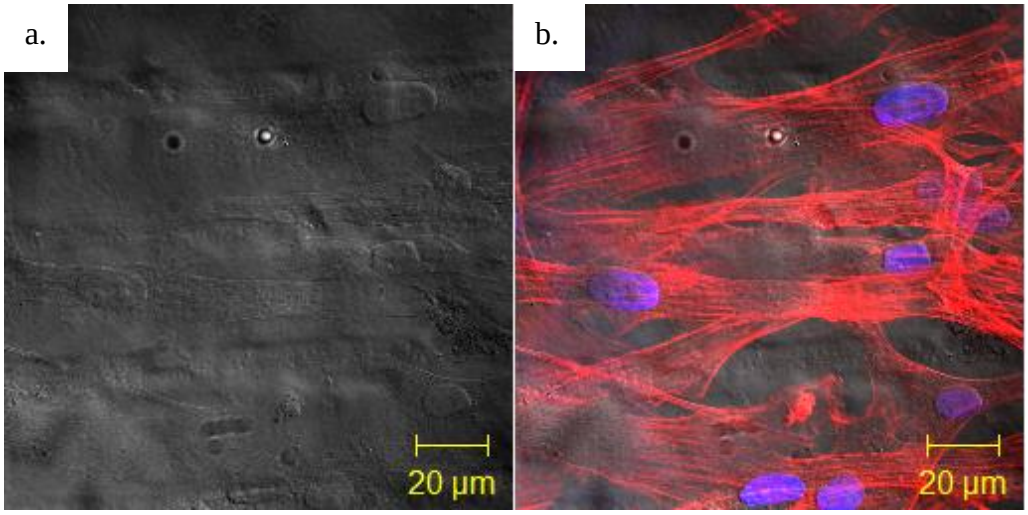

Figure 8.19 Fluorescence images of BAE-1 cells actin filament organisation after 24 hours post seeding. (a) Polyurethane 1A micro-textured surface. (b) The actin filaments were stained in red and nuclei in blue.

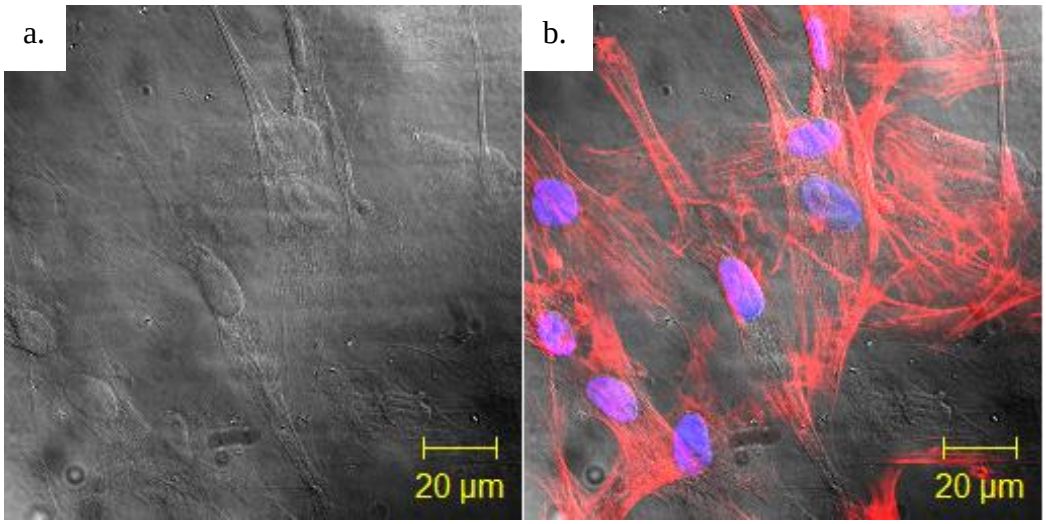

Figure 8.20 Fluorescence images of BAE-1 cells actin filament organisation after 24 hours post seeding. Actin red and nuclei blue. (a) Polyurethane 1D micro-textured surface. (b) The actin filaments were stained in red and nuclei in blue.

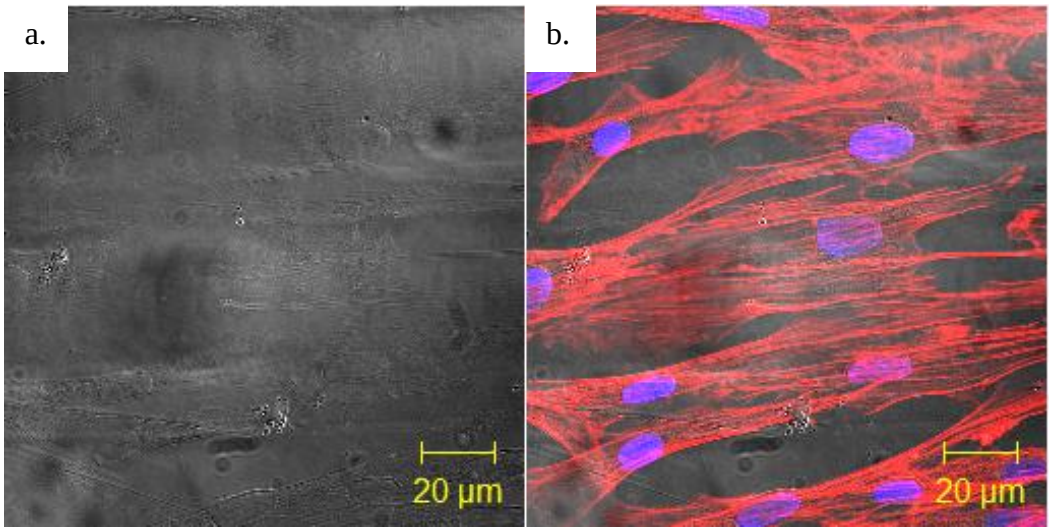

Figure 8.21 Fluorescence images of BAE-1 cells actin filament organisation after 24 hours post seeding. (a) Polyurethane 3A micro-textured surface. (b) The actin filaments were stained in red and nuclei in blue.

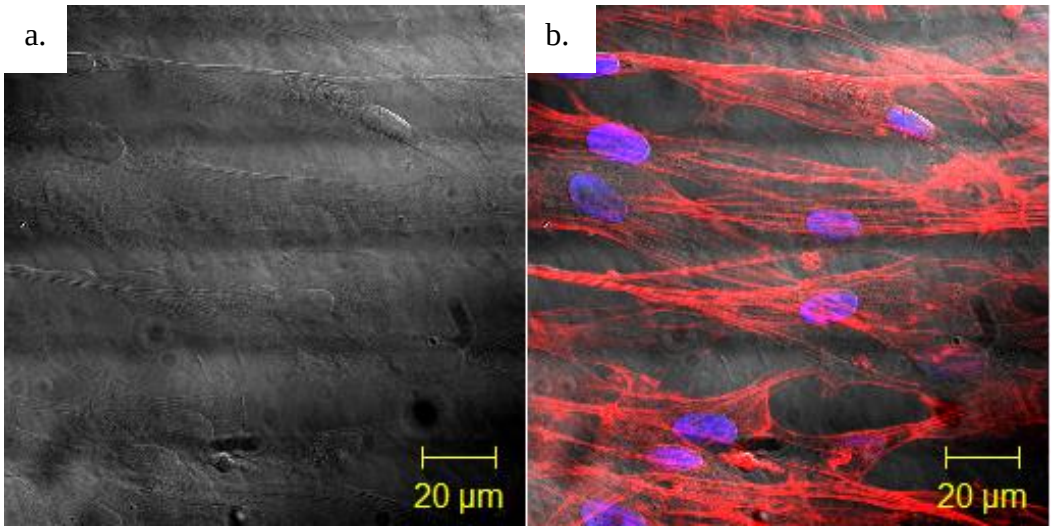

Figure 8.22 Fluorescence image of BAE-1 cells actin filament organisation after 24 hours post seeding. (a) Polyurethane 3D micro-textured surface. (b) The actin filaments were stained in red and nuclei in blue.

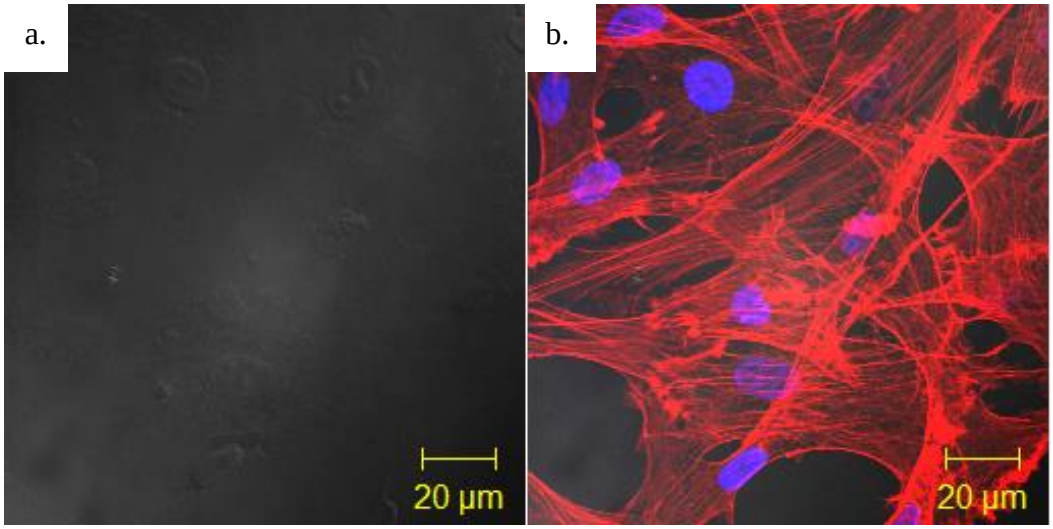

Figure 8.23 Fluorescence images of BAE-1 cells on non-textured actin filament organisation after 24 hours post seeding. (a) Control surface. (b) The actin filaments were stained in red and nuclei in blue.

Chapter 9

9.0 Discussion

9.1 Investigating the Laser Beam Spot in a Single Hatching Line

The aim of this work is to produce a laser microfabricated topography that enhances re-endothelization and inhibits smooth muscle cell adhesion and proliferation. If this is possible then it would lead to advanced biomedical implant surfaces and an application in the production of novel stent technology, and as a consequence, there would be a reduced risk of restenosis. In the initial experiments, it was observed that a single hatching line micro-textured on stainless steel at a laser scanning speed of 1800mm/s with an average power of 15W, repetition rate of 25 KHz, and pulse duration of 200ns generated a structure with an elevated rim (see figure 7.1 in chapter 7). A further decrease in the laser scanning speed to 800mm/s generated an overlapping beam spot with a less uniform elevated rim.

The results indicated that the microfringe and microripple textures may be produced through thermal ablation processes, which deposited heat into the stainless steel surface leading to heat conduction into the bulk of the material, melting, then melt expulsion, vaporization and the generation of recoil pressure, during vapour expansion. The elevated rim may be generated by laser induced vaporization recoil pressure which forces the melt out from the laser interaction zone (Semak and Matsunawa, 2014). The schematic diagram shown in figure 9.1 illustrates the laser melt expulsion process during the laser interaction with the metal surface.

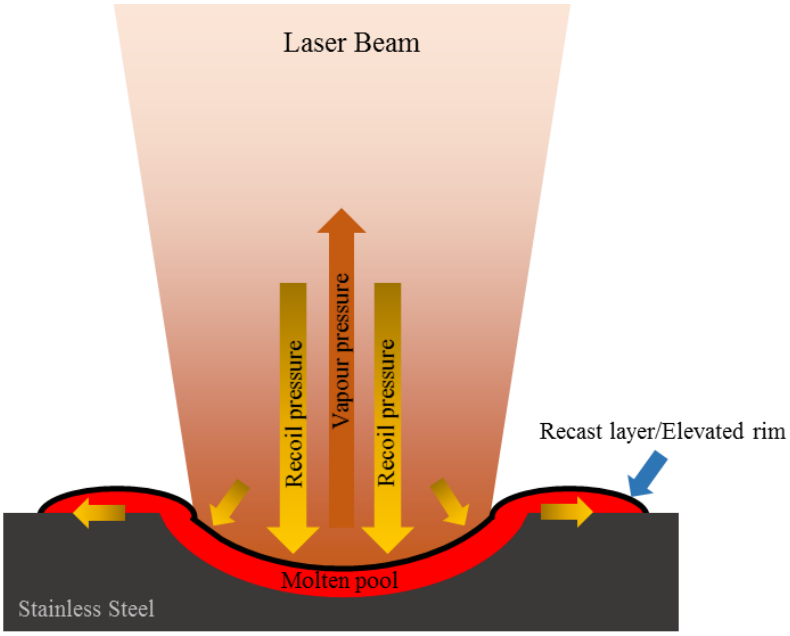

Figure 9.1 Schematic diagram illustrating the laser melt expulsion process during laser surface interaction. The red arrow showing the vapour pressure and the yellow arrow showing the recoil pressure.

9.2 Optimization of Direct Laser Microfringes Microfabrication

Laser parameter set 1 with a laser fluence of 0.03mJ/cm^2 was used in the initial experiments to generate a microfringe topography on a stainless steel surface. However, no microfringes were observed. However a slight melt expulsion, was observed where the molten material was partially expelled by a weak recoil pressure and re-solidified into an irregular recast rim around the laser spot interaction zone. The result suggested that the laser fluence wasn't high enough to generate a full regular rim around the laser spot interaction area and only a partial melt was formed, which was expelled as a molten recast layer causing irregularity in topography on the laser processed area.

The formation of the regular microridge feature, along the edge of laser processed area on the stainless steel surface, was due to the accumulation of re-solidified partially expelled molten material, called recast, which was remodelled after 25 laser scanning passes. Moreover, the formation of a regular microridge feature

associated with overlaid recast elevated rim was formed by repeatedly melting and recodify process during laser surface interaction.

A further increase in the number of passes to 25 did not show any improvement on microfringe formation, but did increase the amount of metal melt on the surface and the formation of large amount of solidified recast in the laser processed area. The result further indicated that the laser fluence was not high enough to generate a full melt expulsion through the formation of vapour pressure (see Figure 9.1). The microfringe structures were only successfully formed on the stainless steel surface by increasing the laser fluence to 0.06mJ/cm^2 and the number of laser beam scanning passes to 25. Increasing the laser fluence had successfully generated microfringes, however the results indicated that the generation of smaller microfringe structures by decreasing the overlap between two adjacent laser beam spots would be challenging. It is because further increasing laser fluence would produce a recast rim wider than the spacing width between two laser scanning spot.

The microfringe structure is sensitive to heat deposition. Failure to form microfringes may be due to slow heat dissipation and high thermal input in a small laser beam overlapping ratio. As a result, the laser processed surface is associated with other irregular features, such as hole formation, or round protruded domes formed from solidified stainless steel melt. It is suggested that small laser beam overlapping ratio, slow heat dissipation, and heat accumulation over time all lead to maintaining the molten liquid state for the first laser beam process. Then the second incoming beam overlaps the first beam processed spot, distorting the integrity of the first molten pool.

A different laser machining strategy was used to produce a smaller width microfringe feature by reducing the hatch spacing until two of the adjacent laser processing tracks overlapped each other. It was hoped that only half of the previous machined tracks would be over written by the new machining strategy. However this was not the case, and instead we observed that the second laser hatching track destroyed the previous microfringe structure due to the thermal input into the stainless steel substrate. Figure 9.2 shows the new micro textured track structure. It was observed that the second laser track does not overwrite half of the previous track, as was expected, with a new microfringe structure, but instead damages all

the previously formed microfringes, by melt formation and remodelling of the metal surface into a wavy uneven structure when the liquid molten metal solidifies. Therefore, a wavy surface topography without microfringes (polyurethane 1D) was generated and this used as a comparison sample to investigate the effect of microfringes features on BAE-1 cells.

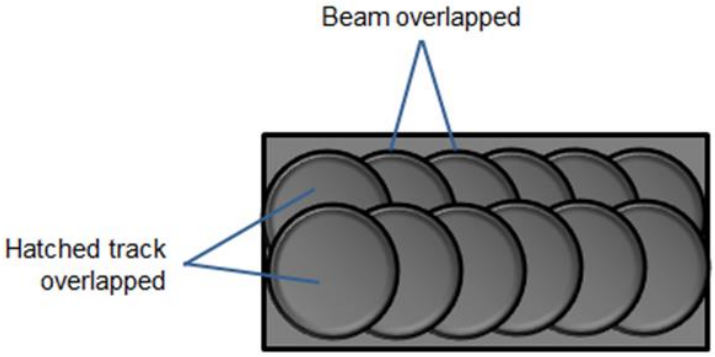

Figure 9.2 The schematic diagram illustrates show the microfringes were formed by laser beam overlapping and produced smaller width microfringes by hatch track overlapping.

9.3 Optimization of Direct Laser Microripple Microfabrication

In the previous section, it was observed, that a small focused laser beam spot diameter, overlapping with the previous track would generate high amounts of heat deposition on the laser processed area, which leads to the surface being remodelled into irregular wavy surface topography. Therefore, a larger laser beam overlapping parameter was investigated in an attempt to generate a microripple feature without the associated destruction through heat conduction into the surface. For the first set of experiments, a laser fluence of 0.003J/cm^2 was applied, which did not produce any ablation on the surface at all. This may be due to a low laser fluence, which was not high enough to initiate the melt expulsion process. Increasing the laser fluence to 0.005J/cm^2 was successful in generating microripple features that span the breadth of the microgroove. At the same time a microridge was generated along the side of microripples due to liquid melt re-solidification.

However, a further increase in the number of laser scanning passes, using the same laser fluence, produced a larger recast microridge and a narrowing of the width of the microgroove, which consisted of the microripple feature. A further increased in the laser scanning pass number did not increase the levels of melt expulsion but only removed material in every repeated single pass. However, the deeper the microgroove, the higher and wider were the microridges which formed. This was due to the Gaussian beam profile (beam shape) and consolidation of the overlaid recast rim.

Further increase in laser fluence led to the expulsion of a large amount of molten material and the formation of a thicker re-solidified rim around the laser spot interaction zone. The thicker ring dimension was greater than the spacing between the overlapping laser beam spot diameters which in turn led to a reunion and remodelling of the stainless steels surface into an uneven, or flat, surface topography. With this current laser system set-up, the result has shown that this techniques has reached its limitation in producing smaller, or deeper structures, such as the microripples. This is because in order to increase the depth of the microfringes, or microripples, then the laser fluence must be increased to increase the melt expulsion. This leads to the formation of a larger, or wider, dimension in the re-solidified rim by molten material being expelled which is wider than the overlapping spacing.

9.4 Investigating the Effect of Indirect Laser Micro-textured and Non-textured Polyurethanes on BAE-1 Cell Adhesion and Cell Height Profile under Static Conditions

Since endothelial cell adhesion is the first biological response to a surface, BAE-1 cell adhesion on all indirect laser micro-textured and non-textured polyurethanes were investigated after 2 hours post-cell seeding. The adhesion results demonstrated that polyurethane 1A, which has microgroove features with a mean width of 27.16±2.01µm and a microfringe feature with a width of approximately 4.05±0.67µm, had the greatest effect on BAE-1 cell adhesion. To determine the

effect of microfringes on BAE-1 cell adhesion, a wavy surface, but with no microfringe features, was developed for comparison purposes (polyurethane 1D). Adhesion experiments found that the loss of microfringe structures drastically reduced BAE-1 cell adhesion compared to polyurethane 1A. This suggests that the microfringe structure is an important factor for inducing BAE-1 cell adhesion.

In contrast to the width of the microfringes on polyurethane 1A, polyurethanes 3A and 3D have a wider microripple structure with widths of 6.23±1.26±um and 6.27±0.82µm, respectively. By comparing polyurethane 3A and 3D to 1A, it was observed that the dimension of the microfringe was very important in inducing BAE-1 cells adhesion. Wider microripples with widths greater than 4µm had a poor performance with respect to cell adhesion of the BAE-1 cells.

Hwang *et al.* examined human umbilical vein endothelial cell (HUVEC) and calf pulmonary artery endothelial cell (CPAE) adhesion on fibronectin coated biodegradable poly(lactic-co-glycolic acid) (PLGA) substrates with features having the following dimensions; 350 nm wide ridges/350 nm grooves, 350 nm ridges/700 nm grooves, 350 nm ridges/1750 nm grooves, 700 nm ridges/350 nm grooves, 1050 nm ridges/350 nm grooves, 1750 nm ridges/350 nm grooves and non-textured PLGA under different shear stress forces for 40 minutes. They found that both cell types have highest cell adhesion on the substrate having 700nm ridges/350nm grooves under 40dyne/cm^2 shear stress. Their observation suggested that HUVECs having strong adhesion on 700nm ridges/350nm grooves was due to clustered focal adhesions. They observed that the focal adhesion of HUVECs on 700nm ridges/350nm grooves aligned to the ridge/groove direction with higher fluorescent intensity and density compared to non-patterned PLGA (Hwang *et al.*, 2010).

9.4.1 Cell Height Profile

Non-adherent cells in a medium suspension maintain a spherical cell morphology compared to adherent cells which are flatter. Integrins are the receptors that are responsible for the cell being able to adhere to the extracellular matrix (ECM), or substrate. Once the integrin is bound to the extracellular matrix components, it promotes cytoskeletal organization, cell flattening and spreading. *Re et al.* investigated the inhibition of anchorage-dependent cell spreading on substrate triggers apoptosis in cultured human endothelial cells. The authors showed that human umbilical vein endothelial cells (HUVECs) retained a round cell morphology and were incapable of organising actin microfilaments. It was found that they underwent apoptosis when cultured on low coating concentrations of either fibronectin, or vitronectin. In contrast, HUVECs became flattened, showed actin microfilament organisation and retained viability when cultured on high coating concentrations of fibronectin, or vitronectin (Re *et al.*, 1994).

In this study, it was found that BAE-1 cells growing on polyurethane 1A (which had the greatest adhesion) also had the lowest height profile compared to polyurethanes 1D, 3A, 3D, and non-textured polyurethanes. This would suggest that the BAE-1 cells were forming faster adhesions on this surface and thus proceed to flatten and spread quicker than the BAE-1 cells growing on the other surfaces. Focal adhesion formation will be discuss on section 9.6.

9.5 Investigating the Effect of Indirect Laser Micro-textured and Non-textured Polyurethanes on BAE-1 Cell Proliferation Under Static Conditions

Stent re-endothelisation is essentially a wound healing process, whereby adjacent/neighbouring endothelial cells at the wound edge proliferate and migrate to close the wound (Lee and Gotlieb, 2003). Therefore, to enhance the endothelial cell proliferation rate, it is crucial to shorten the healing period after stent deployment. Our observations showed that polyurethane 1A had the greatest ability to accelerate BAE-1 cell proliferation after 24, 48, 72 hours, compared with non-textured polyurethane. The work also found that wavy polyurethane 1D,

which has no microfringes, did not improve BAE-1 cell proliferation when compared to non-textured polyurethane. These results suggest that the microfringes on polyurethane 1A were the main feature that helped to accelerate cell proliferation.

The effect of polyurethanes 3A and 3D (which also have microripples) on BAE-1 cell proliferation were also investigated. It was found that polyurethane 3A (with a microripple width of 6.23±1.26±µm and height 0.17±0.06µm) did not have any effect on cell proliferation compared to non-textured polyurethane after 24, 48, 72 hours post seeding. However, microripples on polyurethane 3D, which has a mean width of 6.27±0.82µm (approximately the same as polyurethane 3A) and a depth of 0.21±0.07µm, enhanced cell proliferation compared to non-textured polyurethane. However, this was only found after 72 hours post seeding. These results indicate that the microripple depth is important in enhancing BAE-1 cell proliferation.

In contrast, Uttayarat *et al*. found there to be no significant difference in BAEC proliferation on substrates having a constant microgroove/ridge of ~3.5µm and different groove depths of 200nm, 500nm and 1µm (Uttayarat *et al.*, 2005). Sprague *et al*. however, showed that human aortic endothelial cells (HAEC) proliferation on 15µm wide microgrooved stainless steel and cobalt chromium was significantly higher compared to proliferation on non-textured stainless steel and cobalt chromium substrates (Sprague *et al.*, 2012).

As mentioned previously, cell adhesion, is the first biological response before proceeding to proliferation. Compared with the adhesion results, the proliferation results indicate that proliferation is dependent on cell adhesion. For example, accelerating cell adhesion could reduce the time for the cells to proceed to the cell proliferation stage, hence increasing the cell density at 24, 48, and 72 hours post cell seeding.

9.6 Investigating Focal Adhesion Formation and Actin Organisation of BAE-1 Cells on Polyurethane 1A and Non-textured Polyurethane Under Static Conditions

Growing BAE-1 cells on polyurethane 1A was found to influence vinculin formation and actin arrangement. The results showed that vinculin was localised and elongated along the microfringes (width: 4.05±0.67µm, height: 0.11±0.07µm). It was also noted that the vinculin were connected with dense actin stress fibres.

These results suggest that the microfringes affect the morphology and maturation of the focal adhesions. It would seem that once the focal adhesions have formed on the microfringes, they mature and elongate according to the shape of the microfringe. Moreover, the organisation and bundling of the actin stress fibres would seem to depend on the focal adhesion location and maturation status. These results agree with those of Uttayarat *et al.* who reported that in bovine aortic endothelial cells (BAECs), actin filaments and focal adhesions preferentially aligned along a ~3.5µm ridge, even when the depth of the channel was varied (200 nm, 500 nm, 1µm, and 5µm, respectively). Furthermore, the authors also observed that the focal adhesion on the 1µm depth channels, were mainly formed at the side wall of the channel. It was found that BAECs could not establish focal adhesions on the deepest channel of 5µm (Uttayarat *et al.*, 2005)(Uttayarat *et al.*, 2008). Den Braber *et al.* reported that microgrooves on a titanium substrate with widths of 1, 2, and 5µm, confined FAP formation to the ridge of the channels. Only rat dermal fibroblast (RDFs) cells on titanium having microgrooves with a width of 10µm, allowed cells to established FAP at the bottom of the groove (den Braber, Jansen, *et al.*, 1998).

In comparison to polyurethane 1A, it was observed that the focal adhesion on polyurethane 3A and 3D tended to form in between the microripple gap instead of on the microripple feature (see Figures 8.14 and 8.15 in Section 8.7). This may be due to the microripples being wider on polyurethane 3A and 3D. In contrast to polyurethane 3D, it was observed that polyurethane 3A, which had the shallower and narrower microripple, had less vinculin formation and elongation on the

microripple gap. Overall these findings suggest that microripple or microfringe width and depth can strongly influence focal adhesion formation.

9.7 Investigating BAE-1 Cell β-Actin Expression Level on Laser Micro-textured and Non-textured Polyurethanes Under Static Conditions

β-actin is predominantly localised in stress fibres, circular bundles and at cell-cell contacts, which suggests that β-actin plays an important role in cell attachment and contraction (Dugina *et al.*, 2009), and as such β-actin expression was measured on both micro-textured and non-textured polyurethanes. It was found that on polyurethane 1A and 3D β-actin expression was increased compared to non-textured polyurethane. It was observed that β-actin expression was sensitive to the width dimension and the depth of the microfringes and microripples.

The microfringes on polyurethanes 1A, with a width of 4.05±0.67μm and height of 0.11±0.07μm, were found to increase β-actin protein expression. When grown on polyurethanes 1D and 3A (with microripple widths of 6.23±1.26μm and a depth of 0.17±0.06μm respectively) they showed no significant difference in the mean level of actin expression when compared to the non-textured polyurethane. Although the microripple gap on polyurethane 3A has a slightly shallower depth and narrower width compared to that of polyurethane 3D, these were no obvious differences seen in β-actin expression compared to non-textured polyurethane. Furthermore, polyurethane 3D, which has the widest and deepest microripples, it was found that there was an increase in β-actin expression. Overall these findings suggest that feature dimension is an important regulator of β-actin expression. No previous research work can be found regarding endothelial cell β-actin expression on micro-textured surfaces. Further investigation is required to understand the effect of the microripple gap upon β-actin expression in real time and it is suggested that this should be carried out in the future.

9.8 Investigating BAE-1 Cell Migration Velocity, Distance, and Forward Migration Index on Indirect Laser Micro-textured and Non-textured Polyurethanes Under Static Conditions

9.8.1 BAE-1 Cell Migration Velocity and Distance

Live cell tracking was carried out to try and correlate β-actin protein expression to cell migration velocities on the micro-textured polyurethanes. Interestingly, it was found that on polyurethane 1A, which promoted the greatest level of actin expression, BAE-1 cell velocity was not significantly different compared to BAE-1 cell velocity on the non-textured polyurethane.

The highest cell migration velocity observed in our study was on polyurethane 3D with the widest width and deeper microripple gaps (width-6.59±1.21µm and depth-0.21±0.07µm). BAE-1 cells growing on all other micro-textured polyurethanes showed significantly higher cell migration velocity compared to non-textured polyurethane. These results suggested that β-actin expression and focal adhesion formation is correlated with BAE-1 cell adhesion and cell migration velocity. In the previous chapter, in section (8.2), polyurethane 3D was found have the lowest BAE-1 cell adhesion. It is therefore possible that microripple gap depth >170nm weaker cell adhesion/focal adhesion formation and facilitates cell migration velocity.

On polyurethane 1A it was found that BAE-1 cells formed a more mature focal adhesion with the microfringes. This may account for the relatively low migration velocity of BAE-1 cells observed on this substrate. The most reasonable explanation for the slower migration velocity might be due to strong cell-surface adhesion. A few researchers have shown that cell migration velocity is governed by ligand-cell binding affinity, i.e. Hunttenlocher *et al.*, showed that that either activating αIIbβ3 receptors by the LIBS6 antibody into a high affinity state, or via mutations in the integrin β cytoplasmic domains to increase ligand affinity, result in decreased cell migration rate (Huttenlocher *et al.*, 1996)(Palecek *et al.*, 1997).

Strong cell adhesion and high β-actin expression on polyurethane 1A are interrelated. Focal adhesion maturation is a key factor for cells to form strong adhesions with the surface by clustering the integrin receptor to increase cell-ligand binding affinity (Carman and Springer, 2003). However, focal adhesion maturation requires actin bundling and myosin contractile activities (Huttenlocher and Horwitz, 2011). In addition, Oakes *et al.* also proposed that tension itself is not sufficient for focal adhesion maturation without a stress fibre template. In order to facilitate focal adhesion maturation, actin stress fibres are required to assemble at the focal adhesion site to serve as a structural template for wide range tension (Oakes *et al.*, 2012). Hence the most plausible explanation of high β-actin expression may be due to a large amount of actin assembly and bundling at focal adhesion maturation.

9.8.2 BAE-1 Cell Forward Migration Index

This work also investigated the effect of indirect laser micro-textured polyurethanes on BAE-1 cell migration directionality. The forward migration index (FMI) showed that the cells migrated more frequently parallel to the microfringe features. The cells often changed migration direction when encountered the microfringes, the cells elongated parallel to the microfringe structure and changed their migration direction so as to be orthogonal to the microridges. As discussed previously in Section 9.3, the most plausible explanation of this phenomenon is that as the cell encounters the microfringes, the focal adhesions become elongated, parallel to the microfringes. As a result this induces the formation of parallel actin stress fibres between focal adhesions (as shown in Figure 8.12 in Section 8.4). These parallel actin stress fibres may influence the cell elongating parallel to the microfringes, which may cause the cell to change migration direction. Furthermore, polyurethane 1A also consists of microgrooves (width-11.15±1.72µm and depth-0.9±0.34µm) in-between the microridges, and cells were also found migrate along these microgrooves. If the surface was totally covered with only the microfringe features, the cells would probably only migrate in the direction parallel to the microfringes.

The FMI result also found that polyurethane 3D (microripples gap with width-6.59±1.21µm and depth-0.21±0.07µm) influenced the cells so that they more frequently migrated parallel to the microripple direction. In contrast to the microripple gap on polyurethane 3D, on polyurethane 3A the microripple gap was narrower and shallower (width-6.23±1.26µm and depth-0.17±0.06µm) and less cells were found to have migrated parallel to the microripples. The results suggested that 4nm shallower in depth on polyurethane 3A produced less focal adhesion confinement although the microripple width was 720nm smaller than polyurethane 3D. The result clearly suggested that the depth have more profound effect on cell migration orientation.

As discussed previously in Section 9.5, cells formed more favourable focal adhesion on the microfringes and microripple gaps which influences the actin filament alignment. The alignment of actin stress fibres are parallel to the microfringes and microripples and this in turn causes the cells to change directionality by elongating themselves parallel to the microfringes and microripple gaps.

Several studies have demonstrated that the ridge widths between 1 and 5µm are generally have more pronounced on cellular cytoskeletal and adhesion complex alignment compared to grooves and ridged topographies with larger lateral dimension (Karuri *et al.*, 2004)(den Braber, de Ruijter, *et al.*, 1998)(Teixeira *et al.*, 2003)(Matsuzaka *et al.*, 1999). Overall these findings suggest that microripple/fringe with width dimensions <4µm, or with depth dimensions >0.11µm are an important regulator that influences cell migration through both focal adhesion formation and actin filament organisation.

9.9 Investigating Cell Morphology, Focal Adhesion Formation and Actin Organisation of BAE-1 Cells on

Indirect Laser Micro-textured and Non-textured Polyurethanes Under Flow Conditions

In the arterial system endothelial cells possess an elongated morphology and align in the direction of the flow (Potter *et al.*, 2011). A number of studies have shown that *in vitro*, endothelial cells exposed to shear stress possess an elongated morphology, increased actin stress fibre formation, and large elongated mature focal adhesions. For example, Galbraith *et al.* demonstrated that BAECs cultured on glass coverslips undergo three distinct phases when subjected to 15dyne/cm^2 shear stress for 24 hours. During the first phase (3 hours post cell seeding), the cells became elongated, and exhibited more dense stress fibres, and apical microfilaments. In the second phase (6 hours post cells seeding), the cells became more mobile and lost their dense peripheral bands (actin microfilament which are located at to cell periphery)(Wong and Gotlieb, 1986). In the third phase (12 hours post cell seeding), the elongated cells orientated towards the flow. The actin stress fibres became thicker and were also closer together (Galbraith *et al.*, 1998).

Interestingly, in our studies after 24 hours the BAE-1 cells growing on all the micro-textured surfaces represented those described by Galbraith *et al*., in phase 1. However, it was also observed that only a few cells elongated with the flow direction on all micro-textured and non-textured polyurethane after 24 hours (see Figures 8.22-8.26 in Section 8.7). The results suggested that the cells seem to be starting to elongate after 24 hours. However, most of the studies showed that cells possessed an elongated form and alignment toward the direction of flow within 4 to 8 hours. Further investigation is required to try and understand this phenomenon.

The characteristic of larger focal adhesions and dense actin stress fibres on the microfringes (polyurethane 1A) were observed under static conditions and were not seen under any flow conditions. The results suggested that the microfringes on polyurethane have less effect on BAE-1 cells under flow conditions. Interestingly, it was observed that the microripple gap on polyurethane 3A and 3D have a more pronounced effect on focal adhesion under 20dyne/cm^2 shear stress. The most plausible explanation for this is that focal adhesions that form on deeper

microripple gap structures may provide stronger cell adhesions under flow conditions.

In contrast to the microripple gap on polyurethane 3A, the microripple gap on polyurethane 3D, had a more pronounced effect on focal adhesion and actin organisation. Cells growing on this latter substrate had dense actin stress fibres that were aligned parallel with the microripples and orthogonal to the direction of flow. This may be due to polyurethane 3D having ~4nm deeper microripple gaps compared to polyurethane 3A as was discussed previously.

These experimental results are similar to those of Uttayarat *et al*., who exposed BAECs cells to a shear stress of 50dyne/cm^2 with the flow direction perpendicular to the microgrooves. They found that the cells migrated orthogonal to the microgrooves in the direction of the flow, but that the focal adhesions and actin filaments remained aligned along the microgrooves, instead of following the flow direction. They suggested that the microgroove topography was more effective in cell guidance, and structural protein guidance during exposure to the flow (Uttayarat *et al.*, 2008).

The overall finding showed that >210nm in microripple/microfringes gap depth effectively induced recruitment of focal adhesions and actin filaments under flows of 20dyne/cm^2. Many studies have suggested that biomechanical forces in combination with surface topography can modulate the endothelial phenotype and function through changes of gene expression (Johnson *et al.*, 2011)(Davies *et al.*, 2013)(Morgan *et al.*, 2012). Hence, further investigation using the GeneCalling technique is required to understand how physiological shear stress and endothelial mechano-transduction signalling pathways could alter the endothelial gene expression and change its phenotype (Wasserman *et al.*, 2002).

9.10 Investigating the Effect of Indirect Laser Micro-textured and Non-textured Polyurethanes on HCASMC Adhesion Under Static Conditions

The results presented in this thesis have showed that no HCASMCs cells were found to be attached on the micro-textured and non-textured polyurethane after 2, 4, and 8 hours post seeding. It was observed that polyurethane itself delayed HCASMCs adhesion to the surface, however, the mechanism of how polyurethane delayed HCASMCs adhesion is not understood. Further investigation is required to understand the effect Z1A1 polyurethane chemical properties on HCASMCs and also surface topography cues induce HCASMCs phenotypic changes (such as, synthetic or contractile phenotypes).

9.11 Investigating the Effect of Indirect Laser Micro-textured and Non-textured Polyurethanes on HCASMC Proliferation Under Static Conditions

HCASMCs proliferation on indirect laser micro-textured and non-textured polymers was investigated. No significant difference in proliferation was found when comparing all the micro-textured polyurethanes to non-textured polyurethane at 24, 48, and 72 hours post seeding (see Figure 8.18 in Section 8.10). However, there was a significant difference found when comparing BAE-1 proliferation with HCASMCs proliferation. The comparison showed that on the non-textured polyurethane proliferation rate was 2.8 fold higher for HCASMCs compared to the BAE-1 cells.

Past research has shown that confining SMC spreading reduces cell proliferation. Thakar *et al.* demonstrated that the cell morphology regulated SMCs proliferation. They examined human aortic smooth muscle cells (HASMCs) on PDMS with microgrooves (10µm width and 2.8µm depth) and observed that the HASMCs were elongated in morphology, had a lower proliferation rate and a lower cell density. The nucleus and cell shape indexes were also lower compared to non-pattern PDMS. Also, DNA microarray profiling revealed that the elongated HASMCs had lower neuron derived orphan receptor-1 (NOR-1) expression. NOR-1 is responsible for DNA synthesis and if knock-out NOR-1 expression, analysis has shown that this will suppress DNA synthesis (Thakar *et al.*, 2009).

In this study, the HCSMACs were found to be elongated and aligned along the microridges on polyurethanes 1A, 3A and 3D (see Figures 8.19, 8.21 and 8.22 in Section 8.11). However, the depth and lateral width of the microridges were shallower and wider compared to those that were used by Thakar *et al.* (see Table 7.3 and 7.4 in Section 7.4), which allowed the HCSMCs to spread more freely and cross over from groove to groove, or ridge to ridge, without any restriction (Thakar *et al.*, 2009).

Although polyurethanes 1A, 3A and 3D had narrower microfringes and microripples, which were orthogonal to the microridge, HCASMCs parallel alignment, with these two features, was not observed. This could be due to the depth of the microfringes and microripples not being sufficiently great enough to restrict the SMCs spreading and alignment behaviour. This seems plausible as Yim *et al.* have shown that bovine pulmonary artery smooth muscle cells aligned and elongated on poly(methyl methacrylate) (PMMA) having nanogrooves with a line width of 350nm, a pitch of 700nm and a depth of 350nm. Moreover, they showed that the nano-grooves significantly decreased cell proliferation when compared to plain PMMA (Yim *et al.*, 2005).

Overall these findings indicate that the microripple or fringes depth dimension has a greater effect than the microripple width dimension with respect to decreasing cell proliferation. The HCASMCs phenotypic changes induce by laser micro-fabricated surface topography can be further investigate by defining and characterising using protein marker such as (α-smooth muscle actin (α-SMA), smooth muscle-myosin heavy chain (SM-MHC), smoothelin-A/B, SMemb/non-muscle MHC isoform-B and cellular retinol binding protein (CRBP)-1). Synthetic SMCs usually contain large numbers of organelles, whereas contractile SMCs are largely replaced by actin filaments. This investigation is crucial to understand the proliferation behaviour of HCASMCs because these two SMCs phenotypes have different proliferative and migratory characteristics, for example, contractile SMCs exhibit lower growth rate and lower migratory activity than synthetic SMCs (Rensen *et al.*, 2007).

9.12 Investigating Actin Organisation of HCASMC on Indirect Laser Micro-textured Polyurethane Under Static Conditions

It was observed that HCASMC cells were predominantly aligned in a parallel fashion along the microridge features on polyurethanes 1A, 3A and 3D, instead of being aligned to the microfringes or microripples. This may be due to the shallower depth/height of the microfringes and microripples on polyurethanes 1A (0.11±0.07µm), 3A (0.17±0.06µm) and 3D (0.21±0.07µm). Furthermore, HCASMC cells were found to cross over the microridges structures on polyurethanes 1A (0.9±0.34µm) and 3A (0.71±0.22µm) with less cells crossing over on polyurethane 3D. This may be due to the higher microridge height (1.23±0.27µm) on polyurethane 3D. Sarkare *et al*. studied human umbilical smooth muscle cell (HUVS-112D) organization on PDMS microgrooved surfaces. They observed that more than 90% of the HUVS-112D cells were aligned on the grooves in between18-78µm and 4.7µm in depth on PDMS microgrooves. They also found that most of the cells were predominantly located in the grooves (Sarkar *et al.*, 2005). In comparison with the results presented here in this thesis showed that the height of the microridges is the major factor that affects HCASMC alignment and that a microridge height of at least ≥1µm is required to control HCASMCs.

As discuss previously that the contractile SMCs phenotype exhibit elongated morphology and contain larger amount actin filament (Rensen *et al.*, 2007). This general characteristic were similar to our experiment result that the HCASMCs exhibited an elongated morphology with large amount of actin filament aligned along the microridges on polyurethane 1A, 3A and 3D. Therefore, further investigation is required to confirm HCASMCs phenotypes by using protein markers and studying how the surface topographical dimension cues can induce the phenotypic changes.

Chapter 10

10.0 Conclusion

10.1 Optimization of Direct Laser Microfringes and Microripples Microfabrication

Over the past 20 years, a range of advanced micro and nanofabrication technologies have been adopted by scientists working in tissue engineering, to produce user-designed surface topographies for controlling aspects of cell behaviour. A diverse range of micro and nano-topographies have been designed and produced including microgrooves, pillars and pits. These structures have been shown to enhance cell bio-functionality and show great promise in many biomedical applications including implant technology. The topography most studied to date is the microgroove, where it has been shown that microgroove structures have an impact in stent technology.

This present study aimed to use laser technology to develop micro-textured surfaces that may be used to control the adhesion and growth of both endothelial and smooth muscle cells. Using laser technology ~4µm microfringe and ~6µm microripple structures were generated upon ~23-40µm larger microridge features. This was achieved through optimising laser parameters and through using beam overlapping strategies to successfully micro-fabricate a stainless steel master mould. This mould was then used to develop a polymer cast, which would subsequently act as a substrate for cell culture.

Inspection of the processed steel moulds, using SEM and white light interferometry, showed that the pattern was developed due to a thermal process, which deposited thermal energy into the stainless steel surface, causing melting and melt expulsion. This expulsion formed a recast elevated ring around the beam spot, which formed the microripple/fringe structures by further overlapping the

laser beam spot. In conclusion, the current laser system settings can be used to generate microfringes and microripples through the laser overlapping technique that has been described. The smaller elevated ring can be generated by beam overlapping strategies, but is limited to features approximately 4µm in width. Furthermore, producing smaller structures proved to be difficult and the height of the microripples/fringes was difficult to control due to reconsolidation of the elevated rim caused by the relatively high laser fluence.

10.2 Investigating BAE-1 and HCASMCs Responses to Laser Micro-textured Microfringes and Microripples

The main objective of this thesis was to use laser micro-textured surfaces generated by the laser overlapping technique, to physically accelerate endothelial cell adhesion and proliferation, whilst correspondingly suppressing smooth muscle cell growth. The study found that laser microfringe features accelerate BAE-1 cell adhesion after 2 hours post cell seeding. This enhanced adhesion of the BAE-1 cells may be facilitated by the larger elongated matured focal adhesion formations which were observed on the microfringe features.

The results from this work showed that adhesion and proliferation of BAE-1 cells cultured on polymers having microfringe features are somewhat interdependent. This is because cells cultured on those substrates that enhanced adhesion (i.e. those having a significant numbers of microfringes) also promoted the greatest cell proliferation. Hence, an accelerated BAE-1 cell adhesion rate can simultaneously increase the proliferation of BAE-1 cells.

The level of actin expression was quantified for BAE-1 cells cultured on all polymer substrates. It was found that cells growing on polyurethanes with microfringe and microripple features had a greater level of β-actin expression than those surfaces that did not have these features. The increased level of β-actin expression may be induced by the microfringe and microripple structures. Furthermore, the dimensions of the microfringe width and the microripple depth are important factors for inducing β-actin expression.

It was also found that, by using time-lapse imaging and cell tracking, BAE-1 cells growing on polyurethane 1A had the same mean cell migration velocity than cells growing on the non-textured polyurethane. This slow mean cell migration velocity may be due to strong BAE-1 cell adhesion on ~4µm of the microfringe structures. However, the high β-actin protein expression level may be due to actin bundling and contractile activity during the focal adhesion maturation process. The high mean cell migration velocity on polyurethane 3D may be due to either weaker BAE-1 cell adhesion, or high levels of β-actin expression. BAE-1 cells on ~4µm microfringe features generated by laser beam overlapping show enhanced cell adhesion and supressed cell migration velocity. On the other hand, BAE-1 cells on ~6µm microripple features which are larger than the microfringes mediated β-actin protein expression and increased cell migration velocity.

The BAE-1 cell migration directionality study performed on polyurethane 1A supports the assumption that focal adhesions are confined to the microfringe structures, leading to cells changing migration directionality when encountering a microfringe feature. The focal adhesions are confined to the microfringes, leading to an alignment of actin stress fibers between the elongated focal adhesion complexes and thus changing cell elongation orientation. The microripples did not show any influence on cell migration directionality. This was due to the relatively large width dimension of the structure, which lacked the ability to confine focal adhesions to the microripple structures.

Microfringe and microripple structures were found not to have any effect on HCASMC alignment. This may be due to this cell type's low sensitivity to shallow features. However, HCASMCs were found to align along the microridge features, which may be due to the high height to width ratio.

Under 20dyne/cm2 shear stress conditions on polyurethanes 1A, 1D, 3A, 3D and non-textured polyurethane, BAE-1 cells did not align, or elongate, to the flow direction. When BAE-1 cells were grown on polyurethanes 3A and 3D under shear stress conditions, they exhibited a greater level of parallel actin stress fibres aligned to the microripple compared to when there was no shear stress present. This may be due the confinement of the focal adhesions to the microripple gap structures leading to the forming of actin alignments, which also had a greater

effect on cell shape and migration directionality. If the effect of the surface topography is greater than the shear stress force of the fluid flow, then the cell can migrate in parallel along the microripple, instead of following the direction of the fluid flow.

Microfringe and microripple features had no effect on HCASMC adhesion at a duration of 2 hours post cell seeding. It is not known why this was the case, however these results suggest that the polyurethane was having an inhibitory effect with respect to cell adhesion. Furthermore, 100-200nm depth microfringes and microripples were not deep enough to suppress HCASMCs proliferation due to the low response sensitivity of HCASMCs.

In conclusion, the most important factors for BAE-1 cell control are the >4μm width and >200nm depth of the microstructures that are cast in the polyurethane. These laser textured microfringe and microripple dimensions have a major effect on BAE-1 cells and their behaviours including cells adhesion, proliferation, β-actin gene expression, migration velocity and directionality, under both static and flow conditions. In addition, the Z1A1 polyurethane used in this study has been shown to have an inhibitory effect on HCAMSCs adhesion, however the mechanism is not yet understood and requires further investigation. The purpose of this research is to provide preliminary data for stent technology development in the future by direct laser micro-textured microfringes, ripples, and ridges, on the inner stent surface and nano-coated with Z1A1 polyurethane to enhance, or accelerate, re-endotheliazation and reduce in-stent restenosis.

Chapter 11

11.0 Recommendations For Future Work

11.1 Ultra-Short Pulses For Direct Laser Micro and Nanofabrication

In this investigation of the effect of micro-textured surfaces on cell behaviour, all of the surface topographies were micro-fabricated using a short pulse nanosecond SPI infrared solid state fibre laser. The micro-features produced are the result of the nanosecond laser pulse's interaction with a metal substrate. The infrared laser exchanges energy with the atomic lattice of the metal through thermal vibrations, where the photon causes the atomic lattice of the metal to increase in vibration. This causes the surface of the metal substrate to melt and flow into different patterns driven by forces generated by other laser pulses deposited onto the surface. This mechanism of melt formation produced the microridges, microfringes and the microripples described here. This study has identified the importance of controlling the thermal input into a metallic substrate, as this is the most important factor for controlling the size of the features through melt formation. The author believes that controlling this thermal input, and hence feature size, using the parameters of mean laser power, pulse duration, repetition rate and scanning speed, has reached its limitations with this nanosecond laser pulsed system. The only possible improvement with respect to feature size for this type of nanosecond laser is to improve its beam quality, i.e. the M^2 value of the laser beam.

In future work other potential laser systems could be studied that could prove to be interesting in terms of producing micro-features for controlling cell behaviour. Such lasers include picosecond and femtosecond laser systems. Femtosecond micromachining is now a well-established area of research. A number of research groups around the world have used this type of system to produce a number of different structures and have investigated their cell control properties. It would be

interesting to use a femtosecond laser to reproduce the structures produced in the investigation. The femtosecond laser uses a different mechanism to interact with the atomic lattice. The electric field produced by the laser is so intense, that it rips the electrons from the surface, followed by the bulk of the material. This process is called Coulomb explosion, and is also referred to as “cold ablation”. This processing mechanism could potentially improve the dimensional accuracy of the microridges, microfringes and microripples.

Femtosecond lasers could be used to micro-fabricate material with ultra-precision with negligible thermal input and the method is not sensitive to material properties, such as the absorptivity of the material. This would allow the direct machining of the polyurethane substrate used in these experiments and would hence allow avoiding the polymer moulding procedure altogether, which would then be unnecessary. Moreover, research by a number of different groups have demonstrated that femtosecond lasers are capable of inducing periodic surface structures (LIPSS) through interference between the incident laser beam and surface plasmon-polariton waves, that could generate ripples at the nano-scale, ranging from 500-700nm (Gurevich and Gurevich, 2014)(Tan and Venkatakrishnan, 2006).

The use of micro and nano structures to enhance endothelial cell growth and to supress SMCs functions have been investigated by a number of different research groups. However, most of the micro and nano sized features were produce using MEMS technology, which generally incurs high capital costs and is time consuming. With ultra-fast short-pulse laser systems, micro and nanoscale structures can be integrated to form both a primary and secondary surface topography. For example, microgrooves may be used as the primary structure, functioning to regulate SMC shape by confining the cells to specifically designed areas on the biomedical implant and supressing SMC proliferation. This could be followed by post-processing LIPSS (such as nano-ripples) on the microgrooves as secondary structures, which could function to induce endothelial cell adhesion, proliferation and alignment, so as to improve stent surface functionality. This complex surface topography design could enable greater functionalization of the surface of biomedical implants, including stents.

11.2 Investigating the Dynamics of Focal Adhesion and Actin Filament Formation and Organization in Real Time under Physiological Static and Flow Conditions

The focal adhesion and actin filament formation and organisation shown in this work were achieved via post-cell staining (which is not a real time analysis technique). The cells were fixed at a specific time and stained with fluorescent antibodies for visualization. Although we can study the focal adhesion and actin organisation through these analytical methods, the data provided only showed focal adhesion and actin filament formation and organisation at a specific time point. The study could not show the dynamic changes of focal adhesions and actin filament formation and organisation when interacting with the microfringe and microripple structures. This study therefore still leaves a number of unanswered questions that must be answered, if this technology is to move forward into the production of real implants. These questions cannot be resolved by information generated from non-dynamic post cell staining, they are:

1. Why focal adhesions are preferentially formed on the microfringe and microripple gaps?
2. How do focal adhesions form and interact with indirect laser micro-textured polyurethanes?
3. How do microfringes and microripples affect endothelial and smooth muscle cell phenotypes?

To help answer the above questions the main components of the focal adhesion complexes (e.g. paxillin, vinculin, talin) and actin GFP plasmids can be transfected into the endothelial cells to generate temporary, or stable, cell lines. This would allow visualisation of focal adhesion formation and actin filament organisation both under static and flow conditions, thus eliminating the need for post-cell staining procedures. This would allow one to visualise focal adhesion and actin filament dynamics in real time with data analysis being carried out using imaging processing software. This would provide more insight into how the cells interact

with and interpret physical cues from the indirect laser micro-textured polyurethanes.

11.3 Develop Systems to Better Mimic *in vitro* Condition to study BAE-1 and SMC Cells behaviour

Many features have to be taken into consideration when imitating the conditions within the coronary artery. Most of the research in this thesis simply seeded HCASMCs or BAE-1 cells onto indirect laser micro-textured polyurethanes and analysed their behaviour. However, the coronary artery consists of three layers of cells, including endothelial, SMC and fibroblast cells. As discussed previously, endothelial cells in the coronary artery play an important role in controlling SMCs in quiescent phenotypes. SMCs convert to a proliferative phenotype after endothelial denudation which is caused during stent deployment and which leads to neointimal in-stent restenosis.

To imitate the architecture of the coronary artery, SMC and endothelial cells could be seeded inside a polyurethane tube to establish two layers of cells with the SMC cells in the outer layer and the endothelial cells in the inner layer. Once the bilayer of cells has been formed, physiological shear stress could then be applied to the cells for various time periods (i.e. 24-72hrs) so as to imitate the elongated cell morphology in the artery. Stents textured with micro and nano scale topographies could then be expanded inside the polyurethane tube containing the two layers of cells. The stent strut would press against the polyurethane tube wall and compress the cells, leading to denudation. Continuous shear stress would be applied to the endothelial cells and SMCs within the polyurethane tube. It may be expected at this point that following denudation, the cells would start migrating along the stent to compete for the available surface area on the stent strut. This could be monitored using real-time, 4 dimensional imaging techniques and post imaging analysis.

In previous work, manual tracking of a very large number of cells on indirect laser micro-textured polyurethanes has proven to be very difficult and time consuming. Especially, tracking of cell detachment or cell death under flow conditions.

However, post cell staining cannot provide accurate information about how the micro-features affect the internal molecular structure of the cell and lead to a change in cell directionality. To overcome this technical problem Metamorph Inc.'s Metamorph software, or Media Cybernetic's Image Pro software, or similar, could be used to automatically track cell movement. In addition, this software can also provide analytical functions, such as cell adhesion, proliferation, cell 4D migration tracking, 3D cell volume, and 3D cell measurement. Furthermore, both endothelial cells and SMC phenotypes under static and shear stress conditions could be identified by studying the shear-regulated gene using specific sets of primers and analysed through the use of protein microarrays and real time quantitative polymerase chain reactions (RT-qPCR).

References

Agarwal, A., Farouz, Y., Nesmith, A.P., Deravi, L.F., McCain, M.L., Parker, K.K. (2013) Micropatterning Alginate Substrates for In Vitro Cardiovascular Muscle on a Chip. *Advanced Functional Materials*. **23**(30), 3738–3746.

Albersen, M., Fandel, T., Lin, G., Wang, G., Banie, L., Lin, C., Lue, T. (2010) Injections of adipose tissue-derived stem cells and stem cell lysate improve recovery of erectile function in a rat model of cavernous nerve injury. *Journal of Sexual Medicine*. **7**(10).

Alttissimo, M. (2010) E-beam lithography for micro-/nanofabrication. *Biomicrofluidics*. **4**(2).

Angioplasty (2014) . *Britannica Online for Kids*. [online]. Available from: http://kids.britannica.com/comptons/article-9316337/Angioplasty This feature allows you to export a Britannica citation in the RIS format used by many citation management software programs. [Accessed May 20, 2014].

Atala, A., Bauer, S.B., Soker, S., Yoo, J.J., Retik, A.B. (2006) Tissue-engineered autologous bladders for patients needing cystoplasty. *The Lancet*. **367**(9518), 1241–1246.

Baac, H., Lee, J.H., Seo, J.M., Park, T.H., Chung, H., Lee, S.-D., Kim, S.J. (2004) Submicron-scale topographical control of cell growth using holographic surface relief grating. *14th Molecular Electronics and Devices Symposium*. **24**(1–2), 209–212.

Beldon, P. (2007) What you need to know about skin grafts and donor site wounds. *Wound Essential*. **2**, 149–155.

Betancourt, T., Brannon-Peppas, L. (2006) Micro-and nanofabrication methods in nanotechnological medical and pharmaceutical devices. **1**(4), 483–95.

Bhatheja, K., Field, J. (2006) Schwann cells: Origins and role in axonal maintenance and regeneration. *The International Journal of Biochemistry & Cell Biology*. **38**(12), 1995–1999.

Biela, S.A., Su, Y., Spatz, J.P., Kemkemer, R. (2009) Different sensitivity of human endothelial cells, smooth muscle cells and fibroblasts to topography in the nano-micro range. *Acta Biomaterialia*. **5**(7), 2460–2466.

Bitar, K.N., Raghavan, S. (2012) Intestinal tissue engineering: current concepts and future vision of regenerative medicine in the gut. *Neurogastroenterology and Motility: The Official Journal of the European Gastrointestinal Motility Society*. **24**(1), 7–19.

Bonse, J., Rosenfeld, A., Krüger, J. (2009) On the role of surface plasmon polaritons in the formation of laser-induced periodic surface structures upon

irradiation of silicon by femtosecond-laser pulses. *Journal of Applied Physics*. **106**(10), 104910.

Den Braber, E.T., Jansen, H.V., de Boer, M.J., Croes, H.J.E., Elwenspoek, M., Ginsel, L.A., Jansen, J.A. (1998) Scanning electron microscopic, transmission electron microscopic, and confocal laser scanning microscopic observation of fibroblasts cultured on microgrooved surfaces of bulk titanium substrata. *Journal of Biomedical Materials Research*. **40**(3), 425–433.

Den Braber, E.T., de Ruijter, J.E., Ginsel, L.A., von Recum, A.F., Jansen, J.A. (1998) Orientation of ECM protein deposition, fibroblast cytoskeleton, and attachment complex components on silicone microgrooved surfaces. *Journal of Biomedical Materials Research*. **40**(2), 291–300.

Bremus-Koebberling, E.A., Beckemper, S., Koch, B., Gillner, A. (2012) Nano structures via laser interference patterning for guided cell growth of neuronal cells. *Journal of Laser Applications*. **24**(4).

Broers, A.N., Hoole, A.C.F., Ryan, J.M. (1996) Electron beam lithography—Resolution limits. *Nanotechnology*. **32**(1–4), 131–142.

Broglia, M.F., Suarez, S., Soldera, F., Mücklich, F., Barbero, C.A., Bellingeri, R., Alustiza, F., Acevedo, D. (2014) Direct laser interference patterning of polystyrene films doped with azo dyes, using 355 nm laser light. *Applied Surface Science*. **300**(0), 86 – 90.

Brown, M., Arnold, C. (2010) Fundamentals of Laser-Material Interaction and Application to Multiscale Surface Modification. In K. Sugioka, M. Meunier, & A. Piqué, eds. *Laser Precision Microfabrication*. Springer Series in Materials Science. Springer Berlin Heidelberg, pp. 91–120.

Brunette, D. (1986) Spreading and orientation of epithelial cells on grooved substrata. *Experimental cell research*. **167**(1), 203–217.

Bunge, R.P. (1993) Expanding roles for the Schwann cell: Ensheathment, myelination, trophism and regeneration. *Current Opinion in Neurobiology*. **3**(5), 805–809.

Burg, T., Cass, C., Groff, R., Pepper, M., Burg, K. (2010) Building off-the-shelf tissue-engineered composites. *Philosophical Transactions of the Royal Society A: Mathematical, Physical and Engineering Sciences*. **368**(1917), 1839–62.

Carman, C.V., Springer, T.A. (2003) Integrin avidity regulation: are changes in affinity and conformation underemphasized? *Current Opinion in Cell Biology*. **15**(5), 547–556.

Carvalho, E.J., Alves, M.A.R., Braga, E.S., Cescato, L. (2006) SiO2 single layer for reduction of the standing wave effects in the interference lithography of deep photoresist structures on Si. *Microelectronics Journal*. **37**(11), 1265 – 1270.

Casper, C.L., Stephens, J.S., Tassi, N.G., Chase, D.B., Rabolt, J.F. (2003) Controlling Surface Morphology of Electrospun Polystyrene Fibers: Effect of Humidity and Molecular Weight in the Electrospinning Process. *Macromolecules*. **37**(2), 573–578.

Charest, J.L., Bryant, L.E., Garcia, A.J., King, W.P. (2004) Hot embossing for micropatterned cell substrates. *Biomaterials*. **25**(19), 4767–4775.

Charnley, M., Textor, M., Khademhosseini, A., Lutolf, M.P. (2009) Integration column: microwell arrays for mammalian cell culture. *Integrative Biology*. **1**(11-12), 625–634.

Chua, M.C.H., Chee Kong Chui, Bina Rai, Lau, D.D.P. (2013) Development of a patient specific artificial tracheal prosthesis: Design, mechanical behavior analysis and manufacturing. In Engineering in Medicine and Biology Society (EMBC), 2013 35th Annual International Conference of the IEEE. pp. 6236–6239.

Claeyssens, F., Hasan, E.A., Gaidukeviciute, A., Achilleos, D.S., Ranella, A., Reinhardt, C., Ovsianikov, A., Shizhou, X., Fotakis, C., Vamvakaki, M., Chichkov, B.N., Farsari, M. (2009) Three-Dimensional Biodegradable Structures Fabricated by Two-Photon Polymerization. *Langmuir*. **25**(5), 3219–3223.

Clark, P., Connolly, P., Curtis, A., Dow, J. (1987) Topographical control of cell behaviour. I. Simple step cues. . **99**, 439–448.

Clark, P., Connolly, P., Curtis, A., Dow, J. (1990) Topographical control of cell behaviour: II. Multiple grooved substrata. . **108**, 635–644.

Costache, F., Henyk, M., Reif, J. (2002) Modification of dielectric surfaces with ultra-short laser pulses. *European Materials Research Society 2001 Symposium L : Photon-induced Surface Processing*. **186**(1–4), 352–357.

Curtis, A.S.G., Varde, M. (1964) Control of Cell Behavior: Topological Factors. *Journal of the National Cancer Institute*. **33**(1), 15–26.

Dalby, M.J., Gadegaard, N., Tare, R., Andar, A., Riehle, M.O., Herzyk, P., Wilkinson, C.D.W., Oreffo, R.O.C. (2007) The control of human mesenchymal cell differentiation using nanoscale symmetry and disorder. *Nature Materials*. **6**(12), 997–1003.

Dalton, B., Walboomers, X.F., Dziegielewski, M., Evans, M.D.M., Taylor, S., Jansen, J.A., Steele, J.G. (2001) Modulation of epithelial tissue and cell migration by microgrooves. *Journal of Biomedical Materials Research*. **56**(2), 195–207.

Davies, J. (2001) Extracellular Matrix. *Nature Publishing Group*.

Davies, P.F., Civelek, M., Fang, Y., Fleming, I. (2013) The atherosusceptible endothelium: endothelial phenotypes in complex haemodynamic shear stress regions in vivo. *Cardiovascular Research*. **99**(2), 315–327.

Dee, R. (2013) Who Assisted Whom? *Texas Heart Institute Journal*. **30(1)**, 90.

Demidova-Rice, T.N., Hamblin, M.R., Herman, I.M. (2012) Acute and Impaired Wound Healing: Pathophysiology and Current Methods for Drug Delivery, Part 1: Normal and Chronic Wounds: Biology, Causes, and Approaches to Care. *Advances in skin & wound care*. **25**(7), 304–314.

Dibra, A., Kastrati, A., Mehilli, J., Pache, J., von Oepen, R., Dirschinger, J., Schömig, A. (2005) Influence of stent surface topography on the outcomes of patients undergoing coronary stenting: A randomized double-blind controlled trial. *Catheterization and Cardiovascular Interventions*. **65**(3), 374–380.

Dong, Y., Molian, P. (2004) Coulomb explosion-induced formation of highly oriented nanoparticles on thin films of 3C–SiC by the femtosecond pulsed laser. *Applied Physics Letters*. **84**(1), 10–12.

Drewa, T., Adamowicz, J., Sharma, A. (2012) Tissue engineering for the oncologic urinary bladder. *Nat Rev Urol*. **9**(10), 561–572.

Dugina, V., Zwaenepoel, I., Gabbiani, G., Clement, S., Chaponnier, C. (2009) Beta and gamma-cytoplasmic actins display distinct distribution and functional diversity. *Journal of Cell Science*. **122**(16).

Fillies, T., Wiesmann, H.P., Sommer, D., Joos, U., Meyer, U. (2005) Osteoblast reaction on SLA and microgrooved implant surfaces. *Mund-, Kiefer- und Gesichtschirurgie*. **9**(1), 24–28.

Fong, H., Chun, I., Reneker, D.. (1999) Beaded nanofibers formed during electrospinning. *Polymer*. **40**(16), 4585–4592.

Formanek, F., Takeyasu, N., Tanaka, T., Chiyoda, K., Ishikawa, A., Kawata, S. (2006) Three-dimensional fabrication of metallic nanostructures over large areas by two-photon polymerization. *Opt. Express*. **14**(2), 800–809.

Franchi, M., Trirè, A., Quaranta, M., Orsini, E., Ottani, V. (2007) Collagen structure of tendon relates to function. *TheScientificWorldJournal*. **7**, 404–420.

Frey, M.T., Tsai, I.Y., Ruseell, T.P., Hanks, S.K., Wang, Y. (2006) Cellular Responses to Substrate Topography: Role of Myosin II and Focal Adhesion Kinase. *Biophysical Journal*. **90**(10), 3774–3782.

Friedrich MJ (2004) Researchers make the case for human embryonic stem cell research. *JAMA*. **292**(7), 791–792.

Fu, Y., Ngoi, K. (2004) Focused ion beam direct fabrication of micro-optical elements: features compared with laser beam and electron beam direct writing.

Fulco, I., Miot, S., Haug, M.D., Barbero, A., Wixmerten, A., Feliciano, S., Wolf, F., Jundt, G., Marsano, A., Farhadi, J., Heberer, M., Jakob, M., Schaefer, D.J., Martin, I. (2014) Engineered autologous cartilage tissue for nasal reconstruction after tumour resection: an observational first-in-human trial. *The Lancet*. **384**(9940), 337–346.

Galbraith, C.G., Skalak, R., Chien, S. (1998) Shear stress induces spatial reorganization of the endothelial cell cytoskeleton. *Cell Motility and the Cytoskeleton*. **40**(4), 317–330.

García, M.A.A., Yebra, B.G., Flores, A.L.L., Guerra, E.G. (2012) The Major Histocompatibility Complex in Transplantation. *Journal of Transplataion*, 7.

Garg, S., Serruys, P.W. (2010) Coronary Stents: Looking Forward. *Journal of the American College of Cardiology*. **56**(10), 43 – 78.

Garg, U., Hassid, A. (1989) Nitric oxide-generating vasodilators and 8-bromo-cyclic guanosine monophosphate inhibit mitogenesis and proliferation of cultured rat vascular smooth muscle cells. *The Journal of clinical investigation*. **83**(5), 1774–1777.

Garrelie, F., Colombier, J.-P., Pigeon, F., Tonchev, S., Faure, N., Bounhalli, M., Reynaud, S., Parriaux, O. (2011) Evidence of surface plasmon resonance in ultrafast laser-induced ripples. *Opt. Express*. **19**(10), 9035–9043.

Ghibaudo, M., Trichet, L., Digabel, J.L., Richert, A., Hersen, P., Ladoux, B. (2009) Substrate Topography Induces a Crossover from 2D to 3D Behavior in Fibroblast Migration. *Biophysical Journal*. **97**.

Gittard, S.D., Ovsianikov, A., Monteiro-Riviere, N.A., Lusk, J., Morel, P., Minghetti, P., Lenardi, C., Chichkov, B.N., Narayan, R.J. (2009) Fabrication of Polymer Microneedles Using a Two-Photon Polymerization and Micromolding Process. *Journal of Diabetes Science and Technology*. **3**(2), 304–311.

Gonfiotti, A., Jaus, M.O., Barale, D., Baiguera, S., Comin, C., Lavorini, F., Fontana, G., Sibila, O., Rombol, G., Jungebluth, P., Macchiarini, P. (2014) The first tissue-engineered airway transplantation: 5-year follow-up results. *The Lancet*. **383**(9913), 238–244.

Grigorescu, A.E., Hagen, C.W. (2009) Resists for sub-20-nm electron beam lithography with a focus on HSQ: state of the art. *Nanotechnology*. **20**(29), 292001.

Guerin, L.J., Bossel, M., Demmierre, M., Calmes, S., Renaud, P. (1997) Simple and low cost fabrication of embedded micro-channels by using a new thick-film photoplastic. . **2**, 1419–1422.

Gurevich, E.L., Gurevich, S.V. (2014) Laser Induced Periodic Surface Structures induced by surface plasmons coupled via roughness. *Applied Surface Science*. **302**, 118–123.

Hahmann, P., Fortagne, O. (2009) 50 years of electron beam lithography: Contributions from Jena (Germany). *MNE '08 The 34th International Conference on Micro- and Nano-Engineering (MNE)*. **86**(4–6), 438–441.

Hanke, H., Kamenz, J., Hassenstein, S. (1995) Prolonged proliferative response of smooth muscle cells after experimental intravascular stenting. *European heart journal*. **16**(6), 785–93.

Harriott, L.R. (2001) Limits of lithography. *Proceedings of the IEEE*. **89**(3), 366–374.

Harrison, R.G. (1911) On the Stereotropism of Embryonic Cells. *Science*. **34**(870), 279–281.

Harrison, R.G. (1914) The reaction of embryonic cells to solid structures. *Journal of Experimental Zoology*. **17**(4), 521–544.

Le Harzic, R., Dörr, D., Sauer, D., Stracke, F., Zimmermann, H. (2011) Generation of high spatial frequency ripples on silicon under ultrashort laser pulses irradiation. *Applied Physics Letters*. **98**(21).

Hassenkam, T., Fantner, G.E., Cutroni, J.A., Weaver, J.C., Morse, D.E., Hansma, P.K. (2004) High-resolution AFM imaging of intact and fractured trabecular bone. *Bone*. **35**(1), 4–10.

Heath, D.E., Lannutti, J.J., Cooper, S.L. (2010) Electrospun scaffold topography affects endothelial cell proliferation, metabolic activity, and morphology. *Journal of Biomedical Materials Research Part A*. **94A**(4), 1195–1204.

Höhm, S., Rosenfeld, A., Krüger, J., Bonse, J. (2012) Femtosecond laser-induced periodic surface structures on silica. *Journal of Applied Physics*. **112**(1).

Howat, W., Barabás, T., Holmes, J., Holgate, S. (2002) Distribution of basement membrane pores in bronchus revealed by microscopy following epithelial removal. . **139**(3), 137–45.

Howat, W., Holmes, J., Holgate, S. (2001) Basement membrane pores in human bronchial epithelium: a conduit for infiltrating cells? **158**(2), 673–80.

Hsu, S.-H., Chen, C.-Y., Lu, P.S., Lai, C.-S., Chen, C.-J. (2005) Oriented Schwann cell growth on microgrooved surfaces. *Biotechnology and Bioengineering*. **92**(5), 579–588.

Huttenlocher, A., Ginsberg, M.H., Horwitz, A.F. (1996) Modulation of cell migration by integrin-mediated cytoskeletal linkages and ligand-binding affinity. *The Journal of Cell Biology*. **134**(6), 1551–1562.

Huttenlocher, A., Horwitz, A.R. (2011) Integrins in Cell Migration. *Cold Spring Harbor Perspectives in Biology*. **3**.

Hwang, S.Y., Kwon, K.W., Jang, K.-J., Park, M.C., Lee, J.S., Suh, K.Y. (2010) Adhesion Assays of Endothelial Cells on Nanopatterned Surfaces within a Microfluidic Channel. *Analytical Chemistry*. **82**(7), 3016–3022.

Inoue, T., Croce, K., Morooka, T., Sakuma, M., Node, K., Simon, D.I. (2011) Vascular Inflammation and Repair: Implications for Re-Endothelialization, Restenosis, and Stent Thrombosis. *JACC: Cardiovascular Interventions*. **4**(10), 1057–1066.

International consensus (2001) Acellular matrices for the treatment of wounds. An expert working group review. *London: Wounds International*.

Jansen, H., Gardeniers, H., Boer, M. de, Elwenspoek, M., Fruitman, J. (1996) A survey on the reactive ion etching of silicon in microtechnology. *Journal of Micromechanics and Microengineering*. **6**.

Jeun, J.-P., Kim, Y.-H., Lim, Y.-M., Choi, J.-H., Jung, C.-H., Kang, P.-H., Nho, Y.-C. (2007) Electrospinning of Poly(L-lactide-co-D, L-lactide). *Journal of Industrial and Engineering Chemistry*. **13**(4), 592–596.

Jiang, H., Fang, D., Hsiao, B.S., Chu, B., Chen, W. (2004) Optimization and Characterization of Dextran Membranes Prepared by Electrospinning. *Biomacromolecules*. **5**(2), 326–333.

Johnson, B.D., Mather, K.J., Wallace, J.P. (2011) Mechanotransduction of shear in the endothelium: Basic studies and clinical implications. *Vascular Medicine*. **16**(5), 365–377.

Karuri, N.W., Liliensiek, S., Teixeira, A.I., Abrams, G., Campbell, S., Nealey, P.F., Murphy, C.J. (2004) Biological length scale topography enhances cell-substratum adhesion of human corneal epithelial cells. *Journal of cell science*. **117**(Pt 15), 3153–3164.

Kawabe, T., MacCallum, D., Lillie, J. (1985) Variation in basement membrane topography in human thick skin. *The Anatomical record*. **211**(2), 142–148.

Kemp, P. (2006) History of regenerative medicine: looking backwards to move forwards. *Regenerative Medicine*. **1**(5), 653–69.

Kim, H., Jiao, A., Hwang, N., Kim, M., Kang, D.H., Kim, D.-H., Suh, K.-Y. (2013) Nanotopography-guided tissue engineering and regenerative medicine. *Advanced drug delivery reviews*. **65**(4), 536–558.

King, S.B. (1996) Angioplasty From Bench to Bedside to Bench. *Circulation*. **93**(9), 1621–1629.

Klintmalm, G. (2004) The history of organ transplantation in the Baylor Health Care System.

Koski, A., Yim, K., Shivkumar, S. (2004) Effect of molecular weight on fibrous PVA produced by electrospinning. *Materials Letters*. **58**(3–4), 493–497.

Laflamme, K., Roberge, C.J., Labonté, J., Pouliot, S., D'Orléans-Juste, P., Auger, F.A., Germain, L. (2005) Tissue-Engineered Human Vascular Media With a Functional Endothelin System. *Circulation*. **111**(4), 459–464.

Langheinrich, D., Yslas, E., Broglia, M., Rivarola, V., Acevedo, D., Lasagni, A. (2012) Control of cell growth direction by direct fabrication of periodic micro- and submicrometer arrays on polymers. *Journal of Polymer Science Part B: Polymer Physics*. **50**(6), 415–422.

Lee, J.., Gotlieb, A.. (2003) Understanding the role of the cytoskeleton in the complex regulation of the endothelial repair. *Histology and Histopathology*. **18**(3).

Lee, K.S., Yang, D.Y., Park, S.H., Kim, R.H. (2006) Recent developments in the use of two-photon polymerization in precise 2D and 3D microfabrications. *Polymers for Advanced Technologies*. **17**(2), 72.

Lee, S.W., Kim, S.Y., Rhyu, I.C., Chung, W.Y., Leesungbok, R., Lee, K.W. (2009) Influence of microgroove dimension on cell behavior of human gingival fibroblasts cultured on titanium substrata. *Clinical Oral Implants Research*. **20**.

Leitz, K.H., Redlingshöfer, B., Reg, Y., Otto, A., Schmidt, M. (2011) Metal Ablation with Short and Ultrashort Laser Pulses. *Lasers in Manufacturing 2011 - Proceedings of the Sixth International WLT Conference on Lasers in Manufacturing*. **12, Part B**(0), 230–238.

Lenhert, S., Meier, M.-B., Meyer, U., Chi, L., Wiesmann, H.P. (2005) Osteoblast alignment, elongation and migration on grooved polystyrene surfaces patterned by Langmuir–Blodgett lithography. *Biomaterials*. **26**(5), 563–570.

Li, Y., Zhu, Y., Yu, H., Chen, L., Liu, Y. (2012) Topographic characterization and protein quantification of esophageal basement membrane for scaffold design reference in tissue engineering. *Journal of biomedical materials research. Part B, Applied biomaterials*. **100**(1), 265–273.

Liu, H., Slamovich, E.B., Webster, T.J. (2006) Increased osteoblast functions among nanophase titania/poly(lactide-co-glycolide) composites of the highest nanometer surface roughness. *Journal of Biomedical Materials Research Part A*. **78A**(4), 798–807.

Lott, J., de Carvalho, P.H., Assis, D., de Goes, A.M. (2013) Innovative Strategies for Tissue Engineering. In R. Pignatello, ed. *Advances in Biomaterials Science and Biomedical Applications*. InTech.

Lötters, J.C., Olthuis, W., Veltink, P.H., Bergveld, P. (1997) The mechanical properties of the rubber elastic polymer polydimethylsiloxane for sensor applications. *Journal of Micromechanics and Microengineering*. **7**(3), 145.

Lu, H., Cho, S.-H., Lee, J., Cauller, L., Ortega, R., Hughes, G. (2006) SU8-based micro neural probe for enhanced chronic in-vivo recording of spike signals from regenerated axons. *IEEE Sensors*, 66–69.

Lu, J., Rao, M., MacDonald, N., Khang, D., Webster, T. (2008) Improved endothelial cell adhesion and proliferation on patterned titanium surfaces with rationally designed, micrometer to nanometer features. *Acta biomaterialia*. **4**(1), 192–201.

Mak, K.Y., Li, L., Wong, C.M., Ng, S.M., Leung, C.W., Shi, J., Koon, H.K., Chen, X., Mak, C.S.K., Chan, M.M., Pong, P.W.T. (2013) Quantitative analysis of hepatic cell morphology and migration in response to nanoporous and microgrooved surface structures. *Microelectronic Engineering*. **111**(0), 396–403.

Maltzman, J., Koretzky, G. (2003) Azathioprine: old drug, new actions. *Journal of Clinical Investigation*. **111**(8), 1122–1124.

Martin, G.R., Timpl, R. (1987) Laminin and other Basement Membrane Components. *Annual Review of Cell Biology*. **3**(1), 57–85.

Maruo, S., Inoue, H. (2006) Optically driven micropump produced by three-dimensional two-photon microfabrication. *Applied Physics Letters*. **89**(14), 144101–144101–3.

Marx, S.O., Totary-Jain, H., Marks, A.R. (2011) Vascular Smooth Muscle Cell Proliferation in Restenosis. *Circulation: Cardiovascular Interventions*. **4**, 104–111.

Matsuda, S., Koyasu, S. (2000) Mechanisms of action of cyclosporine. *Immunopharmacology*. **47**(2–3), 119–125.

Matsumura, G., Hibino, N., Ikada, Y., Kurosawa, H., Shin'oka, T. (2003) Successful application of tissue engineered vascular autografts: clinical experience. *Biomaterials*. **24**(13), 2303–2308.

Matsuzaka, K., Walboomers, X., De, J. (1999) The effect of poly-L-lactic acid with parallel surface micro groove on osteoblast-like cells in vitro.

Matsuzaka, K., Walboomers, X.F., Yoshinari, M., Inoue, T., Jansen, J.A. (2003) The attachment and growth behavior of osteoblast-like cells on microtextured surfaces. *Biomaterials*. **24**(16), 2711–9.

McGill, G., Shimamura, A., Bates, R.C., Savage, R.E., Fisher, D.E. (1997) Loss of Matrix Adhesion Triggers Rapid Transformation-Selective Apoptosis in Fibroblasts. *The Journal of Cell Biology*. **138**(4), 901–911.

McMurray, R., Dalby, M.J., Gadegaard, N. (2011) Nanopatterned surfaces for biomedical applications. *Trends in Materials Science*, 307–513.

Meredith Jr, J.E., Schwartz, M.A. (1997) Integrins, adhesion and apoptosis. *Trends in Cell Biology*. **7**(4), 146–150.

Michaels, A.D. (2002) Angioplasty Versus Bypass Surgery for Coronary Artery Disease. *Circulation*. **106**, 187–190.

Miller, C., Shanks, H., Witt, A., Rutkowski, G., Mallapragada, S.K. (2001) Oriented Schwann cell growth on micropatterned biodegradable polymer substrates. *Biomaterials*. **22**(11), 1263–1269.

Mit-uppatham, C., Nithitanakul, M., Supaphol, P. (2004) Ultrafine Electrospun Polyamide-6 Fibers: Effect of Solution Conditions on Morphology and Average Fiber Diameter. *Macromolecular Chemistry and Physics*. **205**(17), 2327–2338.

Morgan, J., Wood, J., Shah, N., Hughbanks, M., Russell, P., Barakat, A., Murphy, C. (2012) Integration of basal topographic cues and apical shear stress in vascular endothelial cells. *Biomaterials*. **33**(16), 4126–4135.

Motlagh, D., Hartman, T.J., Desai, T.A., Russell, B. (2003) Microfabricated grooves recapitulate neonatal myocyte connexin43 and N-cadherin expression and localization. *Journal of Biomedical Materials Research Part A*. **67A**(1), 148–157.

Mussig, E., Schulz, S., Spatz, J.P., Ziegler, N., Tomakidi, P., Steinberg, T. (2010) Soft micropillar interfaces of distinct biomechanics govern behaviour of periodontal cells. *European Journal of Cell Biology*. **89**(4), 315–325.

Nayler, W. (1995) Atherosclerosis and endothelial damage: A brief overview. *Cardiovascular Drugs and Therapy*. **9**(1), 25–30.

Nemani, K., Moodie, K., Brennick, J., Su, A., Gimi, B. (2013) In vitro and in vivo evaluation of SU-8 biocompatibility. *Materials science & engineering. C, Materials for biological applications*. **33**(7), 4453–4459.

Oakes, P.W., Beckham, Y., Stricker, J., Gardel, M.L. (2012) Tension is required but not sufficient for focal adhesion maturation without a stress fiber template. *The Journal of Cell Biology*. **196**(3), 363–374.

Obata, K., El-Tamer, A., Koch, L., Hinze, U., Chichkov, B.N. (2013) High-aspect 3D two-photon polymerization structuring with widened objective working range (WOW-2PP). *Light Sci Appl*. **2**, e116.

Oberpenning, F., Meng, J., Yoo, J.J., Atala, A. (1999) De novo reconstitution of a functional mammalian urinary bladder by tissue engineering. *Nat Biotech*. **17**(2), 149–155.

Ovsianikov, A., Viertl, J., Chichkov, B., Oubaha, M., MacCraith, B., Sakellari, I., Giakoumaki, A., Gray, D., Vamvakaki, M., Farsari, M., Fotakis, C. (2008) Ultra-Low Shrinkage Hybrid Photosensitive Material for Two-Photon Polymerization Microfabrication. *ACS Nano*. **2**(11), 2257–2262.

Owen, G.R., Jackson, J., Chehroudi, B., Burt, H., Brunette, D.M. (2005) A PLGA membrane controlling cell behaviour for promoting tissue regeneration. *Dedicated to Canadian Biomaterials Research Dedicated to Canadian Biomaterials Research*. **26**(35), 7447–7456.

Palecek, S.P., Loftus, J.C., Ginsberg, M.H., Lauffenburger, D.A., Horwitz, A.F. (1997) Integrin-ligand binding properties govern cell migration speed through cell-substratum adhesiveness. *Nature*. **385**(6616), 537–540.

Pan, Z., Yan, C., Peng, R., Zhao, Y., He, Y., Ding, J. (2012) Control of cell nucleus shapes via micropillar patterns. *Biomaterials*. **33**(6), 1730–1735.

Peckham, M., Miller, G., Wells, C., Zicha, D., Dunn, G.A. (2001) Specific changes to the mechanism of cell locomotion induced by overexpression of (β)-actin. *Journal of Cell Science*. **114**(7), 1367–1377.

Potter, C.M.F., Lundberg, M.H., Harrington, L.S., Warboys, C.M., Warner, T.D., Berson, R.E., Moshkov, A.V., Gorelik, J., Weinberg, P.D., Mitchell, J.A. (2011) Role of Shear Stress in Endothelial Cell Morphology and Expression of

Cyclooxygenase Isoforms. *Arteriosclerosis, Thrombosis, and Vascular Biology*. **31**(2), 384–391.

Price, R.L., Ellison, K., Haberstroh, K.M., Webster, T.J. (2004) Nanometer surface roughness increases select osteoblast adhesion on carbon nanofiber compacts. *Journal of Biomedical Materials Research Part A*. **70A**(1), 129–138.

Re, F., Zanetti, A., Sironi, M., Polentarutti, N., Lanfrancone, L., Dejana, E., Colotta, F. (1994) Inhibition of anchorage-dependent cell spreading triggers apoptosis in cultured human endothelial cells. *The Journal of Cell Biology*. **127**(2), 537–546.

Rebollar, E., Frischauf, I., Olbrich, M., Peterbauer, T., Hering, S., Preiner, J., Hinterdorfer, P., Romanin, C., Heitz, J. (2008) Proliferation of aligned mammalian cells on laser-nanostructured polystyrene. *Biomaterials*. **29**(12), 1796 – 1806.

Recknor, J.B., Recknor, J.C., Sakaguchi, D.S., Mallapragada, S.K. (2004) Oriented astroglial cell growth on micropatterned polystyrene substrates. *Biomaterials*. **25**(14), 2753–2767.

Rensen, S.S.M., Doevendans, P.A.F.M., van Eys, G.J.J.M. (2007) Regulation and characteristics of vascular smooth muscle cell phenotypic diversity. *Netherlands Heart Journal*. **15**(3), 100–108.

Rho, J., Ashman, R., Turner, C. (1993) Young's modulus of trabecular and cortical bone material: ultrasonic and microtensile measurements. . **26**(2), 111–9.

Ribeiro-Resende, V.T., Koenig, B., Nichterwitz, S., Oberhoffner, S., Schlosshauer, B. (2009) Strategies for inducing the formation of bands of Büngner in peripheral nerve regeneration. *Biomaterials*. **30**(29), 5251 – 5259.

Roure, O. du, Saez, A., Buguin, A., Austin, R.H., Chavrier, P., Siberzan, P., Ladoux, B. (2005) Force mapping in epithelial cell migration. *Proc Natl Acad Sci U.S.A.* **102**(7), 2390–2395.

Ruoslahti, E., Reed, J.C. (1994) Anchorage dependence, integrins, and apoptosis. *Cell*. **77**(4), 477–478.

Sarkar, S., Dadhania, M., Rourke, P., Desai, T.A., Wong, J.Y. (2005) Vascular tissue engineering: microtextured scaffold templates to control organization of vascular smooth muscle cells and extracellular matrix. *Acta Biomaterialia*. **1**(1), 93–100.

Schaefer, D., Martin, I., Jundt, G., Seidel, J., Heberer, M., Grodzinsky, A., Bergin, I., Vunjak-Novakovic, G., Freed, L.E. (2002) Tissue-engineered composites for the repair of large osteochondral defects. *Arthritis & Rheumatism*. **46**(9), 2524–34.

Semak, V.V., Matsunawa, A. (2014) Modeling of transport phenomena and solidification cracking in laser spot bead-on-plate welding of AA6063-T6 alloy. Part I—the mathematical model. *The International Journal of Advanced Manufacturing Technology*.

Seo, C.H., Jeong, H., Feng, Y., Montagne, K., Ushida, T., Suzuki, Y., Furukawa, K.S. (2014) Micropit surfaces designed for accelerating osteogenic differentiation of murine mesenchymal stem cells via enhancing focal adhesion and actin polymerization. *Biomaterials*. **35**(7), 2245–2252.

Serbin, J., Egbert, A., Ostendorf, A., Chichkov, B.N., Houbertz, R., Domann, G., Schulz, J., Cronauer, C., Frahlich, L., Popall, M. (2003) Femtosecond laser-induced two-photon polymerization of inorganic organic hybrid materials for applications in photonics. *Optics Letters*. **28**(5), 301–303.

Shinoka, T., Breuer, C., Tanel, R., Zund, G., Miura, T., Ma, P., Langer, R., Vacanti, J., Mayer, J. (1995) Tissue engineering heart valves: valve leaflet replacement study in a lamb model. *The Annals of thoracic surgery*. **60**(6), 513–516.

Sipe, J.E., Young, J.F., Preston, J.S., van Driel, H.M. (1983) Laser-induced periodic surface structure. I. Theory. *Physical Review B*. **27**(2), 1141–1154.

Song, J.J., Guyette, J.P., Gilpin, S.E., Gonzalez, G., Vacanti, J.P., Ott, H.C. (2013) Regeneration and experimental orthotopic transplantation of a bioengineered kidney. *Nat Med*. **19**(5), 646–651.

Sprague, E., Tio, F., Ahmed, S., Granada, J., Bailey, S. (2012) Impact of parallel micro-engineered stent grooves on endothelial cell migration, proliferation, and function: an in vivo correlation study of the healing response in the coronary swine model. *Circulation. Cardiovascular interventions*. **5**(4), 499–507.

Stankevicius, E., Gertus, T., Rutkauskas, M., Gedvilas, M., Raciukaitis, G., Gadonas, R., Smilgevicius, V., Malinauskas, M. (2012) Fabrication of micro-tube arrays in photopolymer SZ2080 by using three different methods of a direct laser polymerization technique. *Journal of Micromechanics and Microengineering*. **22**(6), 065022.

Stay, J.L., Burrow, G.M., Gaylord, T.K. (2011) Three-beam interference lithography methodology. *Review of Scientific Instruments*. **82**(2).

Straube, W., Tanaka, E. (2006) Reversibility of the differentiated state: regeneration in amphibians. . **30**(10), 743–55.

Su, W.-T., Chu, I.-M., Yang, J.-Y., Lin, C.-D. (2006) The geometric pattern of a pillared substrate influences the cell-process distribution and shapes of fibroblasts. *Micron*. **37**(8), 699–706.

Su, W.-T., Liao, Y.-F., Lin, C.-Y., Li, L.-T. (2010) Micropillar substrate influences the cellular attachment and laminin expression. *Journal of Biomedical Materials Research Part A*. **93A**(4), 1463–1469.

Su, W.-T., Liao, Y.-F., Wu, T.-W., Wang, B.-J., Shih, Y.-Y. (2013) Microgrooved patterns enhanced PC12 cell growth, orientation, neurite elongation, and neuritogenesis. *Journal of Biomedical Materials Research Part A*. **101A**(1), 185–194.

Tan, B., Venkatakrishnan, K. (2006) A femtosecond laser-induced periodical surface structure on crystalline silicon. *Journal of Micromechanics and Microengineering*. **16**(5), 1080.

Tan, Q., Steiner, R., Hoerstrup, S., Weder, W. (2006) Tissue-engineered trachea: History, problems and the future. *European Journal of Cardio-Thoracic Surgery*. **30**(5), 782–6.

Taylor, G. (1969) Electrically Driven Jets. *Proceedings of the Royal Society of London. A. Mathematical and Physical Sciences*. **313**(1515), 453–475.

Teirstein, P., Fish, R., Colombo, A. (1994) A randomized comparison of coronary-stent placement and balloon angioplasty in the treatment of coronary artery disease. *The New England journal of medicine*. **331**, 496–501.

Teixeira, A.I., Abrams, G.A., Bertics, P.J., Murphy, C.J., Nealey, P.F. (2003) Epithelial contact guidance on well-defined micro- and nanostructured substrates. *Journal of cell science*. **116**(Pt 10), 1881–1892.

Thakar, R., Cheng, Q., Patel, S., Chu, J., Nasir, M., Liepmann, D., Komvopoulos, K., Li, S. (2009) Cell-shape regulation of smooth muscle cell proliferation. *Biophysical journal*. **96**(8), 3423–3432.

Thakar, R.G., Ho, F., Huang, N.F., Liepmann, D., Li, S. (2003) Regulation of vascular smooth muscle cells by micropatterning. *Biochemical and Biophysical Research Communications*. **307**(4), 883–890.

Tiwari, A., Salacinski, H.J., Hamilton, G., Seifalian, A.M. (2001) Tissue Engineering of Vascular Bypass Grafts: Role of Endothelial Cell Extraction. *European journal of vascular and endovascular surgery : the official journal of the European Society for Vascular Surgery*. **21**(3), 193–201.

Townsend, N., Wickramasinghe, K., Bhatnagar, P., Smolina, K., Nicholas, M., Leal, J., Luengo-Fernandez, R., Rayner, M. (2012) Coronary heart disease statistics: A compendium of health statistics. *British Heart Foundation*.

Ulerich, J.P., Ionescu, L.C., Chen, J., Soboyejo, W.O., Arnold, C.B. (2007) Modifications of Ti-6Al-4V surfaces by direct-write laser machining of linear grooves. In SPIE Proceedings, pp. 645819–645819–10.

Uttayarat, P., Chen, M., Li, M., Allen, F., Composto, R., Lelkes, P. (2008) Microtopography and flow modulate the direction of endothelial cell migration. *American journal of physiology. Heart and circulatory physiology*. **294**(2), 1027–1035.

Uttayarat, P., Toworfe, G., Dietrich, F., Lelkes, P., Composto, R. (2005) Topographic guidance of endothelial cells on silicone surfaces with micro- to nanogrooves: orientation of actin filaments and focal adhesions. *Journal of biomedical materials research. Part A*. **75**(3), 668–680.

Vacanti, C. (2006) The history of tissue engineering. *Journal of Cellular and Molecular Medicine*. **1**.

Vogel, R.A. (1997) Coronary risk factors, endothelial function, and atherosclerosis: A review. *Clinical Cardiology*. **20**(5), 426–432.

Walboomers, X.F., Monaghan, W., Curtis, A.S.G., Jansen, J.A. (1999) Attachment of fibroblasts on smooth and microgrooved polystyrene. *Journal of Biomedical Materials Research*. **46**(2), 212–220.

Wang, J.-C., Yang, G., Li, Z. (2005) Controlling Cell Responses to Cyclic Mechanical Stretching. *Annals of Biomedical Engineering*. **33**(3), 337–342.

Wang, L., Carrier, R.L. (2011) Biomimetic topography: bioinspired cell culture substrates and scaffolds. *Advances in Biomimetics*. **21**, 454–472.

Wanzenboeck, H.., Waid, S. (2011) 'Focused ion beam lithography,' in Recent Advances in Nanofabrication Techniques and Applications. *InTech*.

Wasserman, S.M., Mehraban, F., Komuves, L.G., Yang, R.-B., Tomlinson, J.E., Zhang, Y., Spriggs, F., Topper, J.N. (2002) Gene expression profile of human endothelial cells exposed to sustained fluid shear stress. *Physiological Genomics*. **12**(1), 13–23.

Watson, C.J.E., Dark, J.H. (2011) Organ transplantation: historical perspective and current practice. *British Journal of Anaesthesia*. **108**(1), 29–42.

De Waure, C., Lauret, G.-J., Ricciardi, W., Ferket, B., Teijink, J., Spronk, S., Myriam Hunink, M.G. (2013) Lifestyle Interventions in Patients with Coronary Heart Disease: A Systematic Review. *American Journal of Preventive Medicine*. **45**(2), 207–216.

Webster, T.J., Ejiofor, J.U. (2004) Increased osteoblast adhesion on nanophase metals: Ti, Ti6Al4V, and CoCrMo. *Biomaterials*. **25**(19), 4731–4739.

Weiss, P. (1945) Experiments on cell and axon orientation in vitro: The role of colloidal exudates in tissue organization. *Journal of Experimental Zoology*. **100**(3), 353–386.

Weiss, P. (1934) In vitro experiments on the factors determining the course of the outgrowing nerve fiber. *Journal of Experimental Zoology*. **68**(3), 393–448.

Whitesides, G.M., Ostuni, E., Takayama, S., Jiang, X., Ingber, D.E. (2001) Soft lithography in biology and biochemistry. *Annual Review of Biomedical Engineering*. **3**(1), 335–373.

Windecker, S., Meier, B. (2007) Late Coronary Stent Thrombosis. *Circulation*. **116**(17), 1952–1965.

Wong, K.V., Hernandez, A. (2012) A review of additive manufacturing. . **2012**.

Wong, M.K., Gotlieb, A.I. (1986) Endothelial cell monolayer integrity. I. Characterization of dense peripheral band of microfilaments. *Arteriosclerosis, Thrombosis, and Vascular Biology*. **6**(2), 212–219.

Wu, L., Zhong, Y.., Chan, C.., Wong, K.., Wang, G.. (2005) Fabrication of large area two- and three-dimensional polymer photonic crystals using single refracting prism holographic lithography. *Applied Physics Letters*. **86**(24).

Wu, S., Serbin, J., Gu, M. (2006) Two-photon polymerisation for three-dimensional micro-fabrication. *Journal of Photochemistry and Photobiology A: Chemistry*. **181**.

Wystrychowski, W., Cierpka, L., Zagalski, K., Garrido, S., Dusserre, N., Radochonski, S., McAllister, T.N., L'heureux, N. (2011) Case study: first implantation of a frozen, devitalized tissue-engineered vascular graft for urgent hemodialysis access. *The Journal of Vascular Access*. **12**(1), 67–70.

Xia, Y., Whitesides, G. (1998) Soft Lithography. *Angewandte Chemie International Edition*. **37**, 550–575.

Yamato, M., Okano, T. (2004) Cell sheet engineering. *Maetrialstoday*. **7**(5), 42–47.

Yang, W., Bricchi, E., Kazansky, P.G., Bovatsek, J., Arai, A.Y. (2006) Self-assembled periodic sub-wavelength structures by femtosecond laser direct writing. *Optics Express*. **14**(21), 10117–10124.

Yao, L., Wang, S., Cui, W., Sherlock, R., O'Connell, C., Damodaran, G., Gorman, A., Windebank, A., Pandit, A. (2009) Effect of functionalized micropatterned PLGA on guided neurite growth. *Acta Biomaterialia*. **5**(2), 580–588.

Yi, T., Li, L., Kim, C.-J. (2000) Microscale material testing of single crystalline silicon: process effects on surface morphology and tensile strength. *Sensors and Actuators A: Physical*. **83**(1–3), 172–178.

Yim, E., Reaon, R., Pang, S., Yee, A., Chen, C., Leong, K. (2005) Nanopattern-induced changes in morphology and motility of smooth muscle cells. *Biomaterials*. **26**.

Yoshinari, M., Matsuzaka, K., Inoue, T., Oda, Y., Shimono, M. (2003) Effects of multigrooved surfaces on fibroblast behavior. *Journal of Biomedical Materials Research Part A*. **65A**(3), 359–368.

Yu, F., Li, P., Shen, H., Mathur, S., Lehr, C.-M., Bakowsky, U., Mücklich, F. (2005) Laser interference lithography as a new and efficient technique for micropatterning of biopolymer surface. *Biomaterials*. **26**(15), 2307 – 2312.

Yurchenco, P.. (2011) Basement Membranes: Cell Scaffoldings and Signaling Platforms. *Cold Spring Harbor Perspectives in Biology*. **3**(2).

Zhao, X., Xia, Y., Whitesides, G. (1997) Soft lithographic methods for nano-fabrication. . (7), 1069–1074.

Ziaie, B., Baldi, A., Atashbar, M. (2010) Introduction to Micro-/Nanofabrication. In B. Bhushan, ed. *Springer Handbook of Nanotechnology*. Springer Berlin Heidelberg, pp. 231–269.

Zorlutuna, P., Annabi, N., Camci-Unal, G., Nikkhah, M., Cha, J.M., Nichol, J.W., Manbachi, A., Bae, H., Chen, S., Khademhosseini, A. (2012) Microfabricated Biomaterials for Engineering 3D Tissues. *Advanced Materials*. **24**(14), 1782–1804.

Appendices

Appendix 1

Table A1.2. HAM F'12 Medium in 37^0C Data

Falling time (s)	Water mass (g)
138	4.835
139.2	5.088
135.6	4.800
Average: 137.6	Average: 4.907/5ml

Density of water p

$$Density\ p = \left(\frac{4.907g}{5ml}\right) * 1000$$

$$Density\ p = 981.4\ kg/m^3$$

Dynamic Viscosity equation for water in 37^0C calculation

$$\eta = Cpt$$

$$\eta = 5.4x10^{-9}\left(\frac{981.4kg}{m^3}\right) * (137.6s)$$

$$\eta = 7.29x10^{-9}\ kg/m.s$$

Convert kg/m.s to dyne/cm^2

$$1\frac{kg}{m}.s = 98.066\ dyne/cm^2$$

$$\frac{Dyne}{cm^2} = 7.29x10^{-9}\frac{kg}{m}.s * 98.066$$

Dynamic viscosity (η) of Ham F'12 at 37^0C is 0.07 dyne/cm^2

Dynamic viscosity (η) of DMEM at 37^0C is 0.083 dyne/cm^2

(Live cell imaging techniques to study T cell trafficking across the blood-brain barrier in vitro and in vivo)

Ibidi µ-slide $1^{0.4}$ Luer shear stress equation

$$\tau\left[\frac{dyne}{cm^2}\right] = \eta\left[\frac{dyne}{cm^2}\right] * 131.6\Phi\left[\frac{ml}{min}\right]$$

$\tau = Shear\ stress, \eta = medium\ viscosity, \Phi = (flow\ rate)$

$$15\left[\frac{dyne}{cm^2}\right] = 0.07\left[\frac{dyne}{cm^2}\right] * 131.6\Phi\left[\frac{ml}{min}\right]$$

$$15\left[\frac{dyne}{cm^2}\right] = 9.212 * \Phi\left[\frac{ml}{min}\right]$$

$$\Phi\left[\frac{ml}{min}\right] = \frac{15\left[\frac{dyne}{cm^2}\right]}{9.212\left[\frac{dyne}{cm^2}\right]}$$

$$\boldsymbol{\Phi = 1.63 ml/min}$$

Ibidi µ-slide $1^{0.6}$ Luer shear stress equation

$$\tau\left[\frac{dyne}{cm^2}\right] = \eta\left[\frac{dyne}{cm^2}\right] * 60.1\Phi\left[\frac{ml}{min}\right]$$

$$15\left[\frac{dyne}{cm^2}\right] = 0.07\left[\frac{dyne}{cm^2}\right] * 60.1\left[\frac{ml}{min}\right]$$

$$15\left[\frac{dyne}{cm^2}\right] = 4.207 * \Phi\left[\frac{ml}{min}\right]$$

$$\Phi\left[\frac{ml}{min}\right] = \frac{15\left[\frac{dyne}{cm^2}\right]}{4.207\left[\frac{dyne}{cm^2}\right]}$$

$$\boldsymbol{\Phi = 3.57 ml/min}$$

Table A1.2. The responses of different cell lines on different types of surface topography

Feature Type	Ref.	Fabrication technique	Material	Feature dimension and frequency	Cell type	Cellular Responses
Cylindrical micropillars	(Su *et al.*, 2010)	• Photolithography • Si anisotropic dry etching techniques	Silicon	1µm in diameter 9µm repeat spacing between pillars and 1, 5, and 10µm in height.	Mouse bone marrow stromal fibroblasts (M2-10B4)	• For 1µm height pillar structure, the fibroblasts spread arbitrarily and bridged the 1µm high pillars. • For 5µm height pillar structure, the fibroblasts by passed the pillar, and grew into the intervals, embraced the surrounding pillars, appeared thicker • For 10µm height pillar structure, the pillar protruded through cell membrane, and cellular processes spread in three different directions. The highest pillars were strong mechanical barriers

						that restricted cells from spreading.

Cylindrical micropillars	(Su *et al.*, 2006)	• Photolithography • Si anisotropic etching techniques	Silicon	1µm in diameter. 3µm repeat spacing and 1, 5, and 10µm in heights	Mouse bone marrow stromal fibroblasts	• Fibroblasts immobilized in situ by several pillars that visibly protruded through, but did not pierce, the cell bodies. • The cytoplasm migrated outward with long straight lamella along the interval of the pillars and formed several discrete attachment zones at their side walls – the value of their form index (FI) was as high as 35 – which altered the cellular shape entirely. • Most of the cells interacted with the pillar substrate by spreading preferentially in a particular direction, but some of them had the ability to undergo coincident two-direction (x and y) migration. • Fibroblast's behaviour variation was gradually in proportion to the pillar height of substrate.

Cylindrical micropillars	(Frey *et al.*, 2006)	Strong electric field	Polystyrene cast of PDMS.	10.30µm diameter. Average 1.78µm in height. 15.67µm repeats spacing in center-center spacing.	Primary mouse embryonic fibroblast cells (NIH 3T3).	• 3T3 cells on pillar substrates showed a more branched shape, an increased linear speed, and a decreased directional stability. These responses may be attributed to stabilization of cell adhesion on pillars coupled to myosin II-dependent contractions toward pillars. • Focal adhesion kinase is essential for the responses to substrate topography.
Cylindrical micropillars	(Ghibaudo *et al.*, 2009)	Conventional photolithography	PDMS cast of Silicon wafer.	5 to 10µm in diameter. 2 to 10µm in height. 5 to 10µm repeat spacing from edge to edge of the pillars.	Primary mouse embryonic fibroblast cells (NIH 3T3).	• Substrate topography affects cell shape and migration by modifying cell-to-substrate interactions. • Cells on micropillar substrates exhibit more elongated and branched shapes with fewer actin stress fibers compared with cells on flat surfaces. • Migration paths in various environments, different mechanisms of cell migration, including a persistent type of migration that depends on the organization of the topographical features. These responses can be

						attributed to a spatial reorganization of the actin cytoskeleton due to physical constraints and a preferential formation of focal adhesions on the micropillars, with an increased lifetime compared to that observed on flat surfaces. • By changing myosin II activity, the actomyosin contractility is essential in the cellular response to micron-scale topographic signals
Soft cylindrical micropillar	(Mussig *et al.*, 2010)	• UV light • 400W mercury lamp • baking (for production of a range of E-moduli)	PDMS cast of silicon wafer and coated with fibronectin.	5µm in diameter. 15µm in height. 5, 7, 9 and 11µm repeat spacing and elasticity moduli (E-moduli) of 0.6, 1.0 and 3.5 Mega Pascal.	• Gingival-Fibroblasts • Periodontal-Ligament-Fibroblasts • Osteoblasts from the Alveolar Bone	• Deterioration of regular cell morphology with increasing pillar distance, independent from pillar elasticity and cell type. • Analysis of collagen gene expression demonstrates interdependency to the elasticity and the micro-textured of the extracellular environment in all cell types under study. • Biomechanics of the extracellular environment govern tissue-specific cell behaviour in different periodontal cell types.

Cylindrical micropillar	(Roure *et al.*, 2005)	• Conventional photolithography • Deep etching process (Bosch process) • plasma treatment • Reverse microcontact printing (μFSA).	PDMS cast of silicon wafer and coated with fibronectin.	1 to 2μm in diameter. 3 to 8μm in height. Mechanical stiffness of the pillars from 0.47 to 174nN/μm	Differentiated Madin-Darby canine kidney (MDCK) epithelial cells	• The maximum intensity of the forces is localized on the edge of the epithelia. • Hepatocyte growth factor promotes cell motility and induces strong scattering activity of MDCK cells. • Compare forces generated by MDCK cells in subconfluent epithelia versus isolated cells after hepatocyte growth factor treatment. Maximal-traction stresses at the edge of a monolayer correspond to higher values than those measured for a single cell and may be due to a collective behaviour.
V-shaped Microgroove	(Brunette, 1986)	• Photolithography. • Si anisotropic etching techniques.	Titanium-coated silicon wafer. Titanium-coated photoresist-based substrata.	Titanium-coated silicon wafer. Vertical-walled grooves of 5 and 16μm and repeat spacing of 30-220μm.	Epithelial cells (isolated from porcine periodontal ligament).	• The proliferation index (OI) of epithelial cells on every combination of groove depth and width on titanium-coated silicon wafer higher than smooth flat surface. • The orientation index being highest for substrata with groove of the smallest repeats.

			Titanium-coated substrate.	<u>Titanium-coated photoresist-based substrata.</u> Ridge height of ~2µm and gently undulating topology. Repeat spacing of 4.9, 6.6 and 8.3µm. <u>Titanium-coated substrate.</u> ~0.5 deep grooves and repeats spacing of 30 to 112µm.		• The epithelial cells migrated on the direction of the grooves, but some cells crosses over the ridges and descended into the grooves. • Deeper grooves more effective in directing cell locomotion. • Epithelial cells capable of bending around and closely adapting to groove edges. • Epithelial cells did not flatten extensively on 22µm deep v-shaped grooves as on a smooth surface.
V-shape microgroove	(Yoshinari *et al.*, 2003)	Ultraprecision micromachining (using a single crystal diamond).	Polystyrene cast of 18 karat gold alloy multigrooved master die	Macrogrooves had a 50µm ridge width, a 50µm wall width, a 50µm bottom width,	Mouse fibroblast L929 cells	• The fibroblasts on the multigrooved and microgrooved substrates aligned parallel to the surface grooves after 7 days incubation.

				and a 25µm depth. 90-degree V-shaped Microgrooves with a 2µm pitch and 1µm depth cut on trapezoidal macrogrooves.		• The ratios of cellular spreading on the multi- and microgrooved surfaces greater than those on the smooth surfaces. • In contrast to the microgrooved and flat surfaces, a dense extracellular matrix produced along the multigrooves after 21 days of incubation. • Multigrooves can control the orientation of ECM as well as cells and enhance the production of ECM.
Square Microgroove	(Dalton *et al.*, 2001)	Photolithography	Polystyrene cast of silicon wafer. For cell migration polystyrene surface coated with fibronectin.	Microgroove 1 or 5-µm depth. Groove/ridge widths of 1, 2, 5, or 10µm	Bovine corneal epithelial cells	• The migration of a tissue sheet enhanced along the microgrooves, while migration across the microgrooves was inhibited. • Changing the depth of the microgrooves had a greater effect on migration than alteration of the groove/ridge width. • Cellular extensions generally followed the microgroove direction by tracking along the top of the ridges or following the ridge walls.

						• Actin filaments within the basal cell layer of the tissue aligned with the microgrooves. • The basal cell layer of the tissue conformed to the contours of the microgroove following migration. However, the ultrastructure of the tissue above the ridges resembled that of tissue on a flat surface.
Square microgroove	(Charest *et al.*, 2004)	• Hot embossing imprint lithography • Deep reactive ions etch (Bosch Process).	Polymer (not stated) cast of silicon wafer.	Microgrooves approximately 5µm deep. 4µm wide. Periodicity of 34µm.	MC3T3-E1 osteoblasts	• Cell membrane body, cell nucleus, and focal adhesions all strongly aligned with the microgroove, while only the cell body shape changed on the microgrooved surface.
Square microgroove	(Hsu *et al.*, 2005)	• Photolithography. • Si anisotropic etching techniques.	Silicon wafer coated with either collagen type I or laminin.	Grooves depth: 0.5, 1, 1.5 and 3µm. Grooves width and spacing: 10 and 20µm.	Schwann cells (harvested from neo-natal Sprague-Dawley rat pups.	• The percentage of rat Schwann cells alignment increased with increasing grooves depth and width. • 60% of cells aligned on grooves with width/spacing/depth=20/20/1.5µm and coated with laminin, 51% for collagen coated surface and 41%

						for uncoated surface at 24 hours post cell seeding. • The groove depth influenced the Schwann cells orientation. The cell alignment on 20/20/3 µm microgrooved poly(D,Llactide-co-glycolide) 90:10 (PLGA) surfaces transferred from silicon reached 72% at 48 h and 92% at 72 h .Coating this surface with laminin enhanced cell alignment only in short term (67% vs. 62% at 24 h, $P<0.05$). • The cell alignment guided by surface microgrooves was time dependent.
Square microgroove	(Owen *et al.*, 2005)	• Photolithography. • Negative surface impressions. • Sandblasted and acid-etched. •	Epoxy, PLGA and SLA	30µm deep, with sloping walls that met the floor of groove at 125˚. Groove width at 30µm. Ridge width, 25 and 175µm.	Epithelial cells (isolated from porcine periodontal ligament). Osteogenic cells (from newborn rat calvaria).	• Epithelial cells spread on sandblasted-acid-etched after 24 hours but the cell number did not significantly increase after 5 days (cell migration inhibited on this surface). • Osteoblasts cells spread on grooved surface and increase in cell number after 5 days. The cells migrated in the direction of the grooves.

						• The result showed that sandblasted-acid-etched surface inhibited epithelial cell proliferation and migration but grooved surface promote proliferation and directional migration of osteoblast.
Square microgroove	(Lee *et al.*, 2009)	Photolithography	Titanium disks (TiD15, TiD30, and TiD6)	Grooves depth: 3.5µm. Grooves width: 15, 30 and 60µm.	• Human gingival fibroblasts	• The fibroblasts cells descended into the microgrooves of TiD30. • Cells on the ridge edges or in groove corners spindle shaped with abundant filopodia formation toward the acid-etched surface inside the microgrooves thus mimicked the cell shape in three-dimensional (3D) nanoenvironment. • TiD15 significantly increased the cell viability and proliferation compared with the smooth Ti substrata after 72 h of culture. • Up-regulation of fibronectin (FN) and a5 integrin genes observed in cells cultured on TiD15 and TiD30.

						• Gene expression pattern specific to the cells in 3D-matrix culture, such as down-regulation of a-smooth muscle actin gene along with up-regulation of FN and p21 genes, pronounced in cells cultured on TiD30.
Square microgroove	(Wang *et al.*, 2005)	• Photolithography • Si anisotropic etching techniques	Silicon cast of silicon wafer and coated with Pronectin.	Ridge width: 10µm Groove width: 10µm Groove depth: 3µm	Human patellar tendon fibroblasts.	• Fibroblasts cells had polar morphology and aligned along the direction of microgroove regardless of the stretching conditions. • Stretching direction pallerel to the fibroblasts cells orientation induced higher α-SMA (smooth muscle actin) expression than stretching direction perpendiculars to the cells. • Stretching direction perpendicular to the fibroblasts cells induced higher activity levels of phospholipase A_2 ($sPLA_2$) than stretching direction parallel to the cells. • Fibroblasts cell responses to mechanical stretch depend on cell

						orientation to the stretching direction. •
Square microgroove	(Motlagh *et al.*, 2003)	• Photolithography • Si anisotropic etching techniques	Silicon (PDMS) cast of parylene template.	Ridge width: 0-5µm Groove with: 0-5µm Groove depth: 2-5µm	Primary Myocytes (from neonatal rats). Primary cardiac Myocytes.	• Myocytes highly oriented on 5µm depth grooves and compared with randomly oriented cells grown on non-textured surfaces. • Cells on 2µm depth microgrooved surface less oriented. • Connexin 43 and N-cadherin of Myocytes distributed around perimeter of the Myocytes plated on 10x10x5 microgroove surface, similar to the localization found in neonatal. • Connexin43 expression on 5µm depth grooves equal to neonatal heart, whereas it differed on non-textured surface. Groove depth (5µm) and lateral ridge dimensions between grooves (5µm) in could recapitulate connexin43 and N-cadherin expression levels and subcellular localization.

Nanogroove	(Lenhert *et al.*, 2005)	• Langmuir–Blodgett lithography	Polystyrene nano-imprint on silicon wafer	Square Nanogroove. Regular spacing with periodicity of 500nm. Microgroove with 50 and 150nm in depth	Primary osteoblasts (obtained from calf periost).	• The osteoblast cells aligned, elongated and migrated parallel to the grooves. • Cells cultured on the 150 nm deep grooves strongly aligned in the direction of the grooves, 59% of the cells oriented within 30˚ of the groove direction. • Cells cultured on the 50nm deep grooves, 42% of the cells oriented within 30˚ of the grooves. • The elliptical shape of these cell populations did not aligned in the direction of groove.
Nanoripple	(Rebollar *et al.*, 2008)	Linear polarized laser (KrF laser).	Polystyrene	The periodicity of the structures is ca. 200, 270, 340 and 430 nm for the angles of incidence of the laser beam 0, 15, 30 and 45. The respective depth of these structures is	Human embryonic kidney cells (HEK-293) Chinese hamster ovary (CHO-K1) cells.	**HEK-293 Cell Proliferation** • The HEK-293 cells population densities on laser modified PS surface were significantly higher than unmodified PS surface. **HEK-293 Cell Alignment** • HEK-293 cells aligned along the direction of the ripples 24h after seeding. ○ The effect was dependent on the periodicity of the ripples. ○ Periodicity of 200nm, the cells were randomly orientated.

				ca. 40, 70, 80 and 100 nm.		○ Cells aligned along the direction of the ripples after irradiation at 30˚ and 45˚ (*Λ (periodicity)* =340 and 430nm, respectively). ○ Cells aligned along the direction of the ripples in about half of the PS surface after irradiation at 15˚C (*Λ*=270nm). ○ The effect was dependent on the periodicity of the ripples and only observed above a critical minimal value. ○ The cells became confluent after 48h and alignment was not observed any more. • HEK-293 spread freely and randomly orientated on unmodified PS surface. **CHO-K1 Cell Alignment** • CHO-K1 cells aligned along the direction of the ripples already after 6h seeding. ○ The effect observed on samples irradiated at 30 and 45˚ (*Λ*=340 and 430nm, respectively).

						○ CHO-K1 cells aligned weakly along ripples with periodicity of 270nm (irradiated at 15˚). ○ CHO-K1 cells seeded on unmodified PS and PS irradiated at normal incidence were random orientated.

Appendix 2

A2.1 Laser micro-textured ~70µm pillars with spacing ranging from ~9 to 40µm

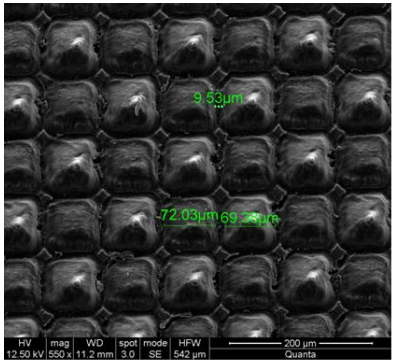

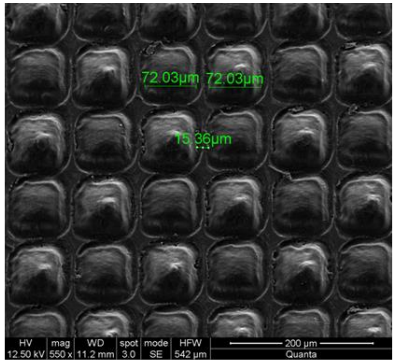

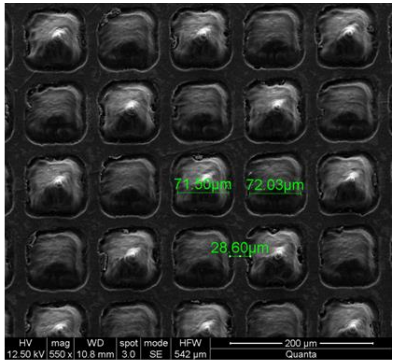

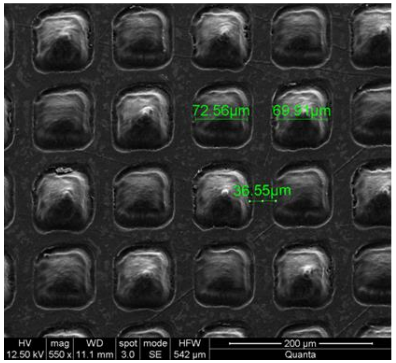

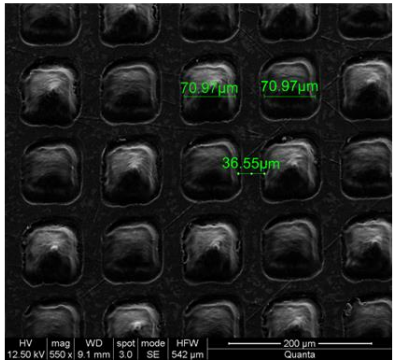

Appendix 3

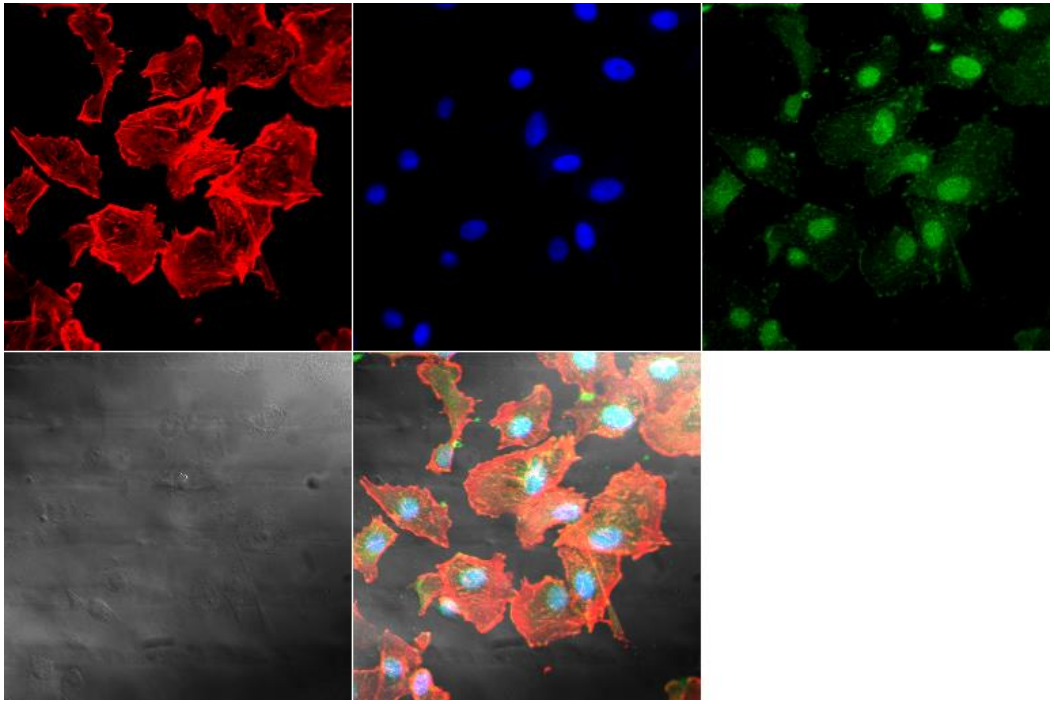

A3.1 Fluorescence images of BAE-1 cells growing on polyurethane 1A after 24 hours of applied shear stress (20dyne/cm^2). (Actin-red, nuclei-blue, vinculin-green).

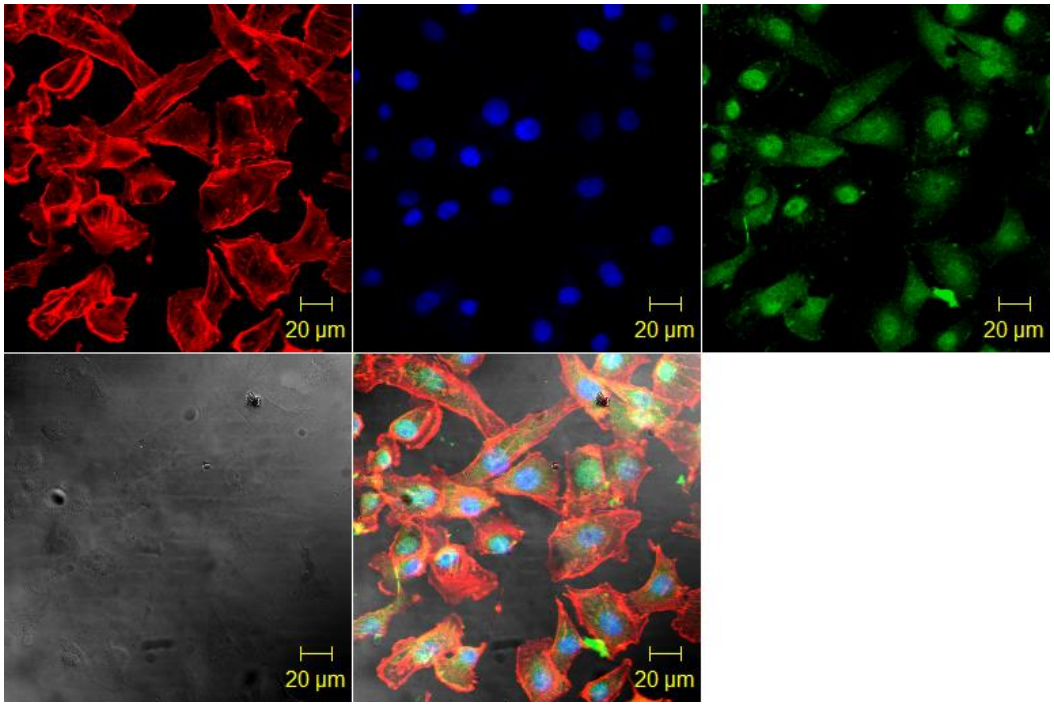

A3.2 Fluorescence images of BAE-1 cells growing on polyurethane 1D after 24 hours of applied shear stress (20dyne/cm^2). (Actin-red, nuclei-blue, vinculin-green).

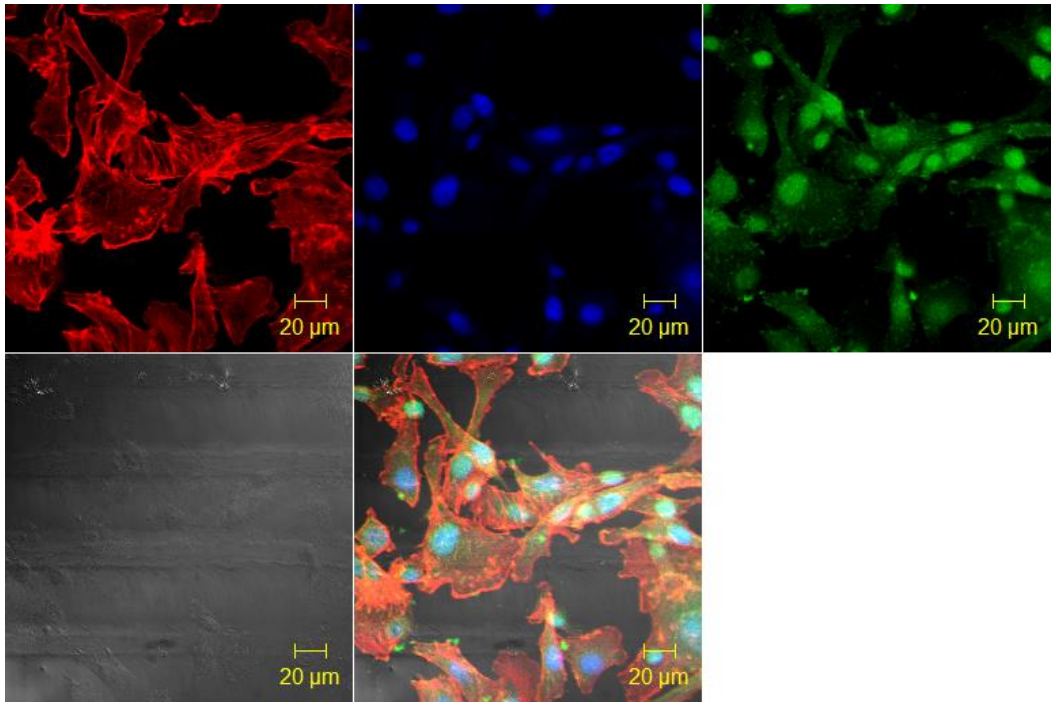

A3.3 Fluorescence images of BAE-1 cells growing on polyurethane 3A after 24 hours of applied shear stress (20dyne/cm^2). (Actin-red, nuclei-blue, vinculin-green).

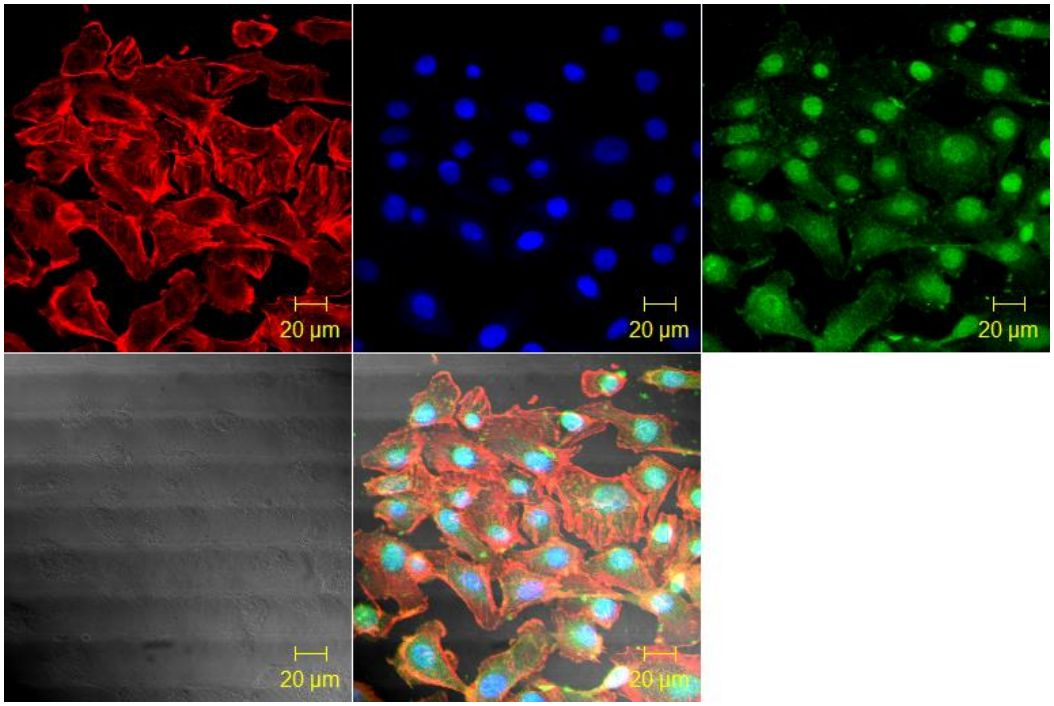

A3.4 Fluorescence images of BAE-1 cells growing on polyurethane 3D after 24 hours of applied shear stress (20dyne/cm^2). (Actin-red, nuclei-blue, vinculin-green).

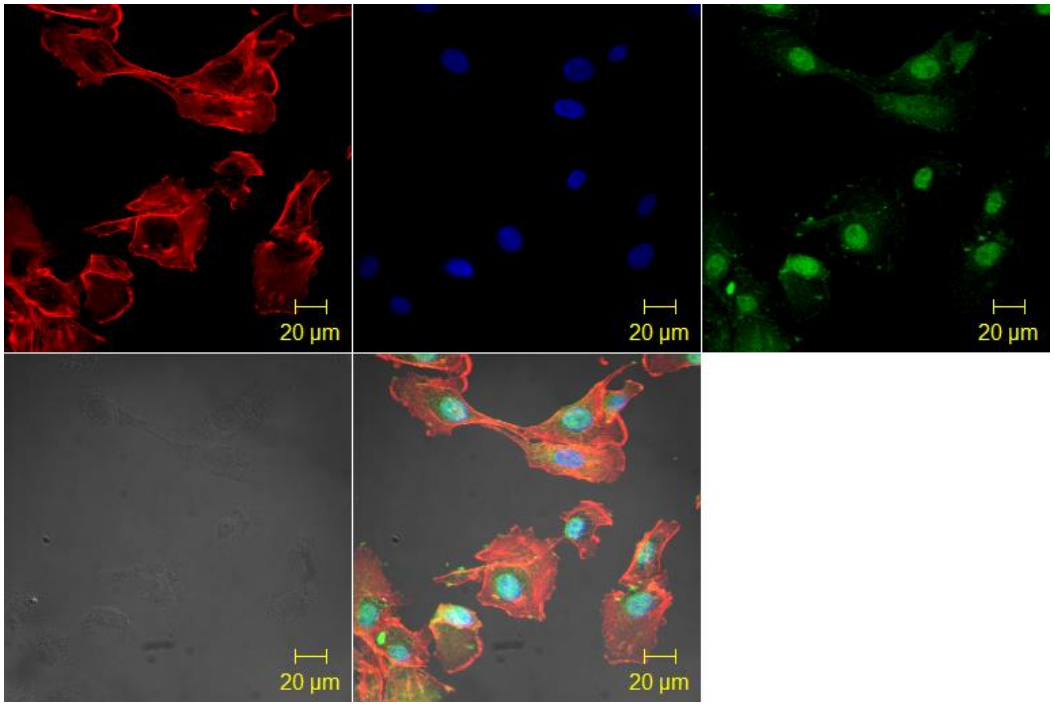

A3.5 Fluorescence images of BAE-1 cells growing on non-textured polyurethane after 24 hours of applied shear stress (20dyne/cm^2). (Actin-red, nuclei-blue, vinculin-green).